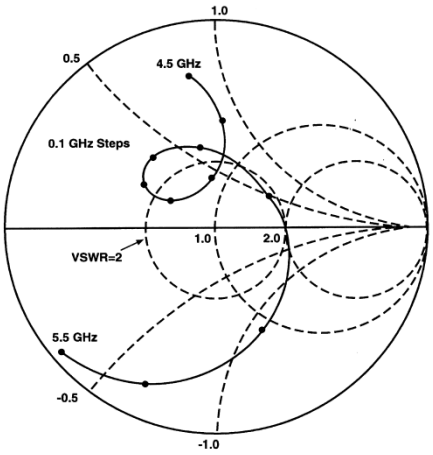

Applied Computational Electromagnetics Society Journal

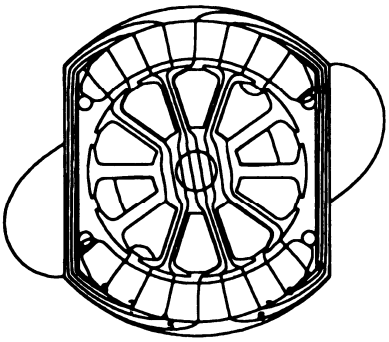

Editor-in-Chief
Atef Z. Elsherbeni

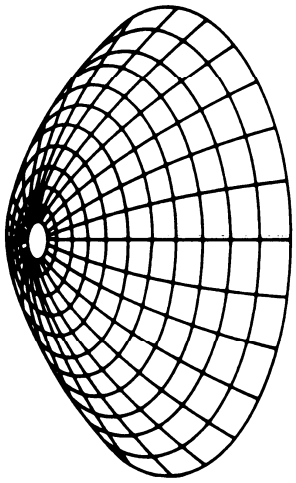

August 2010
Vol. 25 No. 8
ISSN 1054-4887

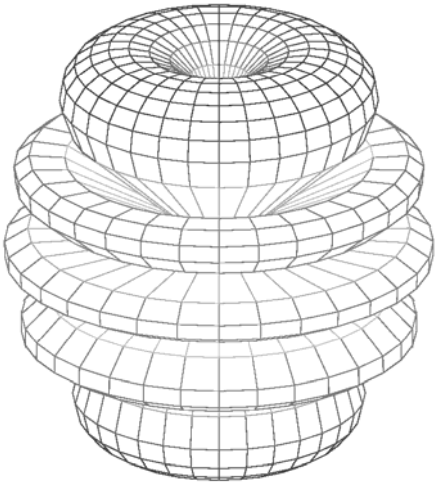

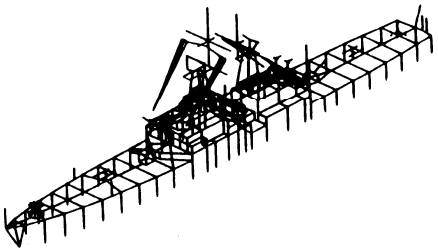

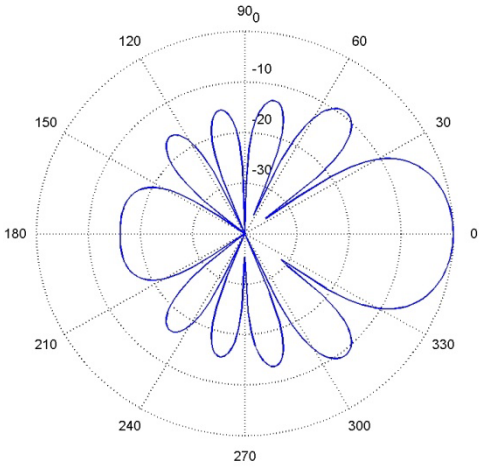

GENERAL PURPOSE AND SCOPE: The Applied Computational Electromagnetics Society ***(ACES)*** Journal hereinafter known as the ***ACES Journal*** is devoted to the exchange of information in computational electromagnetics, to the advancement of the state-of-the art, and the promotion of related technical activities. A primary objective of the information exchange is the elimination of the need to "re-invent the wheel" to solve a previously-solved computational problem in electrical engineering, physics, or related fields of study. The technical activities promoted by this publication include code validation, performance analysis, and input/output standardization; code or technique optimization and error minimization; innovations in solution technique or in data input/output; identification of new applications for electromagnetics modeling codes and techniques; integration of computational electromagnetics techniques with new computer architectures; and correlation of computational parameters with physical mechanisms.

SUBMISSIONS: The ***ACES Journal*** welcomes original, previously unpublished papers, relating to applied computational electromagnetics. Typical papers will represent the computational electromagnetics aspects of research in electrical engineering, physics, or related disciplines. However, papers which represent research in applied computational electromagnetics itself are equally acceptable.

Manuscripts are to be submitted through the upload system of ***ACES*** web site http://aces.ee.olemiss.edu See "Information for Authors" on inside of back cover and at ***ACES*** web site. For additional information contact the Editor-in-Chief:

Dr. Atef Elsherbeni
Department of Electrical Engineering
The University of Mississippi
University, MS 386377 USA
Phone: 662-915-5382 Fax: 662-915-7231
Email: atef@olemiss.edu

SUBSCRIPTIONS: All members of the Applied Computational Electromagnetics Society who have paid their subscription fees are entitled to receive the ***ACES Journal*** with a minimum of three issues per calendar year and are entitled to download any published journal article available at http://aces.ee.olemiss.edu.

Back issues, when available, are $15 each. Subscriptions to ***ACES*** is through the web site. Orders for back issues of the ***ACES Journal*** and changes of addresses should be sent directly to ***ACES***:

Dr. Allen W. Glisson
302 Anderson Hall
Dept. of Electrical Engineering
Fax: 662-915-7231
Email: aglisson@olemiss.edu

Allow four week's advance notice for change of address. Claims for missing issues will not be honored because of insufficient notice or address change or loss in mail unless the Executive Officer is notified within 60 days for USA and Canadian subscribers or 90 days for subscribers in other countries, from the last day of the month of publication. For information regarding reprints of individual papers or other materials, see "Information for Authors".

LIABILITY. Neither ***ACES***, nor the ***ACES Journal*** editors, are responsible for any consequence of misinformation or claims, express or implied, in any published material in an ***ACES Journal*** issue. This also applies to advertising, for which only camera-ready copies are accepted. Authors are responsible for information contained in their papers. If any material submitted for publication includes material which has already been published elsewhere, it is the author's responsibility to obtain written permission to reproduce such material.

APPLIED COMPUTATIONAL ELECTROMAGNETICS SOCIETY JOURNAL

Editor-in-Chief
Atef Z. Elsherbeni

August 2010
Vol. 25 No.8
ISSN 1054-4887

The ACES Journal is abstracted in INSPEC, in Engineering Index, DTIC, Science Citation Index Expanded, the Research Alert, and to Current Contents/Engineering, Computing & Technology.

The first, fourth, and sixth illustrations on the front cover have been obtained from the Department of Electrical Engineering at the University of Mississippi.

The third and fifth illustrations on the front cover have been obtained from Lawrence Livermore National Laboratory.

The second illustration on the front cover has been obtained from FLUX2D software, CEDRAT S.S. France, MAGSOFT Corporation, New York.

THE APPLIED COMPUTATIONAL ELECTROMAGNETICS SOCIETY

JOURNAL

Vol. 25 No. 8 August 2010

TABLE OF CONTENTS

Fundamental Limitations on the Use of Open-Region Boundary Conditions and Matched Layers to Solve the Problem of Gratings in Metallic Screens

Babak Alavikia and Omar M. Ramahi

Department of Electrical and Computer Engineering
University of Waterloo, ON, N2L3G1, Canada
balaviki@maxwell.uwaterloo.ca, oramahi@uwaterloo.ca

Abstract ─ Interest in accurate modeling of the electromagnetic wave scattering from grating surfaces has been renewed due to recent advances in the manipulation and localization of the light in novel application of plasmonic resonance. This work briefly reviews the frequency-domain finite methods that have been used extensively to solve the grating problem. Emphasis will be placed on the finite methods that use local boundary operators or matched layers to truncate the computational boundary. It is shown that significant errors can be generated when using either of these two mesh truncation techniques even if the truncation boundaries are receded to avoid any evanescent waves emanating from the gratings. To quantify the error, the solutions obtained using the boundary condition or matched layers are compared to the solutions obtained using either mode matching or the surface integral equation method, both of which are devoid of truncation boundary related approximations and errors. Additionally, limitations on the use of the periodic boundary condition to truncate the mesh for periodic problems are also addressed.

Index Terms ─ Finite element method, global boundary condition, infinite structures, local boundary condition, surface integral equation.

I. INTRODUCTION

Recent advances in manipulation and localization of the light in novel applications of plasmonic resonance such as near-field microscopy, sub-wavelength lithography, surface defect detection, and development of tunable optical filters has renewed interest in accurate modeling of wave scattering from grating surfaces. Several methods such as field decoupling by equivalent magnetic current [1, 2], integral equation [3], and mode matching [4-10] are reported in the literature to solve the problem of scattering from cavities engraved in a metallic screen. Although these methods are powerful, they are not general enough to address cavities with general shapes or cavities having inhomogeneous and anisotropic fillings. In contrast, the methods based on finite mathematics, such as, the finite element method (FEM) and the finite-difference time-domain method (FDTD) are suitable for the problem of scattering from general-shape cavities with anisotropic and inhomogeneous fillings [11-14].

When solving the scattering problem from a bounded target using finite mathematics, it is essential to introduce an artificial boundary to truncate the solution region surrounding the target. Appropriate boundary condition must be imposed on the artificial boundary to guarantee a well-posed and unique solution to the wave equation. In addition, the boundary condition must model the behavior of the wave at infinity. In other words, the artificial boundary must be as transparent as possible for impinging waves from the interior region.

There are two types of boundary conditions to truncate the solution region, viz., (i) non-local or integral type; (ii) local or differential type. Non-local types of boundary conditions are *analytical* integral equations which accurately model the behavior of the wave at the boundaries [15]. Therefore, they are exact for all range of incident angles. In addition, they can be imposed on the boundary which is very close to the scatterer body.

The major drawback of those types of boundary conditions is that they result in dense system matrix, which spoils the sparsity of the FEM system matrix. In contrast, local types of boundary conditions are partial differential equations which *approximate* the exact behavior of the wave at the artificial boundary [16-18].

When solving the problem of scattering from infinite grating surfaces containing multiple cavities using non-local boundary conditions, the solution region can be truncated at the opening of the cavities [11-14]. In [11-14], the domain of the surface integral equation as a boundary constraint is limited to the aperture of the cavities, and, thus, the infinitely extended perfect electric conducting (PEC) walls have no contribution in calculating the boundary condition. On the other hand, a difficulty in truncating the solution region arises when using local boundary conditions or matched layers (typically referred to in the literature as absorbing boundary conditions, ABC, or perfectly matched layer, PML) in solving the problem of scattering from gratings in infinite PEC screens. Since it is impossible to fully enclose the scatterer's geometry by the ABC or PML, the behavior of the scattered field due to the infinite PEC wall outside of the computational domain boundary cannot be modeled properly. Therefore, errors can be generated in the solution when using ABC or PML even if the truncation boundary is receded.

In this paper, we analyzed the performance of commonly used ABC or PML in solving the problem of scattering from grating surfaces containing a single or multiple cavities engraved in an infinite PEC screen. In particular, we focused on the errors introduced in the solution due to grazing incident waves. Next, we analyzed the dependence of this error on the location of the ABC. Finally, we addressed the error when using periodic boundary conditions when solving the problem of scattering from an infinite periodic array of cavities engraved in a PEC screen. The errors were calculated by comparison to the solutions obtained using an FEM-based method where the surface integral equation is used as a boundary constraint [14] and the mode matching technique reported in [7].

II. GENERAL DESCRIPTION OF THE PROBLEM

As a representative example of the problem of scattering from gratings in metallic screens, we consider the problem depicted in Fig. 1 which shows an electromagnetic wave impinging on a cavity engraved in an infinite metallic wall. The solution region can be truncated using the ABC as a local boundary condition as it is shown in Fig. 1.

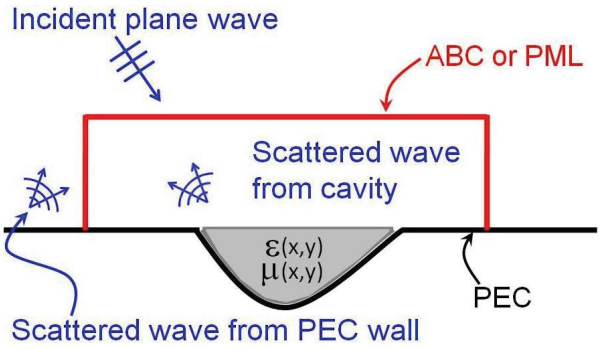

Fig. 1. Schematic of the scattering problem from a cavity with arbitrary shape in an infinite PEC surface. An ABC or PML is used to truncate the computational domain.

Because generic types of ABCs and PMLs are ineffective in absorption of evanescent waves, the introduced error due to these mesh truncation techniques is in general inversely proportional to the distance between the truncation walls and the cavity. Therefore, an ABC or PML cannot be located very close to the cavity. In addition, it is impossible to fully enclose the scatterer's geometry by an ABC or PML. Therefore, the behavior of the scattered field due to the PEC surface that lies outside of the computational domain boundary cannot be modeled properly and thus any consequential physical interaction cannot be included in the solution. In fact, more explicitly, as can be shown in Fig. 1, a portion of the scattered field from the PEC wall propagates into the solution region which causes error that would most likely depend on the incident angle. By increasing the incident angle, more energy is reflected into the solution region by the PEC walls located outside of the ABC, whereas, at zero angle of incidence, the reflected energy from the surface surrounding the cavity does not enter the computational domain depicted in Fig.1.

Therefore, this error is expected to increase as the incident angle increases.

To minimize this error, the domain truncating boundaries should be located far enough from the cavity to enclose a larger segment of the PEC wall in addition to the cavity. However, placing the boundary of the computational domain far from the cavity leads to prohibitive increase in the computational cost, in addition to inaccuracy in the solution due to the exclusion of a large part of the scatterer. The computational cost is most critical when considering cavities whose sizes are several wavelengths, and when loading the cavities to minimize the radar cross-section (RCS), requiring extensive optimizations. Notice, also, that enlarging the computational domain by including a larger segment of the PEC wall while keeping the upper boundary (the horizontal terminating boundary in Fig.1) very close to the PEC wall does not reduce the errors as in such scenario the upper boundary experiences a large concentration of waves incident at oblique angles, which cannot be absorbed effectively by typical PML or ABC methods. There are specialized ABC or PML methods that are designed to absorb waves incident at oblique angles, or even effectively absorb evanescent waves such as in [19, 20]. However, these truncation techniques are specialized and typically add additional computational overhead.

III. NUMERICAL EXPERIMENTS

To study the limitations on the use of ABC or PML to truncate the computational domain for the gratings problems considered in this work, we use the highly robust and widely used full-wave simulator, HFSS [21] which employs a highly effective implementation of PML. We emphasize that the purpose of the comparison is to accentuate the limitations of PML or ABC rather than the effectiveness of the simulator in general. Since the PML implementation in HFSS provides much higher accuracy than the ABC implementation in the same solver, we make comparison to the solution obtained using PML. This solution, henceforth, will be referred to as HFSS-PML. However, in the first example we showed the results obtained using ABC as a benchmark. This solution is referred to as HFSS-ABC. It is important to note that HFSS uses multilayer biaxial anisotropic materials in the PML implementation [22].

Absence of analytical solutions to the problem of scattering from cavities, the solutions generated by two methods will be used for gauging the errors caused by the HFSS-PML or HFSS-ABC solutions. The first method employs the surface integral equation to truncate the computational domain at the aperture of the cavity [14], and the second method employs the mode matching techniques [7]. These two solutions are considered highly accurate in the sense that the approximations used in their respective solution procedures involve discretization of the field rather than any boundary condition approximations.

The solutions presented here are made over a wide range of incident angles. For the transverse magnetic incident plane wave where the electric field vector lies along the axis of the cavities, the error in the magnitude of the total electric field at the aperture of the cavity is calculated as:

$$err = \sqrt{\frac{\int (E - E_0)^2 dl}{\int E_0^2 dl}} \times 100\%. \qquad (1)$$

where E is total electric field obtained using the HFSS-PML or HFSS-ABC solutions and E_0 is total electric field calculated using the surface integral equation method reported in [14] (throughout this work we refer to this methods as FEM-TFSIE), or the mode matching technique [7], respectively. The integration domain is the aperture of the cavities.

In the first example, we considered an 0.8λ X 0.4λ (width X depth) rectangular cavity in a PEC sheet where λ is the wavelength in free space. The solution region using HFSS-PML or HFSS-ABC is truncated by a rectangular mesh. The vertical distance of the truncation boundary from the PEC screen is h=1λ and the distance of the lateral truncation walls D from the edge of the cavity is set to be 4λ (see inset of Fig.2). Figure 2 shows the error using the results calculated using FEM-TFSIE and mode matching technique for incident angle range of 0^0-85^0. It is observed that by increasing the incident angle, the error increases in an almost exponential trend. This is because by increasing the incident angle, more reflected

waves from the PEC screen outside of the PML or ABC propagate into the solution region. As shown in Fig. 2, the increment trend is uniform in HFSS-PML case while it highly depends on incident angles in HFSS-ABC case for $\theta>30^0$. To validate this reason, we changed the distance of the lateral truncation walls (i.e. D) from the cavity. Figure 3 shows the effect of increasing D on the error for grazing incident angle of $\theta=85^0$. By increasing the D from 4λ to 16λ, the error decreases from 37% to 8% in HFSS-PML case. Notice that to achieve 8% solution accuracy, a computational space of approximately $32\lambda^2$ would be needed when using a PML-based truncation technique; whereas, the solution space using FEM-TFSIE which is confined to the cavity's area, would require a computational domain of $0.32\lambda^2$. (It is important to emphasize here that while approximate computational areas are used to highlight the efficiency and accuracy of the methods discussed here, other aspects of different code implementations are intentionally not discussed here such as the algorithm used to solve the systems matrix, the type of bases functions used in the FEM implementation, ...etc.)

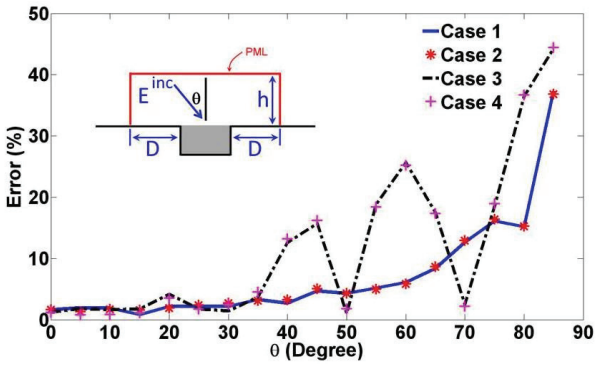

Fig. 2. Error versus incident angle θ for a 0.8λ X 0.4λ air-filled rectangular cavity, TM case, D=4λ, h=1λ. Error between results obtained using: Case1) HFSS-PML and FEM-TFSIE, Case2) HFSS-PML and Mode Matching Technique, Case3) HFSS-ABC and FEM-TFSIE, Case4) HFSS-ABC and Mode Matching Technique.

As a second example, we considered five identical cavities in a PEC screen. The cavities are rectangular with dimension of 0.8λ X 0.4λ and are separated by distance of 0.2λ. The vertical distance of the mesh truncation wall from the PEC screen is h=1λ and the distance of the lateral truncation walls from the cavities is set to be D=4λ (see the inset of Fig. 4). Figure 4 shows the error for incident angle varying from $\theta=0^0$ to $\theta=85^0$. Figure 5 shows the decrease in the cavity field error from 30% to 14% when D is increased from 4λ to 16λ. Notice that despite the excessive computational domain needed when D is increased to 1λ resulting in a computational domain of $37\lambda^2$, the error in the apertures field remains above 10%.

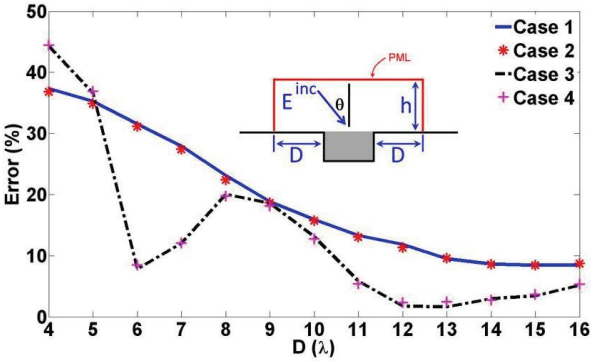

Fig. 3. Error versus distance D of the lateral PML walls from a 0.8λ X 0.4λ air-filled rectangular cavity, TM case, θ=85, h=1λ. Error between results obtained using: Case1) HFSS-PML and FEM-TFSIE, Case2) HFSS-PML and Mode Matching Technique, Case3) HFSS-ABC and FEM-TFSIE, Case4) HFSS-ABC and Mode Matching Technique.

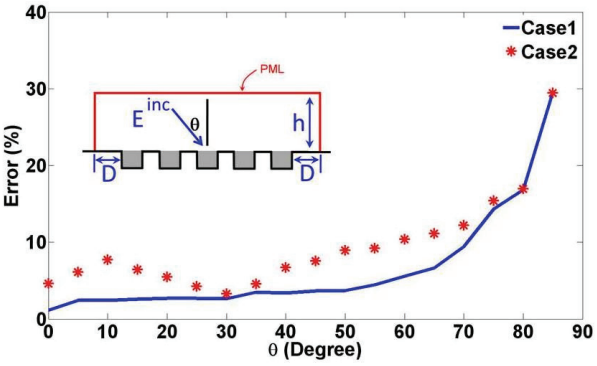

Fig. 4. Error versus incident angle θ for five identical 0.8λ X 0.4λ air-filled rectangular cavities, TM case, D=4λ, h=1λ. The cavities are separated by 0.2 λ. Error between results obtained using: Case1) HFSS-PML and FEM-TFSIE, Case2) HFSS-PML and Mode Matching Technique.

As the final example, we considered an infinite array of identical cavities in a metallic screen. The

cavities are rectangular with dimension of 0.8λ X 0.4λ and are separated by a distance of 0.2λ. Therefore, the periodicity of the cavity is P=1λ. Using Floquet theorem, the solution region can be limited to one unit-cell containing one period of the infinite array (see inset of Fig. 6). In the HFSS solution, the periodic boundary condition and the PML are applied on the lateral walls and the top wall of the truncation boundaries, respectively.

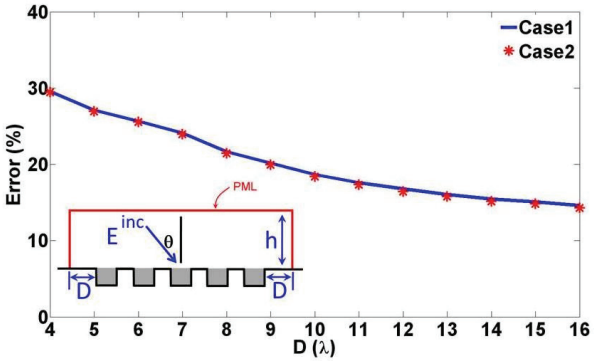

Fig. 5. Error versus distance D of the lateral PML walls from the marginal cavities in an array of five identical 0.8λ X 0.4λ air-filled rectangular cavities, TM case, θ=85, h=1λ. The cavities are separated by 0.2λ. Error between results obtained using: Case1) HFSS-PML and FEM-TFSIE, Case2) HFSS-PML and Mode Matching Technique.

As the final example, we considered an infinite array of identical cavities in a metallic screen. The cavities are rectangular with dimension of 0.8λ X 0.4λ and are separated by a distance of 0.2λ. Therefore, the periodicity of the cavity is P=1λ. Using Floquet theorem, the solution region can be limited to one unit-cell containing one period of the infinite array (see inset of Fig. 6). In the HFSS solution, the periodic boundary condition and the PML are applied on the lateral walls and the top wall of the truncation boundaries, respectively.

We calculated the truncation error in the electric field at the aperture of the cavities in the unit-cell using the results calculated for a finite array of 21 identical cavities with the same dimension using FEM-TFSIE. Figure 6 shows the error for a unit cell containing 1, 3 and 9 cavities for incident angle varying from $\theta=0^0$ to $\theta=85^0$. Notice that changing the size of the number of cavities in the unit cell does not change the physical problem at hand. We observe that by increasing the size of the unit cell to three and nine periods of array (see inset of Fig. 6), the error decreases significantly. We are not in a position to discuss the particular implementation of the periodic boundary condition in HFSS, however, what is quite interesting is that the error in the HFSS solution which directly depends on the periodic boundary condition implemented in HFSS, changes appreciably depending on the number of periods considered.

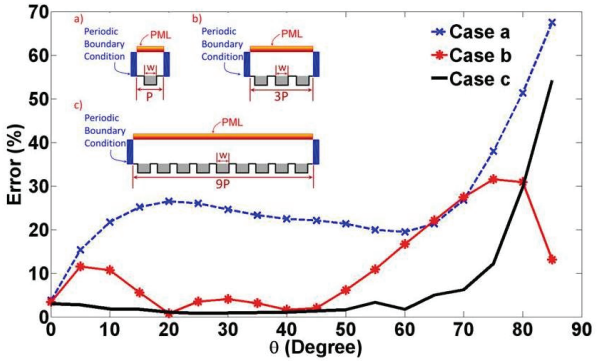

Fig. 6. Error in field calculation versus incident angle θ at the aperture of the center cavity of the unit-cell in an infinite array of identical 0.8λ X 0.4λ rectangular air-filled cavities, TM case. The cavities are separated by 0.2λ. Case a) 1 cavity in a unit-cell, Case b) 3 cavities in a unit-cell, Case c) 9 cavities in a unit-cell. Error between results is obtained using HFSS and FEM-TFSIE.

IV. CONCLUSION

In this study, we highlighted the inherent limitation in truncation the infinite structure using local boundary operators, such as ABC or PML, in context of the problem of scattering from gratings containing a single or multiple cavities engraved in an infinite PEC screen. In fact, we showed that there is an inherent error in the solution due to the truncation of the solution region and ignoring the portion of PEC walls located outside the solution region. Numerical examples of single and multiple cavities engraved in an infinite PEC wall were presented to calculate the error in field computation using PML. The root mean square error in the field computation using PML is calculated with respect to the FEM-based method using a non-local boundary condition and mode matching technique as the accurate solutions. First, we analyzed the error which introduced to the solution due to the grazing incident waves. We

showed that the error in the solution due to truncation increases almost exponentially as the incident angle increases. Next, we analyzed the dependence of this error to location of the mesh truncation boundary. We showed that the error decreases by receding the boundary but cannot be eliminated completely while incurring prohibitive increase of computational resources. Finally, we addressed the error in solution while using periodic boundary condition in truncating the solution region into a unit-cell when solving the problem of scattering from an infinite periodic array of cavities engraved in a metallic screen.

REFERENCES

[1] R. F. Harrington and J. R. Mautz, "A generalized network formulation for aperture problems," *IEEE Trans. Antennas Propagt.*, vol. 24, no. 6, pp. 870-873, Nov. 1976.

[2] D. T. Auckland and R. F. Harrington, "Electromagnetic transmission through a filled slit in a conducting plane of finite thickness, TE Case," *IEEE Trans. Microwave Theory Tech.*, vol. 26, no. 7, pp. 499-505, Jul. 1978.

[3] Y. Shifman and Y. Leviatan, "Scattering by a groove in a conducting plane A PO-MoM hybrid formulation and wavelet analysis," *IEEE Trans. Antennas Propagt.*, vol. 49, no. 12, pp. 1807-1811, Dec. 2001.

[4] Y. -L Kok, "Boundary-value solution to electromagnetic scattering by a rectangular groove in a ground plane," *J. Opt. Soc. Am. A,* vol. 9, no. 2, pp. 302-311, Feb. 1992.

[5] T. J. Park, H. J. Eom, and K. Yoshitomi, "An analytic solution for transverse-magnetic scattering from a rectangular channel in a conducting plane," *J. Appl. Phys.*, vol. 73, no. 1, pp. 3571-3573, Apr. 1993.

[6] T. J. Park, H. J. Eom, and K. Yoshitomi, "An analysis of transverse electric scattering from a rectangular channel in a conducting plane," *Radio Science*, vol. 28, no. 5, pp. 663-673, Sep.-Oct. 1993.

[7] T. J. Park, H. J. Eom, and K. Yoshitomi, "Analysis of TM scattering from finite rectangular grooves in a conducting plane," *J. Opt. Soc. Am. A*, vol. 10, no. 5, pp. 905-911, May 1993.

[8] R. A. Depine and D. C. Skigin, "Scattering from metallic surfaces having a finite number of rectangular grooves," *J. Opt. Soc. Am. A*, vol. 11, no. 11, pp. 2844-2850, Nov. 1994.

[9] M. A. Basha, S. K. Chaudhuri, S. Safavi-Naeini, and H. J. Eom, "Rigorous formulation for electromagnetic plane-wave scattering from a general-shaped groove in a perfectly conducting plane," *J. Opt. Soc. Am. A*, vol. 24, no. 6, pp. 1647-1655, Jun. 2007.

[10] M. A. Basha, S. K. Chaudhuri, and S. Safavi-Naeini, "Electromagnetic scattering from multiple arbitrary shape grooves: a generalized formulation," *IEEE/MTT-S International Microwave Symposium*, pp. 1935-1938, June 2007.

[11] J. M. Jin and J. L. Volakis, "TM scattering by an inhomogeneously filled aperture in a thick conducting plane," *IEE Proceedings-H Microwaves, Antennas and Propagation*, vol. 137, no. 3, pp. 153-159, Jun. 1990.

[12] J. M. Jin and J. L. Volakis, "TE scattering by an inhomogeneously filled thick Conducting Plane," *IEEE Trans. Antennas Propagt.*, vol. 38, no. 8, pp. 1280-1286, Aug. 1990.

[13] O. M. Ramahi and R. Mittra, "Finite element solution for a class of unbounded geometries," *IEEE Trans. Antennas Propagt.*, vol. 39, no. 2, pp. 244-250, Feb. 1991.

[14] B. Alavikia and O. M. Ramahi, "Finite-element solution of the problem of scattering from cavities in metallic screens using the surface integral equation as a boundary constraint," *J. Opt. Soc. Am. A*, vol. 26, no. 9, pp. 1915-1925, Sep. 2009.

[15] B. H. Mcdonald and A. Wexler, "Finite-element solution of unbounded field problems," *IEEE Trans. Microwave Theory Tech.*, vol. 20, no. 12, pp. 841-847, Dec. 1972.

[16] B. Engquist and A. Majda, "Absorbing boundary condition for numerical simulation of waves," *Proceeding of the National Academy of Sciences of the United States of America*, vol. 74, no. 5, pp. 1765-1766, May 1977.

[17] A. Bayliss, M. Gunzburger, and E. Turkel, "Boundary condition for the numerical solution of elliptic equations in exterior regions," *Siam Journal On Applied Mathematics*, vol. 42, no. 2, pp. 430-450, Apr. 1982.

[18] O. M. Ramahi, A. Khebir, and R. Mittra, "Numerically derived absorbing boundary condition for the solution of open region scattering problems," *IEEE Trans. Antennas Propagt.*, vol. 39, no. 3, pp. 350-353, Mar. 1991.

[19] O. M. Ramahi, "The concurrent complementary operators method for FDTD mesh truncation," *IEEE Trans. Antennas Propagt.*, vol. 46, no. 10, pp. 1475-1482, Oct. 1998.

[20] J-P. Berenger, "Numerical reflection from FDTD-PMLs: A comparison of the split PML with the unsplit and CFSPMLs," *IEEE Trans. Antennas Propagt.*, vol. 50, no. 3, pp. 258-265, Mar. 2002.

[21] Ansoft HFSS Version 11.2, "Ansoft Corporation," http://www.ansoft.com.

[22] I. Bardi and Z. Cendes, "New directions in HFSS for designing microwave devices," *Microwave Journal*, vol. 41, no. 8, pp. 22, Aug. 1998.

Babak Alavikia received the B.Sc. degree in atomic and molecular physics from Tabriz University, Tabriz, Iran, in 1995, and the M.Sc. degree in the solid state physics, in 1998, from the University of Urmia, Urmia, Iran. He is currently working toward the Ph.D. degree in electrical and computer engineering at university of Waterloo, Canada. Since 2007, he has worked on developing an accurate method to model the electromagnetic scattering from the grating surfaces to study plasmonic resonance and extra ordinary transmission of light through sub-wavelength apertures. His research interests include numerical techniques in electromagnetic and full-wave analysis of electromagnetic scattering in electromagnetic compatibility and interference applications.

Omar M. Ramahi received the BS degrees in Mathematics and Electrical and Computer Engineering (summa cum laude) from Oregon State University, Corvallis, OR. He received his M.S. and Ph.D. in Electrical and Computer Engineering from the University of Illinois at Urbana-Champaign. Presently, he is a Professor in the Electrical and Computer Engineering Department. He holds cross appointments with the Department of Mechanical and Mechatronics Engineering and the Department of Physics and Astronomy. He has authored and co-authored over 240 journal and conference papers. He is a co-author of the book EMI/EMC Computational Modeling Handbook, 2nd Ed. (Springer-Verlag, 2001). Presently, he serves as an Associate Editor for the IEEE Transactions on Advanced Packaging and as the IEEE EMC Society Distinguished Lecturer. Dr. Ramah is an IEEE Fellow.

An Unconditionally Stable Subcell Model for Thin Wires in the ADI-FDTD Method

Juan Chen[1], Jianguo Wang [1, 2]

[1]School of Electronic and Information Engineering
Xi'an Jiaotong University, Xi'an 710049, China
chenjuan0306@yahoo.com.cn

[2]Northwest Institute of Nuclear Technology
P. O. Box 69-15, Xi'an 710024, China

Abstract **-** In this paper, a method for the implementation of thin wire with the alternating-direction implicit finite-difference time-domain (ADI-FDTD) method is discussed. The magnetic field around the wire is modified according to the "standard" subcell model, which results in the modification to the tridiagonal matrix system in the ADI-FDTD. The perfect-electric-conductor (PEC) condition is directly incorporated within the tridiagonal matrix equation. This method is efficient, stable, and suitable to ADI-FDTD scheme with large time step size. The validity of this method is confirmed through numerical examples.

Index Terms **-** ADI-FDTD method, PEC condition, subcell model, thin wire.

I. INTRODUCTION

The alternating-direction-implicit finite-difference time-domain (ADI–FDTD) method is an unconditionally stable alternative to the standard fully explicit FDTD method [1-5]. The main advantage of the ADI-FDTD method is that the Courant–Friedrich–Levy (CFL) condition that is always required by the conventional FDTD method can be totally removed. Hence, the ADI-FDTD method is extremely useful for problems where a very fine mesh is needed over a large geometric area. Nevertheless, from the implementation point of view, the ADI-FDTD method is more complicated than the conventional FDTD method. This is because the field components of the conventional FDTD method can be directly updated, but in the ADI-FDTD method they have to be implicitly updated by solving a tridiagonal matrix system.

In many electromagnetic problems analyzed numerically with the FDTD method, thin wires need to be modeled. A wire is considered thin when its diameter is less than the selected mesh size. It is certainly possible to select a sufficiently small mesh, so that the wire diameter occupies one or more computational cells, but this approach often results in a very fine discretization and excessive computational resources. As an alternative, a "standard" subcel1 model which is based on the near-field physics can be used [6]. This model assumes that the circumferential component of the magnetic field and the radial component of the electric field vary as 1/r near the wire, where r is the radial distance from the wire axis. In such a case, a modification to the standard FDTD algorithm is easily available. However, the modification to the ADI-FDTD algorithm is complicated, due to its implicit calculation by solving a tridiagonal matrix system.

$$H_x^{n+\frac{1}{2}}\left(i_0, j_0 \pm \frac{1}{2}, k+\frac{1}{2}\right) = H_x^n\left(i_0, j_0 \pm \frac{1}{2}, k+\frac{1}{2}\right) + \frac{\Delta t}{2\mu\Delta z}\left[E_y^n\left(i_0, j_0 \pm \frac{1}{2}, k+1\right) - E_y^n\left(i_0, j_0 \pm \frac{1}{2}, k\right)\right]$$
$$-\frac{\Delta t}{2\mu\Delta y}\left(\frac{2}{\ln\left(\Delta y / r_0\right)}\right)\left[E_z^{n+\frac{1}{2}}\left(i_0, j_0+\frac{1}{2} \pm \frac{1}{2}, k+\frac{1}{2}\right) - E_z^{n+\frac{1}{2}}\left(i_0, j_0 \pm \frac{1}{2} - \frac{1}{2}, k+\frac{1}{2}\right)\right], \quad \left(k_1 \le k \le k_2\right) \tag{1}$$

$$E_z^{n+\frac{1}{2}}\left(i_0, j_0, k+\frac{1}{2}\right) = E_z^n\left(i_0, j_0, k+\frac{1}{2}\right) + \frac{\Delta t}{2\varepsilon\Delta x}\left[H_y^n\left(i_0+\frac{1}{2}, j_0, k+\frac{1}{2}\right) - H_y^n\left(i_0-\frac{1}{2}, j_0, k+\frac{1}{2}\right)\right]$$
$$-\frac{\Delta t}{2\varepsilon\Delta y}\left[H_x^{n+\frac{1}{2}}\left(i_0, j_0+\frac{1}{2}, k+\frac{1}{2}\right) - H_x^{n+\frac{1}{2}}\left(i_0, j_0-\frac{1}{2}, k+\frac{1}{2}\right)\right] \tag{2}$$

$$\left[1+\frac{s_1\Delta t^2}{2\varepsilon\mu\Delta y^2}\right]E_z^{n+\frac{1}{2}}\left(i_0, j_0, k+\frac{1}{2}\right) - \frac{s_1\Delta t^2}{4\varepsilon\mu\Delta y^2}\left[E_z^{n+\frac{1}{2}}\left(i_0, j_0+1, k+\frac{1}{2}\right) + E_z^{n+\frac{1}{2}}\left(i_0, j_0-1, k+\frac{1}{2}\right)\right]$$
$$= E_z^n\left(i_0, j_0, k+\frac{1}{2}\right) + \frac{\Delta t}{2\varepsilon\Delta x}\left[H_y^n\left(i_0+\frac{1}{2}, j_0, k+\frac{1}{2}\right) - H_y^n\left(i_0-\frac{1}{2}, j_0, k+\frac{1}{2}\right)\right]$$
$$-\frac{\Delta t^2}{4\mu\varepsilon\Delta y\Delta z}\left[E_y^n\left(i_0, j_0+\frac{1}{2}, k+1\right) - E_y^n\left(i_0, j_0-\frac{1}{2}, k+1\right) - E_y^n\left(i_0, j_0+\frac{1}{2}, k\right) + E_y^n\left(i_0, j_0-\frac{1}{2}, k\right)\right]$$
$$-\frac{\Delta t}{2\varepsilon\Delta y}\left[H_x^n\left(i_0, j_0+\frac{1}{2}, k+\frac{1}{2}\right) - H_x^n\left(i_0, j_0-\frac{1}{2}, k+\frac{1}{2}\right)\right] \tag{3}$$

This paper presents the implementation of the thin wires for the ADI-FDTD method. The magnetic field around the wire is modified according to the "standard" subcell model, which results in the modification to the tridiagonal matrix system. For the perfect conductor boundary condition, the tangential electronic field component along the wire needs to be set to zero, which is directly incorporated within the tridiagonal matrix system. This method is unconditionally stable and has high accuracy. The theory proposed in this article is validated through numerical examples.

II. FORMULATIONS

The field components around thin wire are shown in Fig. 1. r_0 is the radius of the wire. i_0 and j_0 denote the indices of spatial increments of thin wire. Indices $k_1 \le k \le k_2$ denote the height of the wire.

In the ADI-FDTD method, the calculation for one discrete time step is performed using two procedures. According to the "standard" subcell model [3], the numerical formulations of the $E_z^{n+1/2}$, $H_x^{n+1/2}$ components near the thin wire in the first procedure for the ADI-FDTD method are given in eqs. (1) and (2) above. Obviously, updating of $E_z^{n+1/2}$ component, as shown in eq. (2), needs the unknown $H_x^{n+1/2}$ component at the same time; thus the $E_z^{n+1/2}$ component has to be updated implicitly. By substituting eq. (1) into eq. (2), the equation for $E_z^{n+1/2}$ field is given in eq. (3), where $s_1 = 2/\ln\left(\Delta y / r_0\right)$. Thus, $E_z^{n+1/2}$ fields along a particular y-directed line ($i = i_0$) are updated simultaneously by solving the tridiagonal matrix equation through eq. (4) and repeated for each k ($k_1 \le k \le k_2$), where $\chi = \Delta t^2 / 4\varepsilon\mu\Delta y^2$, $E_{z,j_0}^{n+1/2}$ is the unknown z-direction electronic field, r_{j_0} is the right side of eq. (3). For other k value ($k < k_1$ or $k > k_2$), and other i value ($i \ne i_0$), standard ADI-FDTD formulation is applied.

$$\xrightarrow{j_0}\begin{bmatrix} \cdots & \cdots & \cdots & \cdots & \cdots & \cdots & \cdots \\ \cdots & 1+2\chi & -\chi & 0 & 0 & 0 & \cdots \\ \cdots & -\chi & 1+\chi+s_1\chi & -s_1\chi & 0 & 0 & \cdots \\ \cdots & 0 & -s_1\chi & 1+2s_1\chi & -s_1\chi & 0 & \cdots \\ \cdots & 0 & 0 & -s_1\chi & 1+s_1\chi+\chi & -\chi & \cdots \\ \cdots & 0 & 0 & 0 & -\chi & 1+2\chi & \cdots \\ \cdots & \cdots & \cdots & \cdots & \cdots & \cdots & \cdots \end{bmatrix} \begin{bmatrix} \cdots \\ E_{z,j_0-2}^{n+1/2} \\ E_{z,j_0-1}^{n+1/2} \\ E_{z,j_0}^{n+1/2} \\ E_{z,j_0+1}^{n+1/2} \\ E_{z,j_0+2}^{n+1/2} \\ \cdots \end{bmatrix} = \begin{bmatrix} \cdots \\ r_{j_0-2} \\ r_{j_0-1} \\ r_{j_0} \\ r_{j_0+1} \\ r_{j_0+2} \\ \cdots \end{bmatrix} \tag{4}$$

$$\uparrow j_0-1 \quad \uparrow j_0 \qquad \uparrow j_0+1$$

$$\begin{bmatrix} \cdots & \cdots & \cdots & \cdots & \cdots & \cdots \\ \cdots & 1+2\chi & -\chi & 0 & 0 & \cdots \\ \cdots & -\chi & 1+\chi+s_1\chi & -s_1\chi & 0 & \cdots \\ \cdots & 0 & -s_1\chi & 1+s_1\chi+\chi & -\chi & \cdots \\ \cdots & 0 & 0 & -\chi & 1+2\chi & \cdots \\ \cdots & \cdots & \cdots & \cdots & \cdots & \cdots \end{bmatrix} \begin{bmatrix} \cdots \\ E_{z,j_0-2}^{n+1/2} \\ E_{z,j_0-1}^{n+1/2} \\ E_{z,j_0}^{n+1/2} \\ E_{z,j_0+1}^{n+1/2} \\ E_{z,j_0+2}^{n+1/2} \\ \cdots \end{bmatrix} = \begin{bmatrix} \cdots \\ r_{j_0-2} \\ r_{j_0-1} \\ r_{j_0+1} \\ r_{j_0+2} \\ \cdots \end{bmatrix} \tag{5}$$

$$\uparrow j_0-1 \qquad \uparrow j_0+1$$

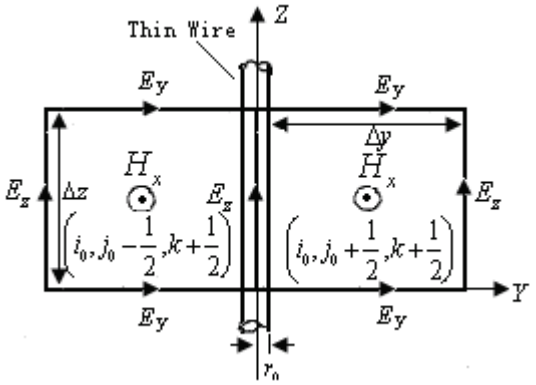

Fig. 1. Field components around a thin wire ($k_1 \le k \le k_2$).

The thin wire is often seen as perfect electric conductor. The tangential electronic field value E_z along the wire must be set to zero. So in the matrix systems (4), the values of $E_{z,j_0}^{n+1/2}$ are not calculated. Then the matrix system (4) becomes (5) above.

Thus, components $E_z^{n+1/2}$ are updated by solving the modified tridiagonal matrix system through Eqs. (5). This ADI-FDTD method incorporates the PEC condition into the matrix system. It seems to be complicated, but it is unconditionally stable and has higher accuracy. If we set the tangential electric field values $E_z^{n+1/2}$ to be zeros directly after solving the tridiagonal matrix system (4), the ADI-FDTD method is unstable, even for very small time step size, which is validated through numerical examples in the next section.

In the second procedure, components E_z^{n+1}, H_y^{n+1} can similarly be treated as $E_z^{n+1/2}$ and $H_x^{n+1/2}$ in the first procedure, which is not shown here due to space limitation.

III. NUMERICAL VALIDATION

To validate the theory presented in this paper, a simple numerical simulation is studied. A thin wire of length 10 cm and radius of 1 mm is embedded in a shielding enclosure, as shown in Fig. 2. The physical dimension of the enclosure is $15cm \times 15cm \times 15cm$. In the middle of the enclosure, a small current source is applied along the z direction. The time dependence of the excitation function is:

$$g(t) = \exp[-\alpha(t-t_0)^2] \tag{6}$$

where α and t_0 are constants, and equal to $1.26\times10^{10}\,\mathrm{s}^{-2}$ and $1.0\times10^{-9}\,\mathrm{s}$, respectively. In such a case, the highest frequency of interest is 2 GHz.

The space increments used in the FDTD simulation are $\Delta x=\Delta y=\Delta z=5mm$. The total mesh size is $30\times30\times30$. Observation point A is 5 cells diagonally far from the source. We apply the ADI-FDTD technique to compute the time domain electric field at the observation point. The time step is $\Delta t=1\Big/c\sqrt{(1/\Delta x)^2+(1/\Delta y)^2+(1/\Delta z)^2}=9.62\mathrm{ps}$, which is the maximum time step to satisfy the limitation of the 3D CFL condition in the conventional FDTD method. For simplicity, both the thin wire and the enclosure are perfect electric conductors.

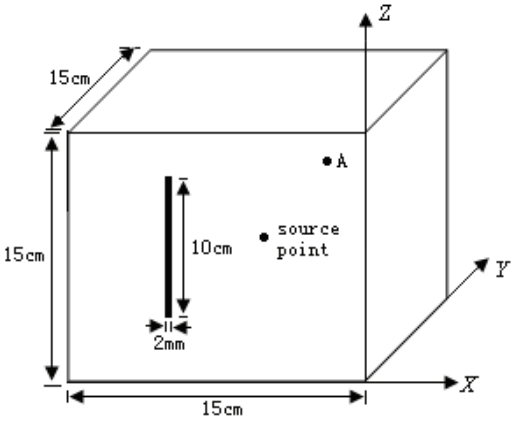

Fig. 2. Geometric configuration of the numerical simulation.

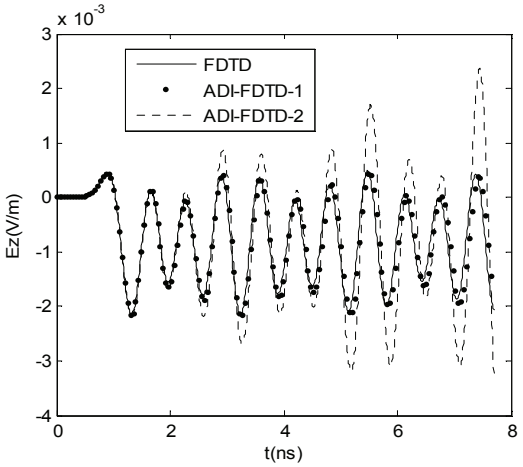

Fig. 3. The electric field component E_z at observation point A calculated by different methods.

To ensure the ADI-FDTD method be symmetric up to the numerical noise level, the excitation field should be directly incorporated within the tridiagonal matrix and the time discretization of the source is done appropriately within each full time step [7].

Figure 3 gives the results of the electric field component E_z at observation point A calculated by ADI-FDTD- 2 methods for large number of time steps.

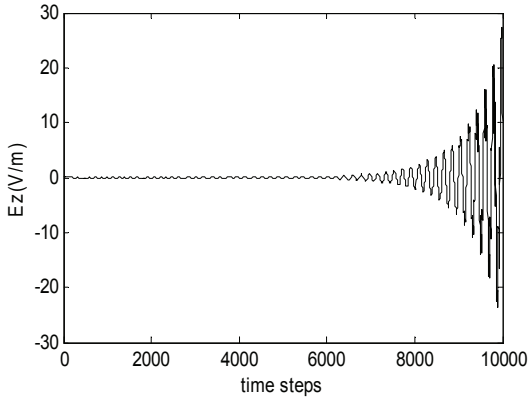

Fig. 4. The electric field component E_z at observation point A calculated by ADI-FDTD-2 methods for large number of time steps.

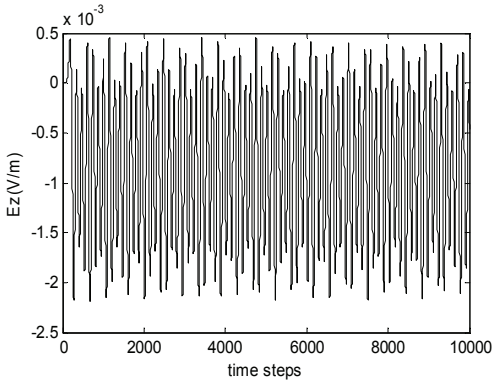

Fig. 5. The electric field component E_z at observation point calculated by ADI-FDTD -1 methods for large number of time steps.

The ADI-FDTD-1 denotes the method that incorporates the PEC condition into the matrix system. The ADI-FDTD-2 denotes the method that set the tangential electric field values E_z to be zeros directly after solving the tridiagonal matrix system. For comparison, the result obtained by the conventional FDTD method is

also plotted in this figure. In all the methods, the time step sizes are 9.62ps. It can be seen from this figure that the results calculated by ADI-FDTD-1 agree well with the results obtained by the conventional FDTD, which shows that the ADI-FDTD-1 method has higher accuracy. The value calculated by ADI-FDTD-2 deviate from that of conventional FDTD significantly. It is apparent that ADI-FDTD-2 can't obtain correct results.

To confirm the stability of these two methods, the ADI-FDTD program is tested for a long time history. Figure 4 shows the result of the electric field component E_z at observation point A calculated by ADI-FDTD-2 method for large number of time steps, the time step size is 9.62ps. It can be seen from this figure that the result of method 2 starts to be unstable after 6,000 time steps. To confirm the stability of method 1, the ADI-FDTD program is tested for 10,000 time steps with time step size 384.80ps which is 40 times as that of conventional FDTD method. No instability problem is observed. This illustrates that the ADI-FDTD scheme based on the method that incorporates the PEC condition into the matrix system is unconditionally stable, and the programs based on the method that set the tangential electric field values E_z to be zeros directly are not stable, even for small number of time steps.

IV. CONCLUSION

Based on the assumption of a 1/r dependence of the magnitude of local fields with radial distance r from the wire center, the magnetic field around the thin wire is modified, which results in the modification to the tridiagonal matrix system in the ADI-FDTD method. Meanwhile, due to the implicit calculation of the ADI-FDTD method, the perfect conductor boundary condition must be incorporated within the tridiagonal matrix system. The matrix needs to cross out the rows and columns for which the value doesn't need to be calculated. This method is unconditionally stable and has higher accuracy, which is validated through numerical examples. It needs to be noted that the stability of the ADI-FDTD-1 method is numerically verified rather than theoretically proven. The theoretical analysis of the stability is under research and will be reported in a future publication.

This unconditionally stable subcell model can be used to calculate the induced currents on the coupled wires in cavity, simulate the inner conductor of the coaxial feed, and analyze the radiation from the shielding cable, thus it has important effects on the electromagnetic numerical simulations.

ACKNOWLEDGMENT

This work was supported by the Research Fund for the Doctoral Program of Higher Education of China (20090201120030), and also supported by the Basic Fund of Xi'an Jiaotong University.

REFERENCES

[1] F. Zheng, Z. Chen, and J. Zhang, "A finite-difference time-domain method without the Courant stability conditions," *IEEE Microwave Guided Wave Lett.*, vol. 9, pp. 441–443, Nov. 1999.

[2] T. Namiki, "3-D ADI-FDTD method-unconditionally stable time-domain algorithm for solving full vector Maxwell's equations," *IEEE Trans. Microwave Theory Tech.,* vol. 48, pp. 1743–1748, Oct. 2000.

[3] G. Sun and C. W. Trueman, "Some fundamental characteristics of the one-dimensional alternate-direction-implicit finite-difference time domain method," *IEEE Trans. Microwave Theory Tech.,* vol. 52, pp. 46-52, Jan. 2004.

[4] I. Ahmed and Z. Chen, "Error reduced ADI-FDTD methods," *IEEE Antennas Wireless Propag. Lett,* vol. 4, pp. 323-325, 2005.

[5] J. Chen and J. Wang, "PEC condition implementation for the ADI-FDTD method," *Microwave Opt. Technol. Lett.,* vol. 49, pp. 526-530, Mar. 2007.

[6] K. Umashankar, A. Taflove, and B. Beker, "Calculation and experimental validation of induced currents on coupled wires in an arbitrary shaped cavity," *IEEE Trans. Antennas Propagat.,* vol. 35**,** pp. 1248-1257, Nov. 1987.

[7] B. Donderici and F. L. Teixeira, "Symmetric source implementation for the ADI-FDTD

method," *IEEE Trans. Antennas Propagat.,* vol. 53, pp. 1562-1565, Apr. 2005.

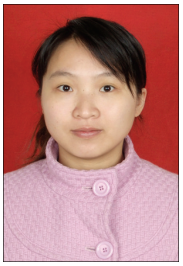

Juan Chen was born in Chongqing, China, in 1981. She received the B.S. degree in Public Security Protection Engineering from Chinese People Public- Security University, Beijing, China in 2003 and the Ph.D. degree in electromagnetic field and microwave techniques from Xi'an Jiaotong University, Xi'an, China in 2008. She now serves as a lecturer in the School of Electronic and Information Engineering, Xi'an Jiaotong University. Her research interests are the numerical electromagnetic methods, antenna designs, and electromagnetic compatibility

Jianguo Wang was born in Jiangsu Province, China, on December 21, 1965. He received the B.S. degree in physics from Nanjing University, Nanjing, China in 1987 and the M.S. degree in physics from the Northwest Institute of Nuclear Technology (NINT), Xi'an Shaanxi, China in 1990, and the Ph.D. degree in electromagnetic theory and microwave techniques from Xidian University, Xi'an, Shaanxi, in 1997. From 1998 to 2000, he conducted his postdoctoral research at the Department of Electrical and Computer Engineering, University of Illinois at Urbana-Champaign. He now serves as a professor at NINT. He also works part-time as a Professor in the School of Electronic and Information Engineering, Xi'an Jiaotong University, Xi'an, China. His research interests mainly include transient electromagnetics, numerical electromagnetic methods, antenna designs, and plasma physics.

A Frequency-Dependent Weakly Conditionally Stable Finite-Difference Time-Domain Method for Dispersive Materials

Juan Chen[1, 2], Jianguo Wang [1, 2]

[1]School of Electronic and Information Engineering
Xi'an Jiaotong University, Xi'an 710049, China
chenjuan0306@yahoo.com.cn

[2]Northwest Institute of Nuclear Technology
P. O. Box 69-15, Xi'an 710024, China

Abstract **-** A frequency-dependent weakly conditionally stable finite-difference time-domain (WCS-FDTD) method for dispersive materials is presented. This method has higher computation efficiency than conventional FDTD method because the time step in this method is only determined by one space discretization. The accuracy of this method is demonstrated by computing the incident field at a planar air-water interface over a wide frequency band including the effects of the frequency-dependent permittivity of water.

Index Terms **-** Dispersive materials, FDTD method, WCS-FDTD method.

I. INTRODUCTION

The finite-difference time-domain (FDTD) method [1] has been proven to be an effective scheme that provides accurate predictions of field behaviors for varieties of electromagnetic interaction problems. However, as it is based on an explicit finite-difference algorithm, the Courant–Friedrich–Levy (CFL) condition [2] must be satisfied when this method is used. Therefore, a maximum time-step size is limited by the minimum cell size in a computational domain, which makes this method inefficient for the problems where fine scale structures are involved.

To overcome the CFL constraint on the time step size of the FDTD method, some unconditionally stable methods [3-6] and weakly conditionally stable (WCS) [7-21] schemes have been studied, among which, the WCS-FDTD method scheme, has been applied extensively [15-21]. In the WCS-FDTD method, the time step size is only determined by one space discretization, which is useful for problems with very fine structures in two directions. The accuracy and efficiency of this method have been well validated in [17] and [18].

In this paper, the WCS-FDTD method will be extended to frequency-dependent materials. The formulations of WCS-FDTD for a frequency-dependent complex permittivity are presented and an example calculation of the incident field at a planar air-water interface over a wide frequency band is showed. The extension of the WCS-FDTD method to frequency-dependent permeability is similar and straightforward.

II. FORMULATIONS

For this paper, we will assume that our materials are linear and isotropic, and only the permittivity is frequency-dependent. Extension to nonlinear or anisotropic dispersive materials should be possible. The displacement vector D is related to the electric field E in the time domain by the following equation:

$$D(t) = \varepsilon_\infty \varepsilon_0 E(t) + \varepsilon_0 \int_0^t E(t-\tau)\chi(\tau)\,d\tau. \tag{1}$$

ε_0 is permittivity of free space, $\chi(\tau)$ is the electric susceptibility, and ε_∞ is the infinite frequency relative permittivity.

Using Yee's notation, we let $t = n\Delta t$ in (1), and each vector component of D and E can be written as:

$$D(t) \approx D(n\Delta t) = D^n = \varepsilon_\infty \varepsilon_0 E^n + \varepsilon_0 \int_0^{n\Delta t} E(n\Delta t - \tau)\chi(\tau)d\tau. \quad (2)$$

All field components are assumed to be constant over each time interval $\Delta t/2$. Therefore, we have, assuming $D(t)$ and $E(t)$ are zero for $t < 0$:

$$D^n = \varepsilon_\infty \varepsilon_0 E^n + \varepsilon_0 \sum_{m=0}^{2n-1} E^{n-m/2} \int_{m\Delta t/2}^{(m+1)\Delta t/2} \chi(\tau)d\tau. \quad (3)$$

$$D^{n+1/2} = \varepsilon_\infty \varepsilon_0 E^{n+1/2} + \varepsilon_0 \sum_{m=0}^{2n} E^{n+1/2-m/2} \int_{m\Delta t/2}^{(m+1)\Delta t/2} \chi(\tau)d\tau. \quad (4)$$

$$D^{n+1} = \varepsilon_\infty \varepsilon_0 E^{n+1} + \varepsilon_0 \sum_{m=0}^{2n+1} E^{n+1-m/2} \int_{m\Delta t/2}^{(m+1)\Delta t/2} \chi(\tau)d\tau. \quad (5)$$

When (3) is substituted in (4), and (4) is substituted in (5), we find:

$$D^{n+1/2} - D^n = \varepsilon_\infty \varepsilon_0 \left[E^{n+1/2} - E^n\right] + \varepsilon_0 E^{n+1/2} \int_0^{\Delta t/2} \chi(\tau)d\tau + \varepsilon_0 \sum_{m=0}^{2n-1} E^{n-m/2} \left\{ \begin{array}{l} \int_{(m+1)\Delta t/2}^{(m+2)\Delta t/2} \chi(\tau)d\tau \\ -\int_{m\Delta t/2}^{(m+1)\Delta t/2} \chi(\tau)d\tau \end{array} \right\}. \quad (6)$$

$$D^{n+1} - D^{n+1/2} = \varepsilon_\infty \varepsilon_0 \left[E^{n+1} - E^{n+1/2}\right] + \varepsilon_0 E^{n+1} \int_0^{\Delta t/2} \chi(\tau)d\tau + \varepsilon_0 \sum_{m=0}^{2n} E^{n+1/2-m/2} \left\{ \begin{array}{l} \int_{(m+1)\Delta t/2}^{(m+2)\Delta t/2} \chi(\tau)d\tau \\ -\int_{m\Delta t/2}^{(m+1)\Delta t/2} \chi(\tau)d\tau \end{array} \right\}. \quad (7)$$

For simplicity, we let:

$$\chi_m = \int_{m\Delta t/2}^{(m+1)\Delta t/2} \chi(\tau)d\tau. \quad (8)$$

$$\Delta\chi_m = \chi_m - \chi_{m+1}. \quad (9)$$

Then, we have:

$$E^{n+1/2} = \varepsilon_\infty E^n \Big/ (\varepsilon_\infty + \chi_0) + \sum_{m=0}^{2n-1} E^{n-m/2} \Delta\chi_m \Big/ (\varepsilon_\infty + \chi_0) + \left(D^{n+1/2} - D^n\right) \Big/ (\varepsilon_\infty + \chi_0)\varepsilon_0. \quad (10)$$

$$E^{n+1} = \varepsilon_\infty E^{n+1/2} \Big/ (\varepsilon_\infty + \chi_0) + \sum_{m=0}^{2n} E^{n+1/2-m/2} \Delta\chi_m \Big/ (\varepsilon_\infty + \chi_0) + \left(D^{n+1} - D^{n+1/2}\right) \Big/ (\varepsilon_\infty + \chi_0)\varepsilon_0. \quad (11)$$

The three scalar equations that relate the components of electric field E can be readily obtained from the WCS-FDTD method:

$$\begin{aligned} E_x^{n+\frac{1}{2}}\left(i+\frac{1}{2}, j, k\right) = & \frac{\varepsilon_\infty}{(\varepsilon_\infty + \chi_0)} E_x^n\left(i+\frac{1}{2}, j, k\right) \\ & + \frac{1}{(\varepsilon_\infty + \chi_0)} \sum_{m=0}^{2n-1} E_x^{n-\frac{m}{2}}\left(i+\frac{1}{2}, j, k\right)\Delta\chi_m \\ & + \frac{\Delta t}{(\varepsilon_\infty + \chi_0)\varepsilon_0} \frac{1}{\Delta y} \left[\begin{array}{l} H_z^n\left(i+\frac{1}{2}, j+\frac{1}{2}, k\right) \\ -H_z^n\left(i+\frac{1}{2}, j-\frac{1}{2}, k\right) \end{array} \right] \\ & - \frac{\Delta t}{(\varepsilon_\infty + \chi_0)\varepsilon_0} \frac{1}{2\Delta z} \left[\begin{array}{l} H_y^{n+\frac{1}{2}}\left(i+\frac{1}{2}, j, k+\frac{1}{2}\right) \\ -H_y^{n+\frac{1}{2}}\left(i+\frac{1}{2}, j, k-\frac{1}{2}\right) \\ +H_y^n\left(i+\frac{1}{2}, j, k+\frac{1}{2}\right) \\ -H_y^n\left(i+\frac{1}{2}, j, k-\frac{1}{2}\right) \end{array} \right]. \end{aligned} \quad (12)$$

$$
\begin{aligned}
&E_y^{n+\frac{1}{2}}\left(i, j+\frac{1}{2}, k\right) \\
&=\frac{\varepsilon_\infty}{\left(\varepsilon_\infty+\chi_0\right)} E_y^n\left(i, j+\frac{1}{2}, k\right) \\
&+\frac{1}{\left(\varepsilon_\infty+\chi_0\right)} \sum_{m=0}^{2n-1} E_y^{n-\frac{m}{2}}\left(i, j+\frac{1}{2}, k\right) \Delta \chi_m \\
&-\frac{\Delta t}{\left(\varepsilon_\infty+\chi_0\right) \varepsilon_0} \frac{1}{2 \Delta x}\left[\begin{array}{l}
H_z^{n+\frac{1}{2}}\left(i+\frac{1}{2}, j+\frac{1}{2}, k\right) \\
-H_z^{n+\frac{1}{2}}\left(i-\frac{1}{2}, j+\frac{1}{2}, k\right) \\
+H_z^n\left(i+\frac{1}{2}, j+\frac{1}{2}, k\right) \\
-H_z^n\left(i-\frac{1}{2}, j+\frac{1}{2}, k\right)
\end{array}\right].
\end{aligned} \tag{13}
$$

$$
\begin{aligned}
&E_z^{n+\frac{1}{2}}\left(i, j, k+\frac{1}{2}\right) \\
&=\frac{\varepsilon_\infty}{\left(\varepsilon_\infty+\chi_0\right)} E_z^n\left(i, j, k+\frac{1}{2}\right)+ \\
&\frac{1}{\left(\varepsilon_\infty+\chi_0\right)} \sum_{m=0}^{2n-1} E_z^{n-\frac{m}{2}}\left(i, j, k+\frac{1}{2}\right) \Delta \chi_m .
\end{aligned} \tag{14}
$$

$$
\begin{aligned}
&E_x^{n+1}\left(i+\frac{1}{2}, j, k\right) \\
&=\frac{\varepsilon_\infty}{\left(\varepsilon_\infty+\chi_0\right)} E_x^{n+\frac{1}{2}}\left(i+\frac{1}{2}, j, k\right) \\
&+\frac{1}{\left(\varepsilon_\infty+\chi_0\right)} \sum_{m=0}^{2n} E_z^{n+\frac{1}{2}-\frac{m}{2}}\left(i+\frac{1}{2}, j, k\right) \Delta \chi_m .
\end{aligned} \tag{15}
$$

$$
\begin{aligned}
&E_y^{n+1}\left(i, j+\frac{1}{2}, k\right) \\
&=\frac{\varepsilon_\infty}{\left(\varepsilon_\infty+\chi_0\right)} E_y^{n+\frac{1}{2}}\left(i, j+\frac{1}{2}, k\right) \\
&+\frac{1}{\left(\varepsilon_\infty+\chi_0\right)} \sum_{m=0}^{2n} E_y^{n+\frac{1}{2}-\frac{m}{2}}\left(i, j+\frac{1}{2}, k\right) \Delta \chi_m \\
&+\frac{\Delta t}{\left(\varepsilon_\infty+\chi_0\right) \varepsilon_0} \frac{1}{2 \Delta z}\left[\begin{array}{l}
H_x^{n+1}\left(i, j+\frac{1}{2}, k+\frac{1}{2}\right) \\
-H_x^{n+1}\left(i, j+\frac{1}{2}, k-\frac{1}{2}\right) \\
+H_x^{n+\frac{1}{2}}\left(i, j+\frac{1}{2}, k+\frac{1}{2}\right) \\
-H_x^{n+\frac{1}{2}}\left(i, j+\frac{1}{2}, k-\frac{1}{2}\right)
\end{array}\right].
\end{aligned} \tag{16}
$$

$$
\begin{aligned}
&E_z^{n+1}\left(i, j, k+\frac{1}{2}\right) \\
&=\frac{\varepsilon_\infty}{\left(\varepsilon_\infty+\chi_0\right)} E_z^{n+\frac{1}{2}}\left(i, j, k+\frac{1}{2}\right) \\
&+\frac{1}{\left(\varepsilon_\infty+\chi_0\right)} \sum_{m=0}^{2n} E_z^{n+\frac{1}{2}-\frac{m}{2}}\left(i, j, k+\frac{1}{2}\right) \Delta \chi_m \\
&-\frac{\Delta t}{\left(\varepsilon_\infty+\chi_0\right) \varepsilon_0} \frac{1}{\Delta y}\left[\begin{array}{l}
H_x^{n+\frac{1}{2}}\left(i, j+\frac{1}{2}, k+\frac{1}{2}\right) \\
-H_x^{n+\frac{1}{2}}\left(i, j-\frac{1}{2}, k+\frac{1}{2}\right)
\end{array}\right] \\
&+\frac{\Delta t}{\left(\varepsilon_\infty+\chi_0\right) \varepsilon_0} \frac{1}{2 \Delta x}\left[\begin{array}{l}
H_y^{n+1}\left(i+\frac{1}{2}, j, k+\frac{1}{2}\right) \\
-H_y^{n+1}\left(i-\frac{1}{2}, j, k+\frac{1}{2}\right) \\
+H_y^{n+\frac{1}{2}}\left(i+\frac{1}{2}, j, k+\frac{1}{2}\right) \\
-H_y^{n+1/2}\left(i-\frac{1}{2}, j, k+\frac{1}{2}\right)
\end{array}\right].
\end{aligned} \tag{17}
$$

It can be seen from these equations that equations (12), (13), (16), and (17) can't be used for direct numerical calculation, because they all include the unknown components defined at the same time, thus, modified equations are derived from the original equations.

Updating of $E_x^{n+1/2}$ component, as shown in equation (12), needs the unknown $H_y^{n+1/2}$ component at the same time. In the nonmagnetic media, the updating for H component is unchanged. The equation of the $H_y^{n+1/2}$ component in the WCS-FDTD method is as follows:

$$
\begin{aligned}
&H_y^{n+\frac{1}{2}}\left(i+\frac{1}{2}, j, k+\frac{1}{2}\right) \\
&=H_y^n\left(i+\frac{1}{2}, j, k+\frac{1}{2}\right) \\
&-\frac{\Delta t}{2 \mu \Delta z}\left[\begin{array}{l}
E_x^{n+\frac{1}{2}}\left(i+\frac{1}{2}, j, k+1\right) \\
-E_x^{n+1/2}\left(i+\frac{1}{2}, j, k\right) \\
+E_x^n\left(i+\frac{1}{2}, j, k+1\right) \\
-E_x^n\left(i+\frac{1}{2}, j, k\right)
\end{array}\right].
\end{aligned} \tag{18}
$$

Thus the $E_x^{n+1/2}$ component has to be updated implicitly. Substituting equation (18) into equation (12), the equation for $E_x^{n+1/2}$ field is given as,

$$\begin{aligned}
&(1+2\eta s)E_x^{n+1/2}\left(i+\frac{1}{2},j,k\right)\\
&-\eta s E_x^{n+1/2}\left(i+\frac{1}{2},j,k+1\right)\\
&-\eta s E_x^{n+1/2}\left(i+\frac{1}{2},j,k-1\right)\\
&=\eta\varepsilon_\infty E_x^{n}\left(i+\frac{1}{2},j,k\right)\\
&+\eta\sum_{m=0}^{2n-1}E_x^{n-\frac{m}{2}}\left(i+\frac{1}{2},j,k\right)\Delta\chi_m\\
&-2\eta s E_x^{n}\left(i+\frac{1}{2},j,k\right)\\
&+\eta s E_x^{n}\left(i+\frac{1}{2},j,k+1\right)\\
&+\eta s E_x^{n}\left(i+\frac{1}{2},j,k-1\right)\\
&+\eta\frac{\Delta t}{\varepsilon\Delta y}\begin{bmatrix}H_z^n\left(i+\frac{1}{2},j+\frac{1}{2},k\right)\\-H_z^n\left(i+\frac{1}{2},j-\frac{1}{2},k\right)\end{bmatrix}\\
&-\eta\frac{\Delta t}{\varepsilon\Delta z}\begin{bmatrix}H_y^n\left(i+\frac{1}{2},j,k+\frac{1}{2}\right)\\-H_y^n\left(i+\frac{1}{2},j,k-\frac{1}{2}\right)\end{bmatrix}
\end{aligned}\qquad (19)$$

where $\eta=1/(\varepsilon_\infty+\chi_0)$. $s=\Delta t^2/4\varepsilon\mu\Delta z^2$.

The stability condition of the frequency dependent WCS-FDTD method is same as that of standard WCS-FDTD method,

$$\Delta t\le\frac{\Delta y}{c}. \qquad (20)$$

Because in the frequency-dependent WCS-FDTD method equation, only a summation is added, it does not affect the stability condition.

The stability condition of the frequency dependent WCS-FDTD method will be validated by numerical example in the next section.

III. NUMERICAL VALIDATION

In order to demonstrate the validity and accuracy of the above formulation, a small current source incident at a planar air-water interface is presented here. The geometric configuration of the numerical simulation is shown in Fig.1. The dimension of the perfect-electric-conductor box is 15cm ×3cm ×3cm. The water with the height 1.5cm is filled in the box. A small current source applied along *y* direction is placed at the upper part of the box. The time dependence of the excitation function is:

$$g(t)=\exp[-4\pi(t-t_0)^2/t_1^2] \qquad (21)$$

where t_0 and t_1 are constants, and both equal to 0.6×10^{-9}. The observation point B is set at the water, and 2.4 cm far from the source point A.

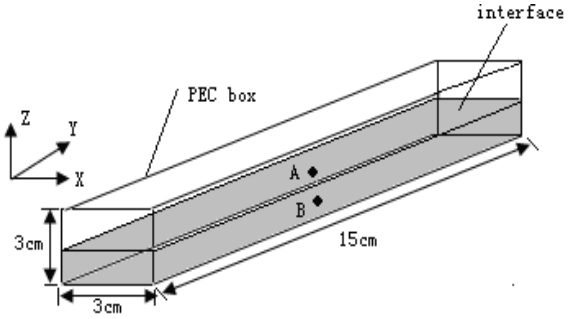

Fig. 1. Geometric configuration of the numerical simulation.

Applying the FDTD method to compute the time domain electric field component E_y at observation point B, the cell size is chosen as $\Delta y=5\Delta x=5\Delta z=$ 0.5cm, so that the computational domain is 30 ×30 ×30 cells. To satisfy the stability condition of the FDTD algorithm, the time-step size for conventional FDTD [22] is $\Delta t\le2.33$ps. For the WCS-FDTD scheme, the maximum time increment is only related to the space increments Δy , that is, $\Delta t\le16.66$ ps.

For water, the complex permittivity $\varepsilon^*(\omega)$ can be described as

$$\varepsilon^*(\omega)=\varepsilon_0\left[\varepsilon_\infty+(\varepsilon_s-\varepsilon_\infty)/(1+j\omega\tau_0)\right] \qquad (22)$$

where ε_s is the "static" permittivity, and τ_0 is the "relaxation time" constant. The water parameters used here are ε_s =81, ε_∞ =1.8, and $\tau_0=9.4\times10^{-12}$.

The summation (convolution) term of equations (10) and (11) can be updated recursively by

utilizing equation (20) in [21], because the susceptibility function is an exponential. So, it does not require storing a large number of past time values E^n, and the computational time is saved. Only one additional number needs to be stored for each electric field component at each spatial index.

First, we validate the numerical stability of equation (19). Figure 2 shows the electric field component E_y at observation point B calculated by using the WCS-FDTD methods with the time-step size Δt =16.66 ps for a long time history. No instability problem is observed even for 5,000 time steps, which validates the weakly conditional stability of the WCS-FDTD method numerically.

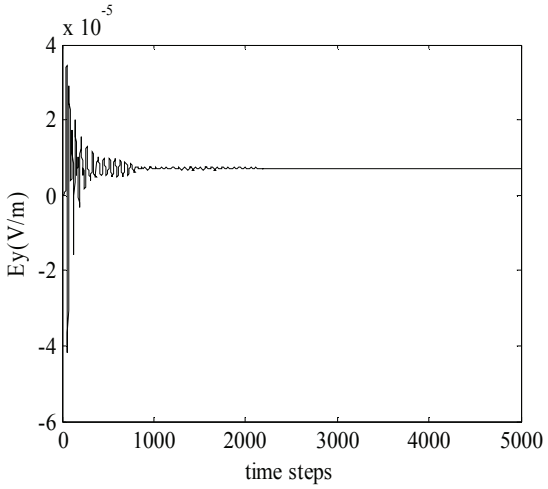

Fig. 2. The electric field component E_y at observation point B calculated by using the WCS -FDTD method with the time-step size Δt =16.66ps for a long time story.

To demonstrate the high computational efficiency of WCS-FDTD method, we perform the numerical simulations for an 8 ns time history by using the conventional FDTD, and WCS-FDTD methods, and compare the CPU times taken by using these two methods. In the conventional FDTD method, the time-step size is 2.33 ps, while in the WCS-FDTD method, the time step size is 16.66ps.

Figures 3 and 4 show the electric field component E_y in the time domain and frequency domain at observation point B calculated by using the conventional FDTD, and WCS-FDTD methods. It can be seen from these figures that the result calculated by the WCS-FDTD method agrees with the result calculated by the conventional FDTD method. The WCS-FDTD method has almost the same accuracy as that of the conventional FDTD method, while, the simulation takes 206.94 s for the conventional FDTD method and 56.79s for the WCS-FDTD method. The time cost for the WCS-FDTD simulation is almost 1/4 times as that for the conventional FDTD simulation. So, we can conclude that the WCS-FDTD has higher efficiency than the conventional FDTD method, due to the use of larger time step size.

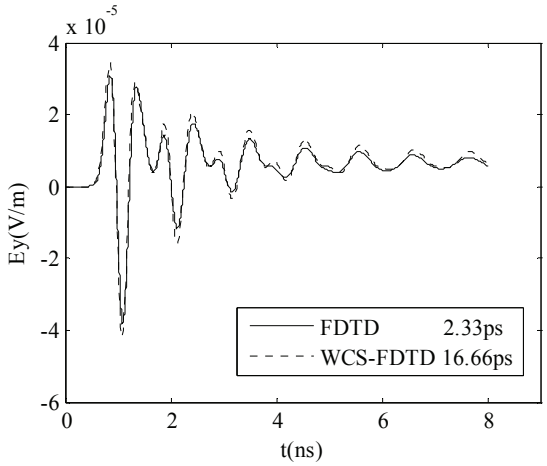

Fig. 3. The electric field component E_y in the time domain at observation point B calculated by using the conventional FDTD (Δt =2.33ps), and WCS-FDTD methods (Δt =16.66ps).

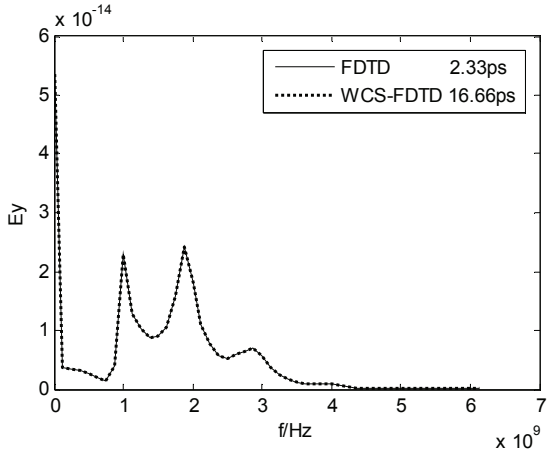

Fig. 4. The electric field component E_y in the frequency domain at observation point B calculated by using the conventional FDTD $(\Delta t = 2.33\text{ps})$, and WCS-FDTD methods (Δt =16.66ps).

IV. CONCLUSION

A frequency-dependent WCS-FDTD method for dispersive materials is presented. It is found that the technique is weakly conditionally stable and supports time steps greater than the CFL limit. Numerical example demonstrates that the computation efficiency of the WCS-FDTD method is higher than the conventional FDTD method, and the accuracy of the WCS-FDTD is almost the same as that of the conventional FDTD method.

ACKNOWLEDGMENT

This work was supported by the Research Fund for the Doctoral Program of Higher Education of China (20090201120030), and also supported by the Basic Fund of Xi'an Jiaotong University.

REFERENCES

[1] K. S. Yee, "Numerical solution of initial boundary value problems involving Maxwell's equations in isotropic media," *IEEE Trans. Antennas Propagat.*, vol. 14, pp. 302–307, May 1966.

[2] A. Taflove, *Computational Electrodynamics,* Artech House, 1995.

[3] F. Zheng, Z. Chen, and J. Zhang, "A finite-difference time-domain method without the Courant stability conditions," *IEEE Microwave Guided. Wave Lett.*, vol. 9, pp. 441–443, Nov. 1999.

[4] T. Namiki, "3-D ADI-FDTD scheme-unconditionally stable time-domain algorithm for solving full vector Maxwell's equations," *IEEE Trans. Microwave Theory Tech.*, vol. 48, pp.1743–1748, Oct. 2000.

[5] J. Chen and J. Wang, "Error between unconditionally stable FDTD methods and conventional FDTD method," *Electon. Lett*., vol. 42, pp. 1132-1133, Sep. 2006.

[6] J. Chen and J. Wang, "PEC condition implementation for the ADI-FDTD method," *Microwave Opt. Tech. Lett.*, vol. 49, pp. 526-530, Mar. 2007.

[7] J. Chen and J. Wang, "A 3D hybrid implicit-explicit FDTD scheme with weakly conditional stability," *Microwave Opt. Technol. Lett.,* vol. 48, pp. 2291-2294, Nov. 2006.

[8] J. Chen and J. Wang, "Comparison between HIE-FDTD method and ADI-FDTD method," *Microwave Opt. Technol. Lett.,* vol. 49, pp. 1001-1005, May 2007.

[9] J. Chen and J. Wang, "A three-dimensional semi-implicit FDTD scheme for calculation of shielding effectiveness of enclosure with thin slots," *IEEE Trans. Electromagn. Compat.,* vol. 49, pp. 354-360, May 2007.

[10] J. Chen and J. Wang, "Numerical simulation using HIE–FDTD method to estimate various antennas with fine scale structures," *IEEE Trans. Antennas Propagat.*, vol. 55, pp. 3603-3612, Dec. 2007.

[11] I. Ahmed and E. Li, "Conventional perfectly matched layer for weakly conditionally stable hybrid implicit and explicit-FDTD method," *Microwave Opt. Technol. Lett.*, vol. 49, pp. 3106-3109, Dec. 2007.

[12] J. Chen and J. Wang, "Implementation of connection boundary for HIE-FDTD method," *Microwave Opt. Technol. Lett.*, vol. 50, pp. 1347-1352, May 2008.

[13] J. Chen and J. Wang, "The body-of-revolution hybrid implicit-explicit finite-difference time-domain method with large time step size," *IEEE Trans. Electromagn. Compat.*, vol. 50, pp. 369-374, May 2008.

[14] F. Xiao, X. Tang, and L. Wang, "Stability and numerical dispersion analysis of a 3D hybrid implicit-explicit FDTD method," *IEEE Trans. Antennas Propag.,* vol. 56, pp. 3346-3350, Oct. 2008.

[15] J. Chen and J. G. Wang, "Weakly conditionally stability FDTD scheme with reduced split error," *Electron. Lett.*, vol. 42, pp.1017-1019, Aug. 2006.

[16] J. Chen and J. G. Wang, "A novel 3-D FDTD method with weakly conditional stability," *Electron. Lett.*, vol. 43, pp. 2-3, Jan. 2007.

[17] J. Chen and J. Wang, "A novel WCS-FDTD method with weakly conditional stability," *IEEE Trans. Electromagn. Compat*., vol. 49, pp. 419-426, May 2007.

[18] J. Chen and J. Wang, "Using WCS-FDTD method to simulate various small aperture-coupled metallic enclosures," *Microwave Opt. Technol. Lett*., vol. 49, pp.

1852-1858, Aug. 2007.

[19] J. Chen and J. Wang, "A new method to avoid the reduction of the time step in CP-FDTD method," *IEEE Trans. Antennas Propag.,* vol. 55, pp. 3613-3619, Dec. 2007.

[20] J. Chen and J. Wang, "A novel body-of-revolution finite-difference time-domain method with weakly conditional stability," *IEEE Microwave Wire Comp. Lett.,* vol. 16, pp. 377-379, Jun. 2008.

[21] R. Luebbers, F. P. Hunsberger, K. S. Kunz, R. B. Standler, and M. Schneider, "A frequency-dependent finite-difference time-domain formulation for dispersive materials," *IEEE Trans Electromagn. Compat*, vol. 32, pp. 222-227, Aug. 1990.

Juan Chen was born in Chongqing, China, in 1981. She received the B.S. degree in Public Security Protection Engineering from Chinese People Public- Security University, Beijing, China in 2003 and the Ph.D. degree in electromagnetic field and microwave techniques from Xi'an Jiaotong University, Xi'an, China in 2008. She now serves as a lecturer in the School of Electronic and Information Engineering, Xi'an Jiaotong University. Her research interests are the numerical electromagnetic methods, antenna designs, and electromagnetic compatibility.

Jianguo Wang was born in Jiangsu Province, China, on December 21, 1965. He received the B.S. degree in physics from Nanjing University, Nanjing, China in 1987 and the M.S. degree in physics from the Northwest Institute of Nuclear Technology (NINT), Xi'an Shaanxi, China in 1990, and the Ph.D. degree in electromagnetic theory and microwave techniques from Xidian University, Xi'an, Shaanxi, in 1997. From 1998 to 2000, he conducted his postdoctoral research at the Department of Electrical and Computer Engineering, University of Illinois at Urbana-Champaign. He now serves as a professor at NINT. He also works part-time as a Professor in the School of Electronic and Information Engineering, Xi'an Jiaotong University, Xi'an, China. His research interests mainly include transient electromagnetics, numerical electromagnetic methods, antenna designs, and plasma physics.

Reconstruction of the Buried Homogenous Dielectric Cylinder by FDTD and Asynchronous Particle Swarm Optimization

Chung-Hsin Huang[1], Chien-Hung Chen[1], Chien-Ching Chiu[2] and Ching-Lieh Li[2]

[1] Department of Computer and Communication Engineering, Taipei College of Maritime Technology
Danshui Town, Taipei County, Taiwan, R.O.C.
chhuang@mail.tcmt.edu.tw, f1092@mail.tcmt.edu.tw

[2] Electrical Engineering Department, Tamkang University
Tamsui, Taiwan, R.O.C.
chiu@ee.tku.edu.tw, li@ee.tku.edu.tw

Abstract **-** In this paper, a time domain microwave imaging technique for reconstructing the electromagnetic properties of a buried homogeneous dielectric cylinder based on the finite difference time domain (FDTD) method and the asynchronous particle swarm optimization (APSO) are presented. The homogeneous dielectric cylinder with unknown electromagnetic properties is illuminated by transverse magnetic pulse and the scattered field is recorded outside. The idea is to minimize the errors between two *E* field data such that the location, shape and permittivity of the dielectric cylinder can be reconstructed through the APSO scheme. The first *E* field data are obtained in the forward problem by the FDTD code with fine grids to mimic the experiment measurement data, while the second *E* field data are obtained in the inverse problem by the FDTD code with coarse grids. The inverse problem is resolved by an optimization approach, and the global searching scheme APSO is then employed to search the parameter space. A set of representative numerical results is presented for demonstrating that the proposed approach is able to efficiently reconstruct the electromagnetic properties of homogeneous dielectric scatterer even when the initial guess is far away from the exact one. In addition, the effects of Gaussian noises on imaging reconstruction are also investigated.

Index Terms **-** APSO, FDTD, inverse scattering, subgridding FDTD, time domain.

I. INTRODUCTION

The objective of the inverse problem of the buried scatterer is to determine the electromagnetic properties of the scatterer from the scattering field outside. Due to the large domain of applications, such as non-destructive problems, medical imaging, geophysical prospecting and determination of underground tunnels and pipelines, etc, the inverse scattering problems related to the buried bodies have particular importance in the scattering theory. This kind of problem is expected to be more difficult due to the fact that the information about the buried unknown scatterer obtained by the limited–view measurement is less than the full-view measurement. Although the incompleteness of the measurement data and the multiple scattering of the scatterer bring out the intrinsic non-unique and ill-posedness of these problems that appear consequentially in the inverse scattering problems [1], the study can be applied in widespread use.

Most of the previously proposed inversion techniques for the inverse problems are formulated in the frequency domain [2-5]. However, the time domain scattering scheme is a potential alternative for the inverse problem because the data contain more information than those in the frequency case. Therefore, various time domain inversion approaches are proposed intensively in recent decades that could be briefly classified as the iterative approach: Born iterative method (BIM) [6], the distorted Born iterative method (DBIM) [7] and optimization approach [8, 9]. The inverse scattering problems are usually treated by the

traditional deterministic methods which are founded on a functional minimization via some gradient-type scheme. The major drawback of these kinds of deterministic methods is that the final reconstructed image is highly dependent on the initial trial guess [2, 3]. In general, they tend to get trapped in local minima when the initial trial solution is far from the exact one. Thus, some population-based stochastic methods, such as the genetic algorithm (GA) [4, 5, 10, 11], differential evolution (DE) [12-14], and particle swarm optimization (PSO) [14-17], are proposed to search the global extreme of the inverse problems to overcome the drawback of the deterministic methods. Rekanos et al. shows that asynchronous mode PSO (APSO) outperforms traditional synchronous mode PSO in reconstructed image quality. To the best of our knowledge, there is still no investigation using the APSO to reconstruct the electromagnetic imaging of homogeneous dielectric cylinders with arbitrary shape in half space based on a time domain method.

In this paper, the computational method combining the FDTD method [18] and the PSO algorithm with asynchronous updating scheme is presented. The forward problem is solved by the FDTD method, for which the subgridding technique [19] is implemented to closely describe the fine structure of the cylinder. The cross section shape of scatterer is parameterized by closed cubic spline expansion. The inverse problem is formulated into an optimization one and then the global searching scheme APSO is used to search the parameter space. In Section II, the theoretical formulation for the electromagnetic imaging is presented. The detail principle of the APSO and the way we applied them to the imaging problem are described. In Section III, numerical results for various dielectric objects are given, and the effect of noise is also investigated. Finally, some conclusions are drawn in Section IV.

II. THEORETICAL FORMULATION

Consider a 2-D homogeneous dielectric cylinder buried in a half space material medium as shown in Fig. 1. The cylinder is parallel to the z axis and is buried below a planar interface separating two homogeneous half spaces: the air (ε_1, μ_1) and the earth (ε_2, μ_2). The permittivity and permeability of the buried dielectric object are denoted by (ε_3, μ_3), respectively. The dielectric object is illuminated by a line source with Gaussian pulse shape placed at two different positions sequentially denoted by Tx in the first layer, and then scattered waves are recorded at those points denoted simultaneously by Rx in the same layer.

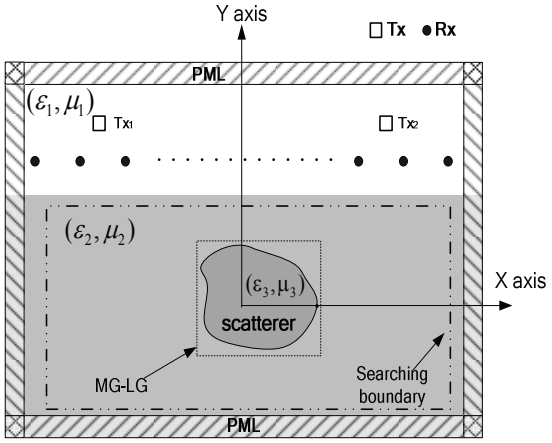

Fig. 1. Geometry for the inverse scattering of a dielectric cylinder of arbitrary shape in half space.

The shape of the cross section of the object is starlike and can be represented in polar coordinates with respect to the logic origin (X_O, Y_O) in the x-y plane as shown in Fig. 2. The computational domain is discretized by Yee cells. It should be mentioned that the computational domain is surrounded by the optimized perfect matching layers (PML) absorber [20] to reduce the reflection from the environment PML interface.

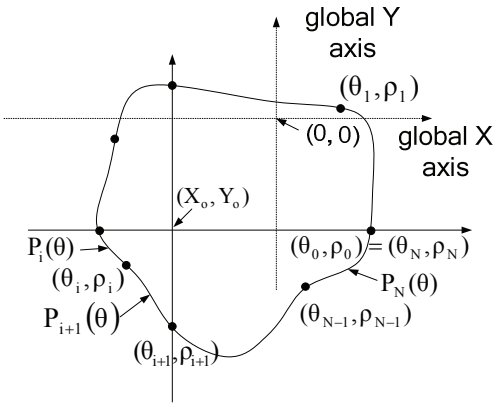

Fig. 2. A cylinder of arbitrary shape is described in terms of a closed cubic spline.

A. Forward problem

As mentioned in the abstract, the first *E* field data need to be obtained in the forward scattering problem by the FDTD code with fine grids to mimic the experimental measurement data. For the forward scattering problem the shape, location and permittivity of the dielectric cylinder to be determined is given first, and then the FDTD code is employed to calculate the scattered electric fields that are utilized to mimic the experiments. It should be noted that in the forward problem, the shape function $F(\theta)$ of the 2-D homogeneous dielectric cylinder buried in a half space is described by the trigonometric series as follows:

$$F(\theta)=\sum_{n=0}^{N/2}B_n\cos(n\theta)+\sum_{n=1}^{N/2}C_n\sin(n\theta). \qquad (1)$$

In order to closely describe the shape of the cylinder for both the forward and inverse scattering procedure, the subgridding technique is implemented in the FDTD code, the details are presented in later section.

B. Inverse problem

As mentioned in the abstract, the second *E* field data are obtained in the inverse problem by the FDTD code with coarse grids. As compared with the first *E* field data obtained in the forward scattering procedure, the inverse scattering problem can be formulated into an optimization problem. The proposed global searching APSO scheme is employed to reconstruct the location, shape and permittivity of the dielectric cylinder under test by minimizing the errors between two *E* filed data.

During the course of optimization process, the following objective function (*OF*) is defined for each candidate cylinder in the APSO scheme:

$$OF=\frac{\sum_{n=1}^{N_i}\sum_{m=1}^{M}\sum_{q=0}^{Q}\left|E_z^{exp}(n,m,q\Delta t)-E_z^{cal}(n,m,q\Delta t)\right|}{\sum_{n=1}^{N_i}\sum_{m=1}^{M}\sum_{q=0}^{Q}\left|E_z^{exp}(n,m,q\Delta t)\right|}, \qquad (2)$$

where E_z^{exp} is the electric field data to mimic the measurement as mentioned previously, and E_z^{cal} is the calculated electric fields in the inversion procedure, respectively. The N_i and M are the total number of the transmitters and receivers, respectively. Q is the total time step number of the recorded electric fields. The details of the proposed PSO are represented as follows.

C. Cubic spline interpolation technique

It should be noted that in the inverse problem, the shape function of the 2-D homogeneous dielectric cylinder is described by a cubic spline in this study instead of the trigonometric series described in the section of the forward problem. The cubic spline is more efficient in terms of the unknown number required to describe a cylinder of arbitrary cross section. By using the cubic spline the coordinates of local origin inside the cylinder serve as the searching parameter and can move around the searching space, which is impossible if the trigonometric series expansion is used in the inversion procedure.

As shown in Fig. 2, the cubic spline consists of the polynomials of degree 3 $P_i(\theta)$, $i=1,2,\cdots,N$, which satisfy the following smooth conditions:

$$\begin{aligned} &P_i(\theta_i)=P_{i+1}(\theta_i)\equiv\rho_i \\ &P_i'(\theta_i)=P_{i+1}'(\theta_i),\ i=1,2,\cdots,N \\ &P_i''(\theta_i)=P_{i+1}''(\theta_i), \end{aligned} \qquad (3)$$

and

$$\begin{aligned} &P_1(\theta_0)=P_N(\theta_N) \\ &P_1'(\theta_0)=P_N'(\theta_N)\equiv\rho_N' \\ &P_1''(\theta_0)=P_N''(\theta_N). \end{aligned} \qquad (4)$$

Through the interpolation of the cubic spline, an arbitrary smooth cylinder can be easily described through the radius parameters $\rho_1,\rho_2,\cdots,\rho_N$ and the slope ρ_N', of which the details are referred to [21]. By combining the modified APSO and the cubic spline interpolation technique, we are able to reconstruct the microwave image efficiently.

It should be noted that the coordinates of local origin inside the cylinder plus the radiuses of the geometrical spline used to describe the shape of the cylinder will be determined by the asynchronous PSO scheme later.

D. The modified synchronous particle swarm optimization (APSO)

Particle swarm global optimization is a class of derivative-free, population-based and self-adaptive search optimization technique which we introduced by Kennedy and Eberhart [22]. Particles (potential solutions) are distributed throughout the searching space and their positions and velocities are modified based on social behavior. The social behavior in PSO is a population of particles moving towards the most promising region of the search space. Clerc [23] proposed the constriction factor to adjust the velocity of the particle for obtaining the better convergence; the algorithm was named as constriction factor method. PSO starts with an initial population of potential solutions that is randomly generated and composed N_p individuals (also called particles) which represents the dielectric constant, location and the geometrical radiuses of the cylinders.

After the initialization step, each particle of population has assigned a randomized velocity and position. Thus, each particle has a position and velocity vector, and moves through the problem space. In each generation, the particle changes its velocity by its best experience, called x_{pbest}, and that of the best particle in the swarm, called x_{gbest}.

Assume there are N_p particles in the swarm that is in a search space in D dimensions, the position and velocity could be determined according to the following equations (constriction factor method):

$$v_{id}^{k} = \chi \cdot \left(v_{id}^{k-1} + c_1 \cdot \varphi_1 \cdot \left(x_{pbest,id} - x_{id}^{k-1} \right) + c_2 \cdot \varphi_2 \cdot \left(x_{gbest,id} - x_{id}^{k-1} \right) \right) \tag{5}$$

$$\mathrm{x}_{\mathrm{id}}^{\mathrm{k}} = \mathrm{x}_{\mathrm{id}}^{\mathrm{k-1}} + \mathrm{v}_{\mathrm{id}}^{\mathrm{k}} \ , \tag{6}$$

where $\chi = \dfrac{2}{\left| 2 - \phi - \sqrt{\phi^2 - 4\phi} \right|}$, $\phi = \mathrm{c}_1 + \mathrm{c}_2 \geq 4$.

c_1 and c_2 are learning coefficients, used to control the impact of the local and global component in velocity equation (3). $\mathrm{v}_{\mathrm{id}}^{\mathrm{k}}$ and $\mathrm{x}_{\mathrm{id}}^{\mathrm{k}}$ are the velocity and position of the i-th particle in the d-th dimension at k-th generation, φ_1 and φ_2 are both the random numbers between 0 and 1. It should be mentioned that the V_{max} method is also applied to control the particle's searching velocity and to confine the particle within the search space [24]. The value of V_{max} is set to be half of X_{max}, where X_{max} is the upper limits of the search space. Note that the V_{max} and X_{max} are maximum velocity and maximum distance, respectively. As an extreme case, if the maximum velocity V_{max} is set to X_{max}, the exploration to the inverse scattering problem space is not limited. Occasionally, the particles may move out of their search space. This problem could be remedied by applying the boundary condition to draw the foul particles back to the normal space. In this paper, we apply the "damping boundary condition" proposed by Huang and Mohan [25] to ensure the particles move within the legal search space. The key distinction between asynchronous PSO and a typical synchronous PSO is on the population updating mechanism. In the synchronous PSO, the algorithm updates all the particles velocities and positions using equations (5) and (6) at end of the generation. And then update the best positions, x_{pbest} and x_{gbest}. Alternatively, the updating mechanism of asynchronous PSO is that the new best position is found after each particle position updates, if the best position is better than the current best position. The new best position will be used in following particles swarm immediately. The swarm reacts more quickly to speedup the convergence because the updating occurs immediately after objective function evaluation for each particle.

The flowchart of the modified asynchronous PSO (APSO) is shown in Fig. 3. Asynchronous PSO goes through seven procedures as follows:

I. Initialize a starting population: Randomly generate a swarm of particles.

II. Calculate E fields by a home-made FDTD code.

III. Evaluate the population using objective function: The asynchronous PSO algorithm evaluates the objective function (2) for each individual in the population.

IV. Find x_{pbest} and x_{gbest}.

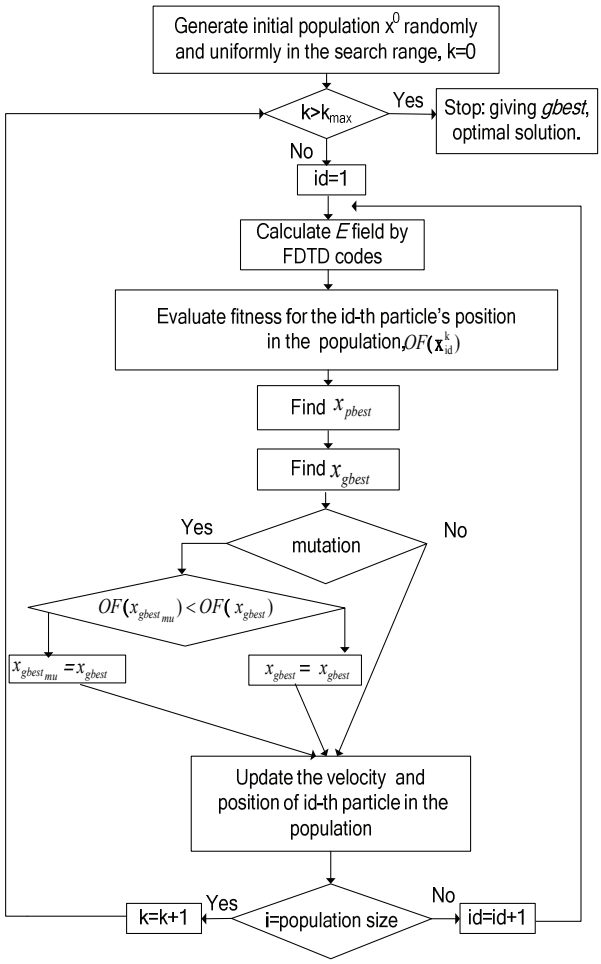

Fig. 3. The flowchart for the modified APSO.

V. Mutation scheme: The particle swarm optimization (PSO) algorithm has been shown to converge rapidly during the initial stages of a global search, but when around global optimum, the search can become very slow. For this reason, mutation scheme is introduced in this algorithm to speed up the convergence when particles are around global optimum. The mutation scheme can also avoid premature convergences in the searching procedure and help the x_{gbest} escape from the local optimal position. As shown in Fig. 3, there is an additional competition between the x_{gbest} and $x_{pbest_{mu}}$. The current x_{gbest} will be replaced by the $x_{gbest_{mu}}$ if the $x_{gbest_{mu}}$ is better than the current x_{gbest}. The $x_{gbest_{mu}}$ is generated by following way:

$$X_{gbest_{mu}} = \begin{cases} X_{gbest} - \varphi_3 \cdot \left[c_3 - (c_3 - c_4) \cdot \frac{k}{k_{\max}} \right] \cdot (x_{\max} - x_{\min}), & \text{if } \varphi_{mu} < 0.5 \\ X_{gbest} + \varphi_3 \cdot \left[c_3 - (c_3 - c_4) \cdot \frac{k}{k_{\max}} \right] \cdot (x_{\max} - x_{\min}), & \text{if } \varphi_{mu} \geq 0.5 \end{cases} \quad (7)$$

where c_3 and c_4 are the scaling parameter. φ_3 and φ_{mu} are both the random numbers between 0 and 1. k is the current iteration number. $k_{\max}$ is the maximum iteration number. $x_{\max}$ and $x_{\min}$ are the upper limit and lower limit of the search space, respectively.

VI. Update the velocity and position.

VII. Stop the process and print the best individual if the termination criterion is satisfied, else go to step II.

III. NUMERICAL RESULTS

In this section, we report some numerical results using the method described in Section II. As shown in Fig. 1, the problem space is divided in 128×68 grids with the grid size $\Delta x = \Delta y$ =5.95 mm. The homogeneous dielectric cylinder is buried in lossless half space ($\sigma_1 = \sigma_2 = 0$). The transmitters and receivers are placed in free space above the homogeneous dielectric. The permittivities in region 1 and region 2 are characterized by $\varepsilon_1 = \varepsilon_0$ and $\varepsilon_2 = 2.3\varepsilon_0$, respectively, while the permeability μ_0 is used for each region, i.e., only non-magnetic media are concerned here. The distance between the half space interface and the original cylinder is 89.2mm. The cylindrical object is illuminated by a transmitter at two different positions, N_t=2, which are located at the (-143mm, 178.5mm) and (143mm, 178.5mm), respectively. The scattered E fields for each illumination are collected at the fifteen receivers, M = 15, which are equally separated by 47.8 mm along the distance of 48 mm from the half space interface. The excitation waveform $I_z(t)$ of the transmitter is the Gaussian pulse, given by:

$$I_z(t) = \begin{cases} Ae^{-\alpha(t-\beta\Delta t)^2}, t \le T_w \\ 0 \quad\quad , t > T_w \end{cases}, \tag{8}$$

where $\beta = 32$, $A = 1000$, $\Delta t = 13.337\, ps$, $T_w = 2\beta\Delta t$, and $\alpha = \left(\frac{1}{4\beta\Delta t}\right)^2$.

The time duration is set to $300\,\Delta t$ ($s = 300$). Note that in order to describe the shape of the cylinder more accurately, the subgridding FDTD technique is employed both in the forward scattering (1:9) and the inverse scattering (1:5) parts – but with different scaling ratios as indicated in the parentheses. For the forward scattering, the *E* fields generated by the FDTD with finer subgrids are used to mimic the experimental data in (2).

The reconstruction ideas are carried out through a home-made Fortran program that runs on an Intel PC (2.83 GHz/ 2G memory /500 G).

Three examples are investigated for the inverse scattering of the proposed structure by using the modified APSO. There are twelve unknown parameters to retrieve, which include the coordinates of local origin (X_O, Y_O) inside the cylinder, the radius ρ_i, $i = 1, 2, \cdots, 8$ of the shape function and the slope ρ'_N plus the relative permittivity of the object, $\varepsilon_r = \varepsilon_3 / \varepsilon_0$. Very wide searching ranges are used for the modified APSO to optimize the cost function given by (2). The parameters and the corresponding searching ranges are listed as follows: $-208.3\text{mm} \le X_O \le 208.3\text{mm}$, $-137.8\text{mm} \le Y_O \le 77.4\text{mm}$, $0\text{mm} \le \rho_i \le 71.4\text{mm}$, $i = 1, 2, \cdots, 8$, $-1 \le \rho'_N \le 1$ and $1 \le \varepsilon_r \le 16$. The relative coefficients of the modified APSO are set as below: The learning coefficients, c_1 and c_2 , are set to 2.8 and 1.3, respectively. The mutation probability is 0.4 and the population size is set to 30.

The first example, a simple circular cylinder is tested, of which the shape function $F(\theta)$ is chosen to be $F(\theta) = 35.7$ mm, and the relative permittivity of the object is $\varepsilon_r = 3.7$. The convergence curves of objective function versus the generation as the proposed APSO being executed seven times out of ten by using different tables of random numbers are shown in Fig. 4. The small converged values show the robustness for the APSO scheme applied this topic.

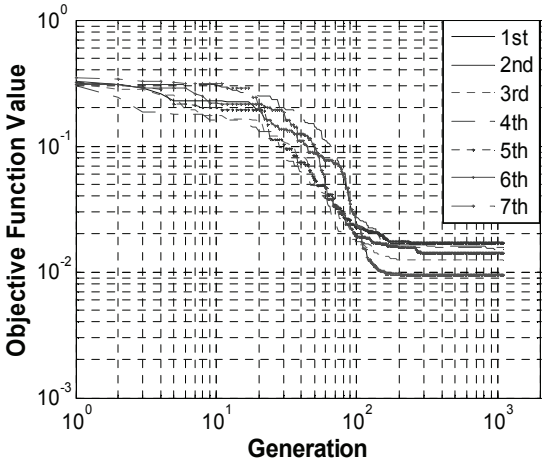

Fig. 4. The objective function value versus generations for example 1 using the Gaussian pulse illumination as the APSO is executed seven times.

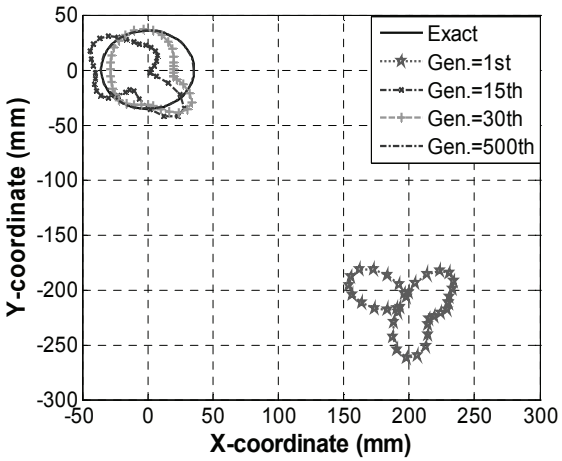

Fig. 5. The reconstructed shape of the cylinder at different generations for example 1.

The reconstructed shape function of the best population member (particle) is plotted in Fig. 5 for different generation. The discrepancy of shape Function (DF) of the reconstructed shape $F^{cal}(\theta)$ and the discrepancy of dielectric constant (DIPE) of ε_r^{cal} with respect to the exact values versus the generation are shown in Figure 6. Here, DF and DIPE are defined as

$$DF = \{\frac{1}{N'}\sum_{i=1}^{N'}[F^{cal}(\theta_i) - F(\theta_i)]^2 / F^2(\theta_i)\}^{1/2}, \quad (9)$$

$$DIPE = \frac{\left|\varepsilon_r^{cal} - \varepsilon_r\right|}{\varepsilon_r}, \quad (10)$$

where the N' is set to 360. The r.m.s. error DF is about 0.84% and DIPE= 0.21%. It is seen that the reconstruction is good.

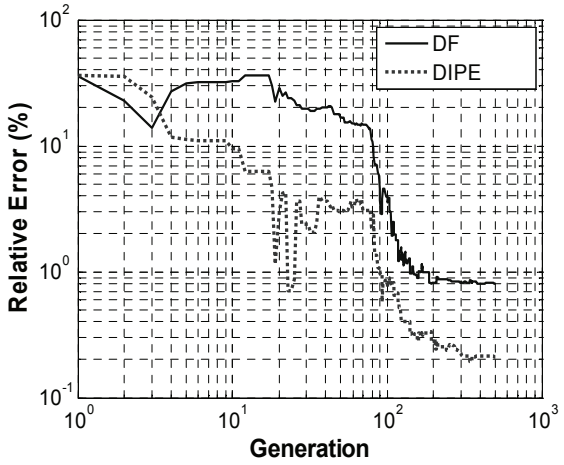

Fig. 6. Shape error and permittivity error versus generation for example 1.

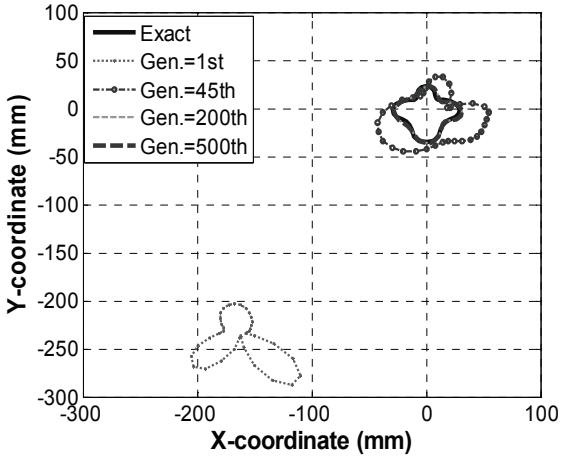

Fig. 7. The reconstructed cross section of the cylinder of example 2 at different generations.

The reconstructed images for different generations and the relative error of the second example are shown in Figs. 7 and 8, respectively. The shape function of this object is given by $F(\theta) = 23.8 - 5.95\sin(\theta) + 5.95\cos(4\theta)$ mm and the relative permittivity of the object is $\varepsilon_r = 6.2$. Figure 8 shows that the relative errors of the shape and the permittivity decrease quickly and good convergences are achieved within 200 generations. It also shows that the permittivity converges faster than the shape function does. The r.m.s. error DF is about 6.65% and DIPE=2.21% in the final generation. From the reconstructed results of this example, we conclude the proposed method is able to reconstruct buried dielectric cylinder successfully when the dielectric object is with high-contrast permittivity.

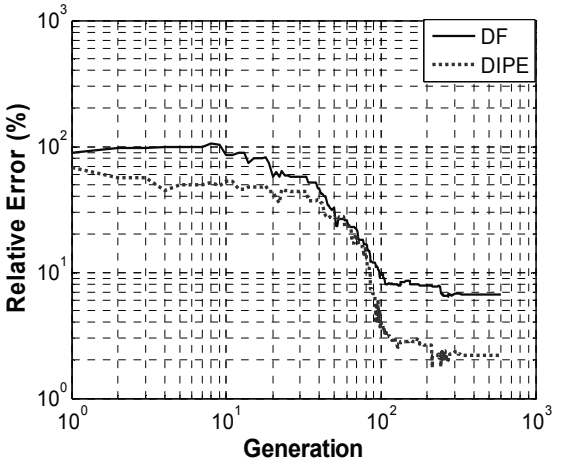

Fig. 8. Shape-function error and permittivity error versus generations for example 2.

In the final example, let us consider the problem for dielectric cylinders with high permittivity. The shape function of this object is given by $F(\theta) = 29.7 + 5.95\sin(2\theta) + 5.95\cos(3\theta) - 5.95\sin(3\theta)$ mm and the relative permittivity of the object is $\varepsilon_r = 3$. The reconstructed images at different generations and the relative error of the final example are shown in Fig. 9 and Fig 10, respectively. As shown in Figure 10, the r.m.s. error DF is about 5% and DIPE=0.20% in the final generations. In order to investigate the sensitivity of the imaging algorithm against random noise, the additive white Gaussian noise of zero mean with standard deviation σ_g is added into the scattered electric fields to mimic the measurement errors. The relative noise level (RNL) is defined as:

$$RNL = \frac{\sigma_g}{\sqrt{\sum_{n=1}^{Ni}\sum_{m=1}^{M}\sum_{k=0}^{K}\left|E_z^{\exp}(n,m,k\Delta t)\right|^2 / (N_i)(M_i)(K-1)}} \quad (11)$$

The relative noise levels of 10^{-4}, 10^{-3}, 10^{-2}, 10^{-1}, 0.2 and 0.5 are used. Fig. 11 shows the reconstructed results under the condition that the scattered E fields to mimic the measurement data are contaminated by the noise. It could be observed that good reconstruction has been obtained for both the relative permittivity and shape of the dielectric cylinder when the relative noise level is below 10^{-1}.

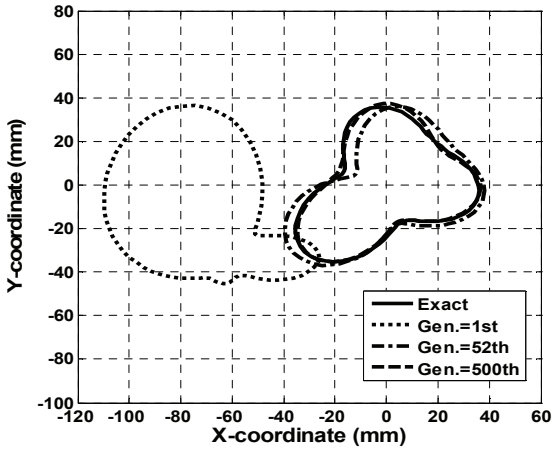

Fig. 9. The reconstructed cross section of the cylinder of example 3 at different generations.

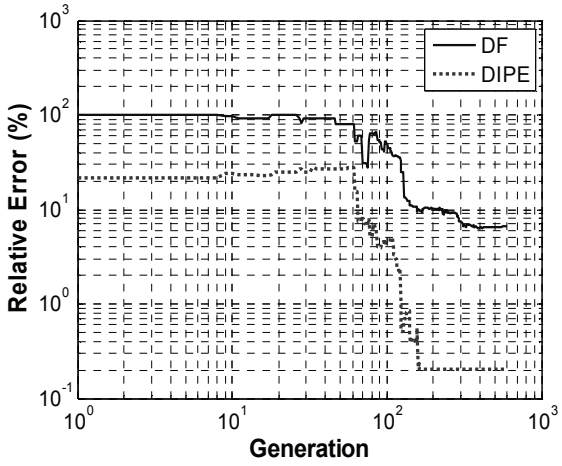

Fig. 10. Shape-function error and permittivity error versus generations for example 3.

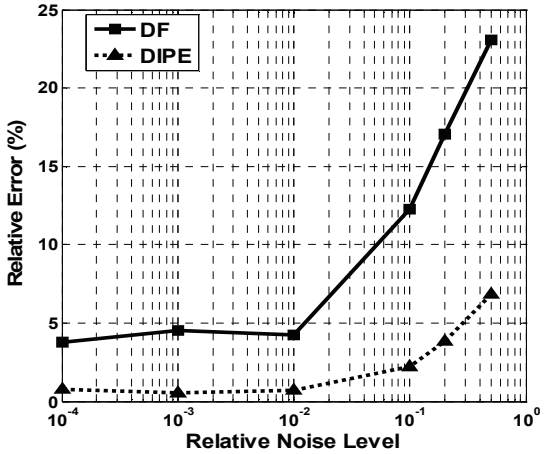

Fig. 11. Shape error and relative permittivity errors as functions of RNL.

IV. CONCLUSION

In this paper, a new numerical approach to microwave imaging of homogeneous dielectric scatterer with arbitrary cross section in time domain has been presented. Scattering fields are obtained by FDTD method. The subgridding scheme is employed to closely describe the shape of the cylinder for the FDTD method. The approach has been formulated as a global nonlinear optimization problem and a modified asynchronous PSO has been applied. It has been shown that the properties of the dielectric object can be successfully reconstructed even when the dielectric object with fairly large permittivity and the Born approximation is no longer valid. In our study, good reconstructed results are obtained even when the initial guess is far from the exact one, while the gradient-based methods often get stuck in a local extreme. Numerical results have been carried out and good reconstruction has been obtained even in the presence of white Gaussian noise in experimental data.

REFERENCES

[1] D. Colton and R. Kress, *Inverse Acoustic and Electromagnetic Scattering Theory*, Springer-Verlag, New York, 1992.

[2] F. Yaman, S. Simçsek, "Neural network approach to determine nonsmooth one-dimensional profiles in inverse scattering theory," *Microwave and Optical Technology Letters,* vol. 49, no. 12, pp. 3158-3162, Dec. 2007.

[3] C. H. Sun, C. L. Liu, K. C. Chen, C. C. Chiu, C. L. Li, and C. C. Tasi, "Electromagnetic transverse electric wave inverse scattering of a partially immersed conductor by steady-state genetic algorithm," *Electromagnetics.* vol. 28, no. 6, pp. 389-400, Aug. 2008.

[4] M. Donelli, G. Franceschini, A. Martini, and A. Massa, "An integrated multiscaling strategy based on a particle swarm algorithm for inverse scattering problems," *IEEE Transactions on Geoscience and Remote Sensing,* vol. 44, no. 2, pp. 298-312, Feb. 2006.

[5] W. Chien, C. H. Sun, and C. C. Chiu, "Image reconstruction for a partially immersed imperfectly conducting cylinder by genetic algorithm," *International Journal of Imaging Systems and Technology,* vol. 19, pp. 299-305, Dec. 2009

[6] M. Moghaddam and W. C. Chew, "Study of some practical issues in inversion with the Born iterative method using time-domain data," *IEEE Transactions on Antennas and Propagation*, vol. 41, no. 2, pp. 177-184, Feb. 1993.

[7] W. H. Weedon, *Broadband microwave inverse scattering: Theory and experiment*, Ph.D. dissertation, University of Illinois at Urbana-Champaign, 1994.

[8] I. T. Rekanos, "Time-domain inverse scattering using Lagrange multipliers: an iterative FDTD-based optimization technique," *Journal of Electromagnetic Waves and Applications*, vol. 17, no. 2, pp. 271-289, 2003.

[9] T. Takenaka, H. Jia, and T. Tanaka, "Microwave imaging of electrical property distributions by a forward-backward time-stepping method," *Journal of Electromagnetic Waves Application*, vol. 14, pp. 1609–1625, 2000.

[10] X. M. Zhong, C Liao, and W. Chen, "Image reconstruction of arbitrary cross section conducting cylinder using UWB pulse," *Journal of Electromagnetic Waves Application,,* vol. 21, no. 1, pp. 25-34, 2007.

[11] C. H. Huang, C. C. Chiu, C. L. Li, and Y. H. Li, "Image reconstruction of the buried metallic cylinder using FDTD method and SSGA," *Progress In Electromagnetics Research*, vol. 85, pp. 195-210, 2008.

[12] K. A. Michalski, "Electromagnetic imaging of circular-cylindrical conductors and tunnels using a differential evolution algorithm," *Microwave and Optical Technology Letters*, vol. 27, no. 5, pp. 330–334, Dec. 2000

[13] A. Semnani, M. Kamyab, and I. T. Rekanos, "Reconstruction of one-dimensional dielectric scatterers using differential evolution and particle swarm optimization," *IEEE Geoscience and Remote Sensing Letters*, vol. 6, no. 4, pp. 671-675, Oct. 2009.

[14] I. T. Rekanos, "Shape reconstruction of a perfectly conducting scatterer using differential evolution and particle swarm optimization, " *IEEE Transactions on Geoscience and Remote Sensing*, vol. 46, no. 7, pp. 1967-1974, July 2008.

[15] M. Donelli and A. Massa, "Computational approach based on a particle swarm optimizer for microwave imaging of two-dimensional dielectric scatterers," *IEEE Transactions on Microwave Theory and Techniques*, vol. 53, no. 5, pp. 1761 - 1776, May. 2005.

[16] T. Huang and A. S. Mohan, "Application of particle swarm optimization for microwave imaging of lossy dielectric objects," *IEEE Antenna and Propagation Society International Symposium Digest*, pp. 852 – 855, 2005.

[17] C. H. Huang, C. C. Chiu, C. L. Li, and K. C. Chen, "Time domain inverse scattering of a two-dimensional homogenous dielectric object with arbitrary shape by particle swarm optimization," *Progress In Electromagnetic Research,* vol. 82, pp. 381-400, 2008.

[18] A. Taflove and S. Hagness, *Computational Electrodynamics: The Finite-Difference Time-Domain Method*, Artech House, Boston, MA, 2000.

[19] M. W. Chevalier, R. J. Luebbers, and V. P. Cable, "FDTD local grid with material traverse," *IEEE Trans. Antennas and Propagation,* vol. 45, no. 3, March 1997.

[20] C. L. Li, C.-W. Liu, and S. H. Chen, "Optimization of a PML absorber's conductivity profile using FDTD," *Microwave and Optical Technology Letters*, vol. 37, no. 5, pp. 69-73 , Jun. 2003

[21] C. de Boor, *A Practical Guide to Splines*, Springer-Verlag, New York, 1978.
[22] J. Kennedy and R. C. Eberhart, "Particle swarm optimization," *Proceedings of the IEEE International Conference on Neural Network*, pp. 1942-1948, 1995.
[23] M. Clerc, "The swarm and the queen: towards a deterministic and adaptive particle swarm optimization," *Proceedings of Congress on Evolutionary Computation*, Washington, DC, pp. 1951-1957, 1999.
[24] A. Carlisle and G. Dozier, "An Off-The-Shelf PSO," *Proceedings of the Workshop on Particle Swarm Optimization*, pp.1-6, 2001.
[25] T. Huang and A. S. Mohan, "A hybrid boundary condition for robust particle swarm. optimization," *IEEE Antennas and Wireless Propagation Letters*, vol. 4, pp.112-117, 2005.

Chung-Hsin Huang was born in Tucheng, Taiwan, Republic of China, on February 1, 1980. He received his M.S.E.E. and Ph.D. degrees in electrical engineering from Tamkang University, Taipei, Taiwan, in 2004 and 2009 respectively. He is currently an Assistant Professor with the Department of Computer and Communication Engineering, Taipei College of Maritime Technology. His current research interests include inverse scattering problem, optimization methods, dielectric material characterization, and wireless communications.

Chien-Hung Chen was born in Kaohsiung, Taiwan, Republic of China, on March 8, 1971. He received his M.S.E.E. and Ph.D. degrees in electrical engineering from Tamkang University, Taipei, Taiwan, in 1999 and 2006 respectively. He is currently an Assistant Professor with the Department of Computer and Communication Engineering, Taipei College of Maritime Technology. His current research interests include indoor wireless communications and numerical techniques in electromagnetics.

Chien-Ching Chiu was born in Taoyuan, Taiwan, Republic of China, on January 23, 1963. He received the B.S.C.E. degree from National Chiao Tung University, Hsinchu, Taiwan, in 1985 and his M.S.E.E. and Ph.D. degrees from National Taiwan University, Taipei, Taiwan, in 1987 and 1991 respectively. From 1987 to1989, he served in the ROC Army Force as a communication officer. In 1992, he joined the faculty of the Department of Electrical Engineering, Tamkang University, where he is now a Professor. He was a visiting scholar at the MIT and University of Illinois, Urbana from 1998 to 1999. His current research interests include microwave imaging, numerical techniques in electromagnetic, and indoor wireless communications.

Ching-Lieh Li was born November 24, 1963, in Pingtun, Taiwan. He received the B.S. degree from National Taiwan University, Taipei, Taiwan, in 1985, and the M.S. and Ph.D. degrees from Michigan State University, East Lansing, in 1990 and 1993, respectively, all in electrical engineering.

From 1989 to 1993, he was a Research Assistant in the Electrical Engineering Department, Michigan State University, where he worked on the measurement techniques for determining the electromagnetic properties of materials. In 1993, he joined the Electrical Engineering Faculty at Tamkang University, Taipei, Taiwan. Currently, his research activities involve inverse scattering problem, and microstrip antenna design and dielectric material characterization. His areas of special interest include theoretical and computational electromagnetics, and application of various optimization schemes such as SSGA, PSO, DDE, Taguchi method in electromagnetics.

Hybrid Electromagnetic and Non-Linear Modeling and Design of SIW Cavity-Backed Active Antennas

Francesco Giuppi [1], Apostolos Georgiadis [2], Maurizio Bozzi [1], Selva Via [2], Ana Collado [2], and Luca Perregrini [1]

[1] Department of Electronics,
University of Pavia, Pavia, 27100, ITALY
francesco.giuppi@unipv.it, maurizio.bozzi@unipv.it, luca.perregrini@unipv.it

[2] Department of Communication Subsystems
Centre Tecnològic de Telecomunicacions de Catalunya, Castelldefels, 08860, SPAIN
ageorgiadis@cttc.es, svia@cttc.es, acollado@cttc.es

Abstract ─ This paper presents the modeling and implementation of planar passive and active cavity-backed antennas in substrate integrated waveguide (SIW) technology. The cavity-backed topology helps suppressing the undesired surface-wave modes and may provide better phase noise performance in the antenna oscillator. The use of SIW technology allows for a compact and cost-effective implementation of the structure. The design of the active antenna involves both electromagnetic full-wave modeling for the radiating structure and nonlinear analysis of the active circuitry through harmonic balance and transient simulations. Single substrate prototypes of both passive and active antennas operating in X band are presented and measured, showing good agreement with simulated results.

Index Terms ─ Active antenna, cavity-backed antenna, harmonic-balance technique, substrate integrated waveguide (SIW).

I. INTRODUCTION

In the last years, a large number of wireless applications have emerged, spurring a great demand for low-profile antennas, for applications ranging from space communications to biomedical imaging and automotive radars. In this scenario, active integrated antennas represent a new paradigm for modern millimeter-wave systems, where compactness, light weight, low cost, low power consumption, and possibility to integrate multiple functions are required [1].

Substrate integrated waveguide (SIW) technology is the most promising candidate for the realization of low-profile active antennas, since it allows for the cost-effective and high performance implementation of waveguide-like structures using conventional fabrication techniques and permits their easy integration with planar circuitry and active devices [2–5]. A large number of SIW components have been proposed in the literature, including filters, couplers, power combiners and dividers, oscillators, and antennas [5]. Current research trends in SIW technology aim to the integration of complete systems on the same substrate, according to the system-on-substrate (SoS) approach [3, 4].

Among the different topologies for the implementation of low-profile active antennas, cavity-backed antennas appear to be a particularly suitable solution. Cavity-backed antennas have been widely studied in the literature [6–8], as they offer several design advantages such as increased efficiency due to surface-wave suppression, as well as adequate metal surface to dissipate heat from active devices required in large array implementations. Furthermore, cavity-backed antenna oscillators permit to improve phase noise performance [9].

This paper presents the design and the implementation of cavity-backed antennas in SIW technology. In particular, compact, single substrate cavity-backed passive and active antennas using a SIW cavity are presented. The paper is organized as follows: Sec. II presents the design and

experimental verification of a passive cavity-backed SIW antenna operating in X band. The modeling is performed by using a full-wave electromagnetic analysis tool, based on the finite element method (FEM). Sec. III presents the active counterpart of the cavity-backed SIW antenna. In this case, the modeling is based on the combined use of a full-wave FEM analysis and of non-linear analysis tools, based on the harmonic-balance (HB) technique and transient simulations. Conclusions are discussed in Sec. IV.

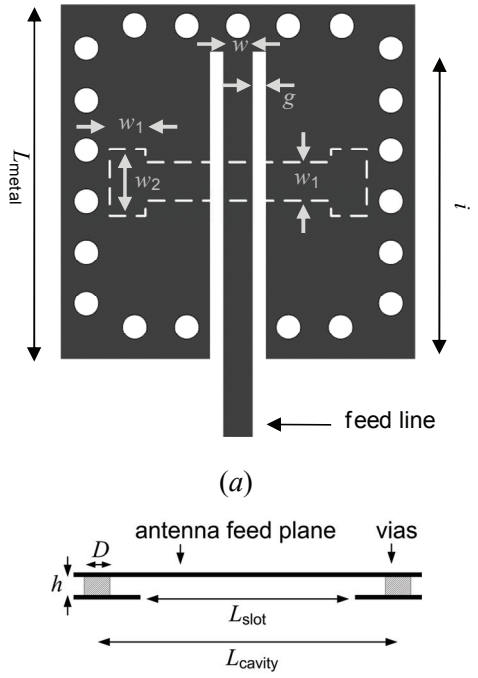

Fig. 1. Geometry of the passive SIW antenna: (*a*) front view; (*b*) side view.

II. PASSIVE SIW ANTENNA

The passive cavity-backed SIW antenna is presented in this Section. It comprises a slot antenna backed by a SIW cavity, excited by a coplanar line (Fig. 1). This topology follows the one presented in [7], where the SIW cavity is obtained by four rows of metal cylinders in a dielectric layer with dual metallization. The radiating element is a slot etched in the ground plane. An input grounded coplanar line is used to excite both the cavity mode and the slot. This antenna topology permits to isolate the feeding circuitry and the radiating slot, since they are located on opposite sides of the dielectric substrate (Fig. 1*b*).

Table 1. Geometrical dimensions of the passive cavity-backed SIW antenna.

parameter	*dimension* [mm]
D	1.00
L_{cavity}	11.80
L_{slot}	10.00
L_{metal}	13.80
i	12.00
w_1	1.40
w_2	2.60
o	0.20
w	1.16
g	0.50

With respect to the antenna proposed in [7], the major differences are the use of a smaller cavity and of a "dogbone" slot, which allows for a more compact structure. The "dogbone" shape of the slot has been used in order to obtain the desired length within the available cavity space (Fig. 1*a*).

A. Electromagnetic modeling

The design of this passive structure has been carried out with a FEM-based full-wave simulator (Ansoft HFSS).

The antenna was designed on Arlon 25N substrate, with thickness h=0.508 mm and relative dielectric permittivity of 3.38 at 10 GHz. The SIW cavity is included between two copper planes connected by metal vias with diameter D=1 mm and spacing 2 mm, in order to avoid lateral radiation leakage [5]. In particular, the slot and the cavity have been dimensioned for broadside radiation and optimal input matching at 10 GHz. The cavity size has been selected to resonate on the TM_{120} mode. The feed line is a 50 Ω microstrip line outside the SIW cavity, whereas it turns into a coplanar line inside the cavity.

Parametric analyses have been carried out in order to investigate the dependence of the frequency response of the structure on certain

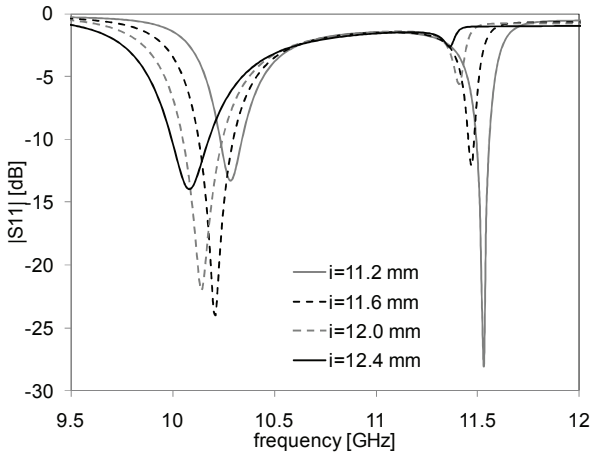

(*a*)

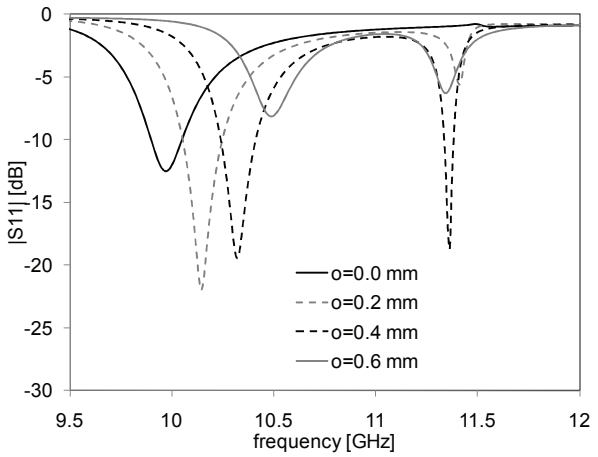

(*b*)

Fig. 2. Parametric study of the input matching of the passive SIW antenna.

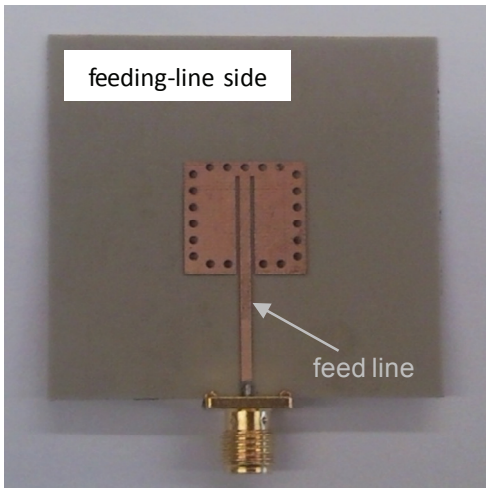

(*a*)

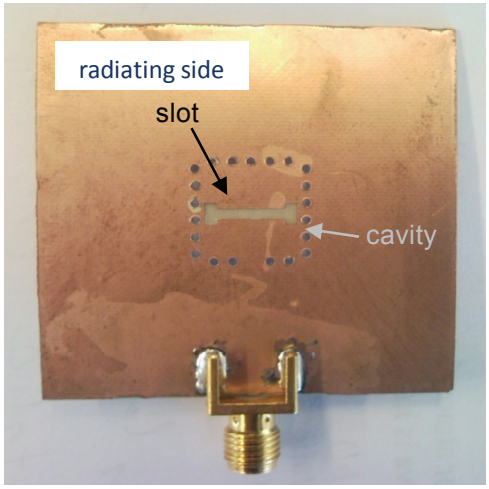

(*b*)

Fig. 3. Photographs of the passive SIW antenna prototype: (*a*) feeding-line side; (*b*) radiating side.

geometrical parameters. Figure 2 shows the effect of the length of the coplanar feed line *i* and of the offset of the slot *o* on the frequency response of the antenna. Both parameters strongly affect the input matching around the first resonance (10 GHz) as well as the presence of a second resonance at 11.5 GHz. The second resonance can be attributed to the half-wavelength resonance of the coplanar feed line. More specifically, Fig. 2*a* shows that increasing the length of the coplanar line permits to minimize the effect of the second resonance. Nevertheless, if the value of *i* is larger than 12 mm, the input matching around the first resonance degrades. Similarly, Fig. 2*b* permits to identify an optimal value for the offset of the slot: if *o*=0, there is a negligible effect of the second resonance but also a poor matching of the first resonance, whereas values of *o* larger than 0.2 mm lead to a strong effect of the second resonance.

On the basis of the parametric analysis shown in Fig. 2, the final dimensions of the geometrical parameters involved in the design have been selected and they are listed in Table 1.

B. Experimental results

A prototype of the passive cavity-backed SIW antenna has been fabricated and tested. Figure 3 shows photographs of the feed-line side and of the radiating side of the antenna.

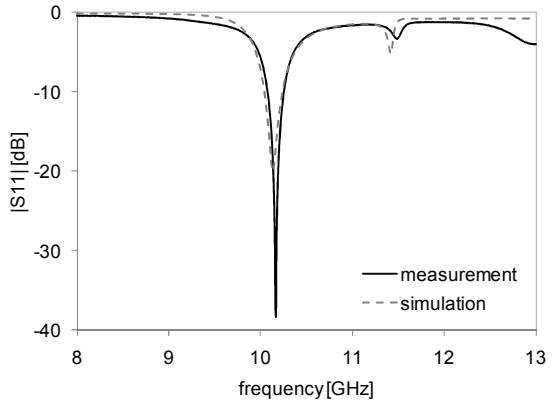

Fig. 4. Simulated and measured input matching of the passive SIW antenna.

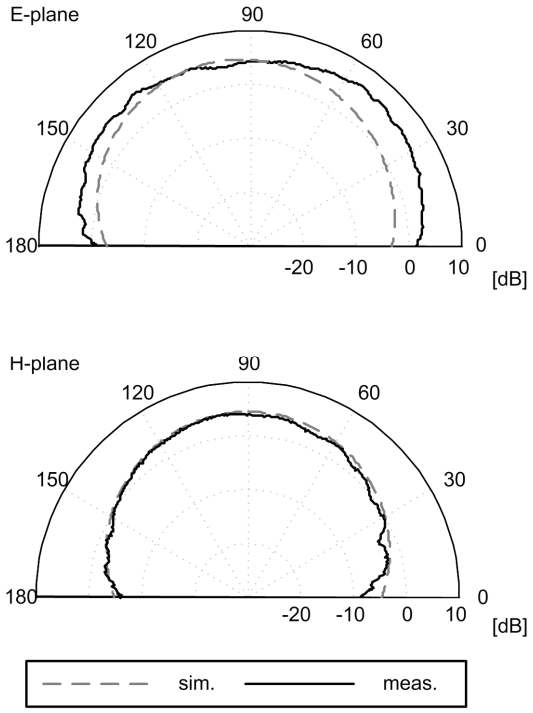

Fig. 5. Simulated and measured radiation pattern of the passive SIW antenna at the main resonance.

Figure 4 shows the simulated and measured input matching of the antenna, which exhibit a very good agreement over the entire frequency band. In particular, the simulation results predict a resonance at 10.14 GHz, whereas the measured results show a minimum of $|S_{11}|$ at 10.17 GHz.
The simulated and measured radiation patterns of the passive antenna are shown in Fig. 5, for both

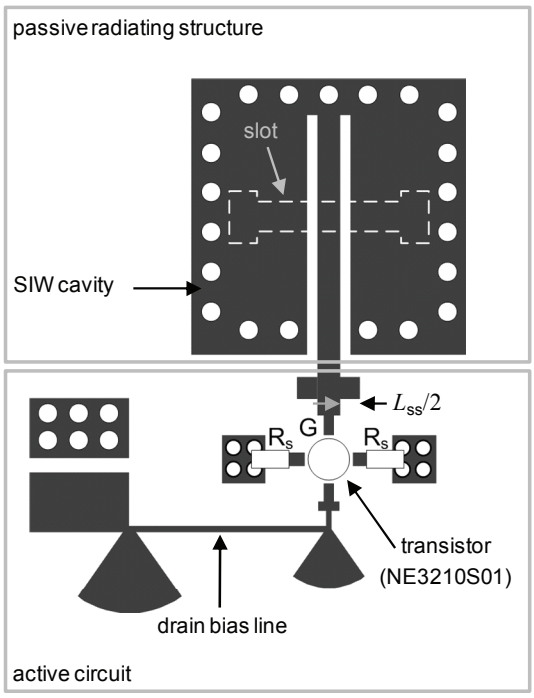

Fig. 6. Geometry of the active SIW antenna.

E-plane and H-plane cuts. The simulated gain of the final design was 4.2 dB at broadside, while the measured gain was 4.1 dB. The two patterns were obtained at the frequency of minimum reflection coefficient, namely 10.14 GHz for the simulated pattern and 10.17 GHz for the measured (Fig. 4). The asymmetry in the E-plane of the measured gain is potentially attributed to the feed line and connectors in the measurement setup.

III. ACTIVE SIW ANTENNA

The passive antenna discussed in the previous section has been used as the starting point for the design of an active cavity-backed SIW antenna. The active antenna consists of the combination of the passive antenna and a reflection oscillator, which uses the SIW cavity as the resonant element (Fig. 6). A similar cavity-backed slot antenna oscillator topology has been presented in [10]. In the present work, however, the cavity consists of a SIW resonator leading to a single substrate implementation of both the antenna and the cavity, and the slot is placed on a separate side from the active circuit, thus minimizing the effects of the active components and bias lines in the radiation pattern of the slot.

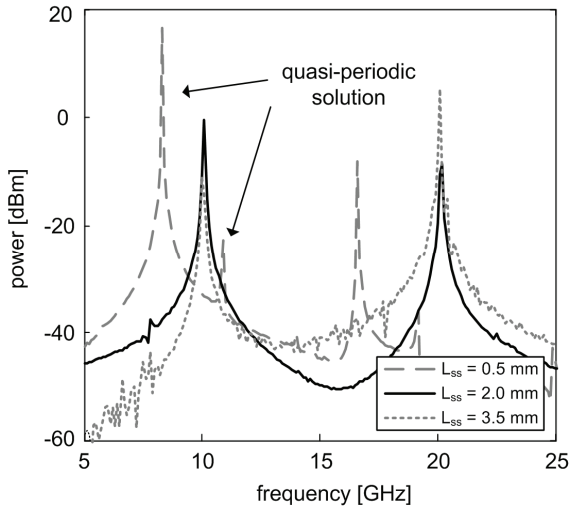

Fig. 7. Transient simulations of the active antenna, showing the effect of the stub length L_{ss}.

A. Electromagnetic and non-linear modeling

Once the design of the cavity-backed antenna has been completed, the oscillator circuit is designed using a commercial harmonic-balance simulator available from Agilent ADS. The S-parameters of the passive antenna obtained from the full-wave electromagnetic simulation are used in the HB analysis. The reflection oscillator is obtained by connecting the gate of an active pHEMT device (NE3210S01) to the cavity feed line (Fig. 6). Two 16 Ω resistors are then placed between the source terminals of the device and ground, in order to self-bias the circuit. The resulting structure is optimized to obtain an oscillation near the cavity resonance frequency of 10.14 GHz. In order to avoid the convergence to the trivial DC solution, the HB simulator was made to converge to the oscillating steady state using a properly defined ideal probe, as described in [11] and references therein. The probe consists of an ideal voltage source in series with an ideal band-pass filter. It is connected in parallel to a circuit node, in this case to the gate of the transistor. This auxiliary generator helps forcing the simulator to find an oscillating solution with non-zero amplitude at the desired frequency. Once the oscillating steady state solution has been obtained a transient simulation is used to study its stability.

One of the main parameters involved in the optimization of the active circuit is the stub length

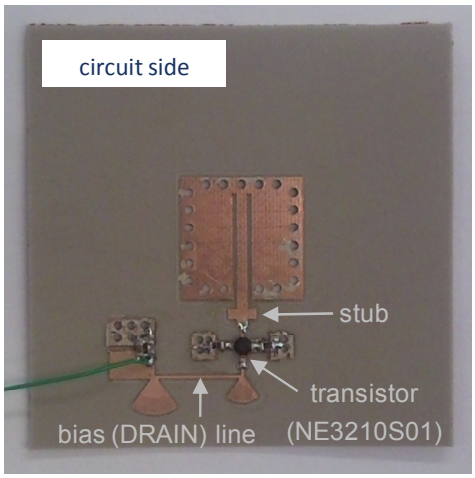

(*a*)

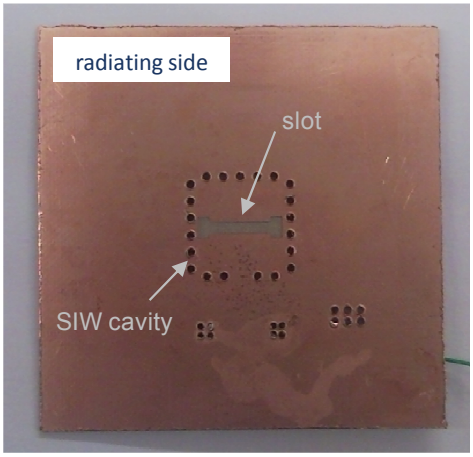

(*b*)

Fig. 8. Photographs of the active SIW antenna prototype: (*a*) circuit side; (*b*) radiating side.

L_{ss} (Fig. 6). Changing this length allows to modify the input impedance seen from the transistor looking into the cavity; it can be seen that this design parameter can be used to optimize the oscillation frequency and eliminate unwanted parasitic oscillations. As shown in Fig. 7, for L_{ss}=0.5 mm the oscillator exhibits a quasi-periodic behavior with two fundamental frequencies (namely, at 8.3 GHz and 10.9 GHz). As L_{ss} increases, it is possible to obtain the desired oscillation frequency near the cavity resonance. For L_{ss}=3.5 mm, though, the second harmonic content of the oscillation grows. The selected value of L_{ss}=2 mm allows to find a good trade-off between the harmonic purity and the desired oscillation frequency, corresponding to 10.1 GHz.

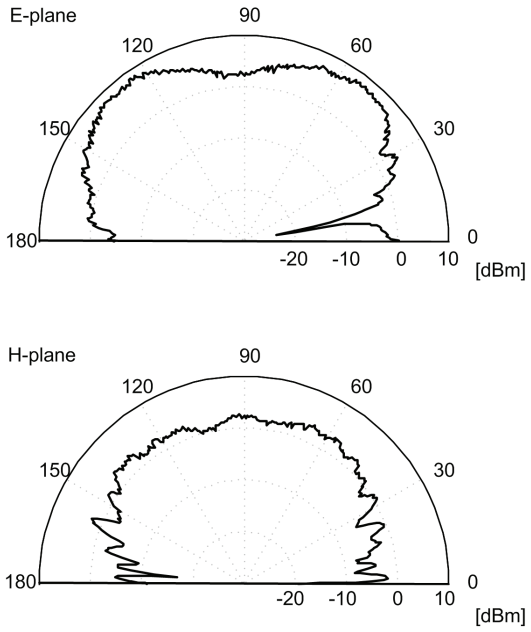

Fig. 9. Measured effective isotropic radiated power (EIRP) of the SIW active antenna.

B. Experimental results

The active cavity-backed SIW antenna was fabricated and experimentally characterized. Pictures of the prototype are shown in Fig. 8. The measured oscillation frequency of the active antenna was 9.8 GHz. Figure 9 shows the measured E-plane and H-plane radiation patterns of the active antenna, in the form of effective radiated power (i.e., gain and power product). The measured effective radiated power at broadside was 2.2 dBm.

The measured radiation pattern permits to estimate the overall radiated power, which is 0.65 mW. Since the power consumption from a DC power supply is 10.5 mW, the estimated DC-to-RF conversion efficiency results in 6.2 %.

Finally, using a probe to capture the radiated signal, the phase noise of the oscillator was measured to be -98 dBc/Hz at 1 MHz offset. The phase noise spectrum exhibited a 30 dB/dec slope up to and beyond 1 MHz offset indicating 1/*f* noise.

IV. CONCLUSION

A novel active SIW antenna has been designed and experimentally verified. It consists in the combination of a cavity-backed SIW slot antenna and a reflection oscillator, which shares the same SIW cavity with the antenna. This antenna results in a single-substrate, compact circuit topology, featuring the slot antenna and active circuitry on different sides of the substrate, thus allowing for high integration and low-cost fabrication methods.

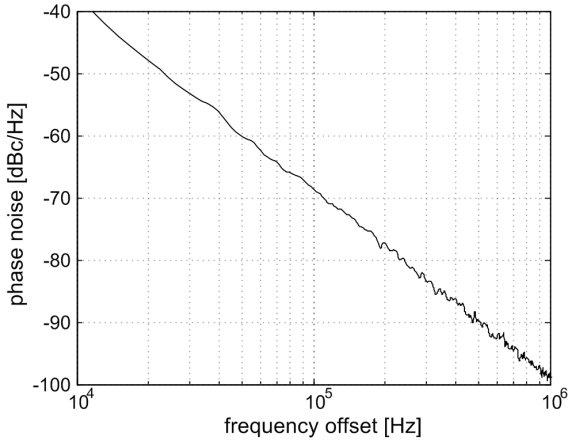

Fig. 10. Measured phase noise of the active antenna.

The combined use of full-wave electro-magnetic simulation tools and non-linear circuit analysis has been required for the design of this active antenna. More specifically, a full-wave FEM simulator has been adopted for the design of the antenna, whereas harmonic-balance and transient simulations have been used for the design of the oscillator.

X-band prototypes of both the passive SIW antenna and of the complete active antenna have been fabricated and measured, showing a good agreement with simulation data.

ACKNOWLEDGMENT

This work was carried out in the framework of COST Action IC0803, titled "RF/Microwave Communication Subsystems for Emerging Wireless Technologies". The work of A. Georgiadis, A. Collado and S. Via was also supported by the Spanish Ministry of Science and Innovation project TEC2008-02685/TEC, and grants PTQ-06-02-0555 and PTQ-08-01-06432. The work of F. Giuppi, M. Bozzi and L. Perregrini was also supported by the Italian Ministry of the University under project PRIN no. 2008HE84LJ.

REFERENCES

[1] Y. Qian and T. Itoh, "Progress in active integrated antennas and their applications," *IEEE Trans. Microwave Theory Tech.*, vol. 46, no. 11, pp. 1891-1900, Nov. 1998.

[2] D. Deslandes and K. Wu, "Single-substrate integration technique of planar circuits and waveguide filters," *IEEE Trans. Microwave Theory Tech.*, vol. 51, no. 2, pp. 593-596, Feb. 2003.

[3] K. K. Samanta, D. Stephens, and I. D. Robertson, "Design and performance of a 60-GHz multi-chip module receiver employing substrate integrated waveguides," *IET Microwave Antennas Propag.*, vol. 1, no. 5, pp. 961-967, Oct. 2007.

[4] Z. Li and K. Wu, "24-GHz frequency-modulation continuous-wave radar front-end System-on-Substrate," *IEEE Trans. Microwave Theory Tech.*, vol. 56, No. 2, pp. 278–285, Feb. 2008.

[5] M. Bozzi, L. Perregrini, K. Wu, and P. Arcioni, "Current and future research trends in substrate integrated waveguide Technology," *Radio-engineering*, vol. 18, no. 2, pp. 201-209, June 2009.

[6] J. -C. Cheng, N. I. Dib, and L. P. B. Katehi, "Theoretical modeling of cavity-backed patch antennas using a hybrid technique," *IEEE Trans. Antennas Propag.*, vol. 43, no. 9, pp. 1003-1013, Sept. 1995.

[7] Q. L. Guo, F. H. Zhi, X. D. Lin, and L. S. Ling, "Planar slot antenna backed by substrate integrated waveguide Cavity," *IEEE Antennas Wireless Propag. Lett.*, vol. 7, pp. 236-239, 2008.

[8] P. R. Haddad and D. M. Pozar, "Analysis of two aperture-coupled cavity-backed antennas," *IEEE Transactions on Antennas and Propagation*, vol. 45, no. 12, pp. 1717-1726, December 1997.

[9] M. Zheng, P. Gardener, P. S. Hall, Y. Hao, Q. Chen, and V. F. Fusco, "Cavity control of active integrated antenna oscillators," *IEE Proc. Microwaves, Antennas Propagation*, vol. 148, no. 1, pp. 15-20, Jan. 2001.

[10] H. P. Moyer, R. A. York, "Active cavity-backed slot antenna using MESFETs," *IEEE Microwave and Guided Wave Letters*, vol. 3, no. 4, pp. 95-97, Apr. 1993.

[11] A. Georgiadis and A. Collado, "Nonlinear analysis of a reflectarray cell based on a voltage-controlled oscillator," *IEEE Int. Symposium on Antennas and Propagation*, pp. 1-4, 5-11 July 2008.

Francesco Giuppi was born in Pavia, Italy, in 1983. He received the M.S. degree (*summa cum laude*) in Electronic Engineering from the University of Pavia, Italy, in 2008. In November 2008, he joined the Department of Electronics of the University of Pavia as a Ph.D. student in Microwave Electronics. His current research interests are related to the development of active and passive components in substrate integrated waveguide (SIW) technology.

He received the Best Student Paper Award at the European Conference on Antennas and Propagation (EuCAP 2010) and was awarded the second place at the Student Paper Competition at the Applied Computational Electromagnetics Society conference (ACES 2010).

Apostolos Georgiadis was born in Thessaloniki, Greece. He received the B.S. degree in physics and the M.S. degree in telecommunications from the Aristotle University of Thessaloniki, Greece, in 1993 and 1996, respectively. He received the Ph.D. degree in electrical engineering from the University of Massachusetts, Amherst, in 2002.

He is currently a senior research associate at Centre Tecnologic de Telecomunicacions de Catalunya (CTTC). He is the Chairman of COST Action IC0803, RF/Microwave communication subsystems for emerging wireless technologies (RFCSET). His research interests include nonlinear microwave circuit design and wireless systems, active antenna arrays and specifically coupled oscillator arrays.

Maurizio Bozzi was born in Voghera, Italy, in 1971. He received the "Laurea" degree in Electronic Engineering and the Ph.D. in Electronics and Computer Science from the University of Pavia, Italy, in 1996 and 2000, respectively. In 2002 he joined the Department of Electronics of the University of Pavia as an Assistant Professor in electro-magnetics. He currently teaches the courses of "Numerical Techniques for Electromagnetics" and of "Computational Electromagnetics and Photonics".

He held research positions in various universities worldwide, including the Technical University of Darmstadt, Germany, the University of Valencia, Spain, the Polytechnical University of Montreal, Canada, and the Centre Tecnologic de Telecomunicacions de Catalunya (CTTC), Spain. His research activities concern the development of numerical methods for the electromagnetic modeling of microwave and millimeter-wave components.

Prof. Bozzi received the Best Young Scientist Paper Award at the XXVII General Assembly of URSI in 2002, and the MECSA Prize for the best paper presented by a young researcher at the Italian Conference on Electromagnetics in 2000.

Selva Vía Labrada was born in Santander, Spain. She received the B.S. in Telecommunications Engineering from the University of Cantabria in 2006. From September 2005 to July 2006, she did a placement like student in the Electronic Communications department at ENSEA, France, where she carried out the development of a low noise amplifier, and the optimization of a passive circuit, the last for Thalès Communications, France. From October 2006 to May 2007, she worked as an engineer trainee for ELA Medical, France, in the Advanced Research service, where she studied the compatibility of transceivers for RF telemetry in pacemakers. Since 2007, she works as a Microwave Engineer in CTTC in the area of Communications Subsystems.

Ana Collado was born in Santander, Spain. She received a degree in Telecommunications Engineering and the Ph.D. from the University of Cantabria, Santander, Spain, in 2002 and 2007, respectively.

In 2002, she worked at the University of the Basque Country, Bilbao, studying the uncertainty in the noise figure measurements in MMIC low noise amplifiers. Since July 2007, she is working in the Centre Tecnologic de Telecommunications de Catalunya (CTTC) as a research associate in the area of Communications Subsystems. Her areas of interest include the development of techniques for practical bifurcation control, the investigation of coupled-oscillator systems and stability analysis of power amplifiers.

Luca Perregrini was born in Sondrio, Italy, in 1964. He received the "Laurea" degree in Electronic Engineering and the Ph.D. in Electronics and Computer Science from the University of Pavia, Pavia, Italy, in 1989 and 1993, respectively. In 1992, he joined the Department of Electronics of the University of Pavia, where he is now an Associate Professor in electromagnetics.

His main research interests are in numerical methods for the analysis and optimization of waveguide circuits, frequency selective surfaces, reflectarrays, and printed microwave circuits. He co-authored the textbook Fondamenti di Onde Elettromagnetiche, McGraw-Hill Italia, 2003.

Prof. Perregrini was an Invited Professor at the Polytechnical University of Montreal, Montreal, Quebec, Canada in 2001, 2002, and 2004. He was a consultant to the European Space Agency and to some European telecommunication companies.

A Simple Technique for Propagation Characteristics of Substrate Integrated Waveguide

Esfandiar Mehrshahi and Mehdi Salehi

Department of Electrical and Computer Engineering
Shahid Beheshti University, G. C., Tehran, Iran
mehr@cc.sbu.ac.ir, m_salehi@sbu.ac.ir

Abstract ─ A simple technique is presented for propagation characteristics of substrate integrated waveguide (SIW). A unit cell of the periodic structure is divided into consecutive rectangular waveguide sections with small difference in widths. Each section is modeled by a transfer matrix which is calculated by satisfying the boundary conditions on discontinuities. Propagation constant of the SIW is extracted by applying the Floquet theorem to the overall transfer matrix of a single unit cell. The results of this extremely simple method agree well with measured values and other numerical techniques reported in recent literatures.

Index Terms ─ Dispersion characteristic, periodic structure, substrate integrated waveguide (SIW), transfer matrix, waveguide discontinuity.

I. INTRODUCTION

To a great extent, systems are based on planar structures which often exhibit high losses. On the other hand, non-planar metallic waveguides are low-loss structures with high power handling capability. The substrate integrated waveguide (SIW) is a periodic structure which preserves well-known advantages of both conventional rectangular waveguide and microstrip transmission line. Hence, SIW is a promising structure for microwave planar circuits such as filters, resonators, mixers, and antennas [1-4]. Various analytical and numerical techniques, namely, the finite-difference frequency-domain (FDFD), the method of lines (MoL), and the boundary integral-resonant mode expansion (BI-RME) method have been employed to analyze SIW structures [5-7]. However, most of them are time and memory consuming and rarely give physical insight about the performance of the structure. Also, risk of divergence solutions may exist; these methods can be very accurate and efficient.

Based on the above observations, this raises the motivation in devising an efficient method to meet the challenges for accuracy, simulation time, required memory, and complexity. In this paper, a very simple approach is proposed to approximately calculate SIW characteristics. The reported results indicate that the electromagnetic field intensity radiated out of two rows of holes is negligible under condition of $\frac{S}{d} \le \frac{5}{2}$ [8] where S and d are longitudinal spacing and diameter of metal vias in the SIW structure, respectively. Hence, the area between adjacent via holes can be modeled by the electric wall. This concept allows for approximating the structure by consecutive rectangular waveguide sections with slightly different widths. By applying the Floquet theorem to overall transfer matrix of a single unit cell, the dispersion properties of the structure are obtained.

The paper is organized as follows. In section II, the overall transfer matrix of a single unit cell is calculated by approximating the configuration with consecutive waveguide steps. Simulation results compared with numerical and experimental values are presented in section III. Finally, section IV concludes the paper.

II. DESCRIPTION OF THE METHOD

The geometry of the SIW structure with its physical parameters is shown in Fig. 1. A period of the structure, indicated in Fig. 2(a), can be approximated by cascading of rectangular waveguide sections with slightly different widths. It is well-known that the selected unit cell is not the unique choice and another periodic structure can be obtained by shifting the configuration to the

left/right by a distance of, for example, *S/2*. On the other hand, the starting point of the unit cell doesn't affect the final results.

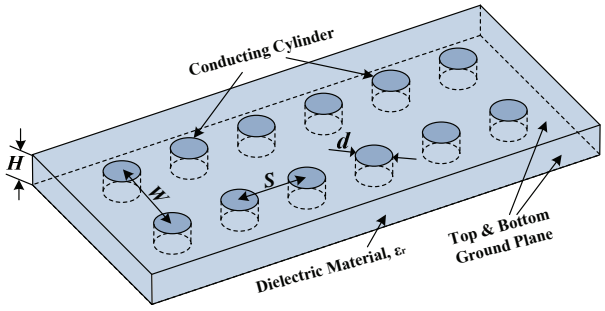

Fig. 1. 3D view of the SIW.

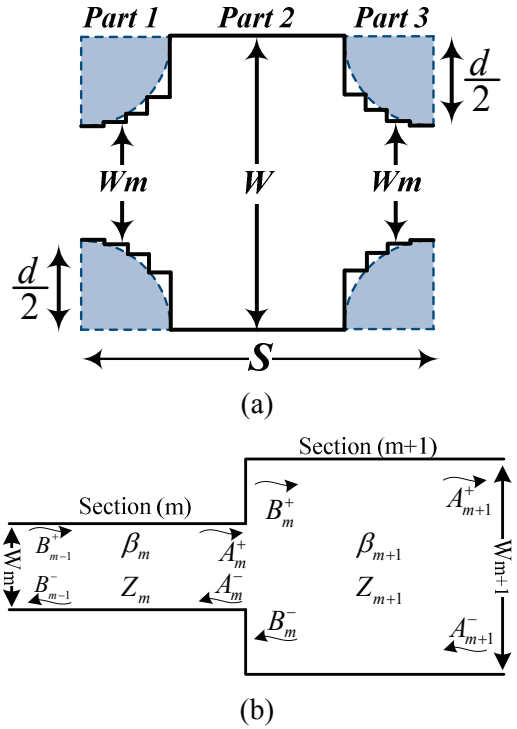

Fig. 2. Top view of the SIW structure: (a) a single unit cell and (b) m^{th} discontinuity.

The unit cell of the whole SIW, as shown in Fig. 2(a), is composed of three parts. The first one consists of the quarters of two lateral cylinders that are divided into *N* consecutive waveguide sections. Each of these sections have constant length of $\frac{d}{2N}$, increasing width of W_m (for *m=1,...N*), and constant height of *H* which are denoted as section *1* to *N*. Due to the fact that pointing power toward the gaps between metal vias is rapidly evanesced, the open area out of two via holes is well approximated by using electric walls that have the shortest length and longest width. As a result, the second part includes a waveguide with length of *(S-d)*, width of $W_{N+1}=W$, and the same height. Finally, the third part consists of the quarters of two next lateral cylinders that are divided into *N* sections just the same as the first one. The discontinuity between m^{th} and $(m+1)^{th}$ sections of the first part is illustrated in Fig. 2(b). As it shows, in the left-hand side of the discontinuity, fields can be written as a summation of forward and backward TE_{10} waves for $m = 1, 2, ..., N$ as follows

$$\begin{cases} E_m^{Left} = A_m^+ cos(\frac{\pi x}{W_m}) e^{+j\beta_m z} + A_m^- cos(\frac{\pi x}{W_m}) e^{-j\beta_m z} \\ H_m^{Left} = -\frac{A_m^+}{Z_m} cos(\frac{\pi x}{W_m}) e^{+j\beta_m z} + \frac{A_m^-}{Z_m} cos(\frac{\pi x}{W_m}) e^{-j\beta_m z} \end{cases}, \quad (1)$$

and similarly in the right-hand side as

$$\begin{cases} E_m^{Right} = B_m^+ cos(\frac{\pi x}{W_{m+1}}) e^{+j\beta_{m+1} z} + B_m^- cos(\frac{\pi x}{W_{m+1}}) e^{-j\beta_{m+1} z} \\ H_m^{Right} = -\frac{B_m^+}{Z_{m+1}} cos(\frac{\pi x}{W_{m+1}}) e^{+j\beta_{m+1} z} + \frac{B_m^-}{Z_{m+1}} cos(\frac{\pi x}{W_{m+1}}) e^{-j\beta_{m+1} z} \end{cases}, \quad (2)$$

where

$$\beta_m = \sqrt{\omega^2 \mu\varepsilon - (\frac{\pi}{W_m})^2}$$

$$Z_m = \frac{\omega\mu}{\beta_m}$$

$$W_m = \begin{cases} W - d\sqrt{1-(\frac{m-1}{N})^2} & m = 1, 2, ..., N \\ W & m = N+1 \end{cases}.$$

Neglecting all loss mechanisms, by applying the boundary conditions to the electric and magnetic fields in (1) and (2), the transfer matrix of each discontinuity in the first part for $m = 1, 2, ..., N$ can be extracted as follows

$$\begin{bmatrix} B_m^+ \\ B_m^- \end{bmatrix} = \frac{Z_{m+1} W_m}{4\kappa_m} \cdot \begin{bmatrix} \frac{\lambda_m}{Z_{m+1}} + \frac{1}{Z_m} & \frac{\lambda_m}{Z_{m+1}} - \frac{1}{Z_m} \\ \frac{\lambda_m}{Z_{m+1}} - \frac{1}{Z_m} & \frac{\lambda_m}{Z_{m+1}} + \frac{1}{Z_m} \end{bmatrix} \begin{bmatrix} A_m^+ \\ A_m^- \end{bmatrix}, \quad (3)$$

where

$$\lambda_m = \frac{W_m W_{m+1}}{4\kappa_m^2}$$

$$\kappa_m = \frac{2}{\pi} \frac{W_m}{\left(1-(\frac{W_m}{W_{m+1}})^2\right)} cos(\frac{\pi}{2} \frac{W_m}{W_{m+1}}).$$

It is worth mentioning that the value of λ_m tends to 1 by increasing the number of sections and hence,

simplify transfer matrices. Similarly, the transfer matrix of each discontinuity in the third part for $m = 1, 2, ..., N$ can be extracted as follows

$$\begin{bmatrix} B_m^+ \\ B_m^- \end{bmatrix} = \frac{Z_m K_m}{W_m} \begin{bmatrix} \frac{1}{\lambda_m Z_m} + \frac{1}{Z_{m+1}} & \frac{1}{\lambda_m Z_m} - \frac{1}{Z_{m+1}} \\ \frac{1}{\lambda_m Z_m} - \frac{1}{Z_{m+1}} & \frac{1}{\lambda_m Z_m} + \frac{1}{Z_{m+1}} \end{bmatrix} \begin{bmatrix} A_m^+ \\ A_m^- \end{bmatrix}. \quad (4)$$

Delay matrix between each consecutive discontinuity in the first and third parts can be expressed as following transfer matrixes, respectively.

$$\begin{bmatrix} A_m^+ \\ A_m^- \end{bmatrix} = \begin{bmatrix} e^{-j\beta_m \frac{d}{2N}} & 0 \\ 0 & e^{+j\beta_m \frac{d}{2N}} \end{bmatrix} \begin{bmatrix} B_{(m-1)}^+ \\ B_{(m-1)}^- \end{bmatrix}, \quad (5)$$

$$\begin{bmatrix} A_{(m-1)}^+ \\ A_{(m-1)}^- \end{bmatrix} = \begin{bmatrix} e^{-j\beta_m \frac{d}{2N}} & 0 \\ 0 & e^{+j\beta_m \frac{d}{2N}} \end{bmatrix} \begin{bmatrix} B_m^+ \\ B_m^- \end{bmatrix}. \quad (6)$$

Delay matrix of the second part ($\boldsymbol{T}_{P2}$) is given by

$$\begin{bmatrix} A_N^+ \\ A_N^- \end{bmatrix} = \underbrace{\begin{bmatrix} e^{-j\beta_N (S-d)} & 0 \\ 0 & e^{+j\beta_N (S-d)} \end{bmatrix}}_{\boldsymbol{T}_{P2}} \begin{bmatrix} B_N^+ \\ B_N^- \end{bmatrix}. \quad (7)$$

At last, the overall transfer matrix of the single unit cell, using the matrices of (3), (4), (5), (6), and (7) can be written as

$$\boldsymbol{T} = \boldsymbol{T}_{P3} \boldsymbol{T}_{P2} \boldsymbol{T}_{P1}, \quad (8)$$

where $\boldsymbol{T}_{Pi}$ ($i=1,2,3$) indicates transfer matrix of the i^{th} part as given by (7) and (9).

Taking the periodicity of the structure into account, we can employ the advantage of Floquet theorem. As a result of the theorem and according to (8), propagation constant of the SIW is written as below:

$$\cosh(j\beta S) = \frac{T_{11} + T_{22}}{2},$$

where β and S are propagation constant and period length of the SIW structure, respectively.

III. SIMULATION RESULTS

The empirical equations for equivalent width of the SIW are proposed for sufficiently small S in [8-10], respectively, as follows

$$W_{eff} = W - \frac{d^2}{0.95S}, \quad (10)$$

$$W_{eff} = W - 1.08\frac{d^2}{S} + 0.1\frac{d^2}{W}, \quad (11)$$

$$W = \frac{2W_{eff}}{\pi} \cot^{-1}\left(\frac{\pi S}{4W_{eff}} Ln\left(\frac{S}{2d}\right) \right). \quad (12)$$

It is shown, in the following, that the presented technique provides good agreement with recently theoretical and experimental data, as well as equivalent width formulas in a wide range of frequency and dimension parameters.

Selecting the number of sections N, is of importance for evaluating the performance of the employed method. By choosing $N=1$, the considered unit cell is simplified to three cascaded rectangular waveguides with width of $(W-d)$, W, and $(W-d)$, and hence, maximum available cut off frequency of the SIW structure is achieved compared to other values of N. In order to confirm convergence of the method, dispersion characteristic, as a function of the number of steps, is shown in Fig. 3. By increasing the number of steps, more accuracy is obtained and results are converged. However, due to the proposed model (lateral-wall approximation) and neglecting high-order mode effects, the cut off frequency slightly deviates from trusted values in [8]. On the other hand, large value of N leads to small-width discontinuities and hence, more accurate model is achieved for via holes at the cost of a small error. Based on the results, in the following examples, we consider $N=100$, which is sufficient to achieve a more accurate model for via holes and, hence, suitable accuracy.

As the first case, consider an SIW with the geometry parameters of $W=7.2$ mm, $d=0.8$ mm $S=2$ mm, and the relative permittivity $\varepsilon_r=2.33$. The

$$\boldsymbol{T}_{P1} = \left(\frac{Z_N W_{N-1}}{4K_{N-1}}\right) \begin{bmatrix} \left(\frac{\lambda_{N-1}}{Z_N} + \frac{1}{Z_{N-1}}\right) e^{-j\beta_{N-1}\frac{d}{2N}} & \left(\frac{\lambda_{N-1}}{Z_N} - \frac{1}{Z_{N-1}}\right) e^{+j\beta_{N-1}\frac{d}{2N}} \\ \left(\frac{\lambda_{N-1}}{Z_N} - \frac{1}{Z_{N-1}}\right) e^{-j\beta_{N-1}\frac{d}{2N}} & \left(\frac{\lambda_{N-1}}{Z_N} + \frac{1}{Z_{N-1}}\right) e^{+j\beta_{N-1}\frac{d}{2N}} \end{bmatrix} \ldots \left(\frac{Z_2 W_1}{4K_1}\right) \begin{bmatrix} \left(\frac{\lambda_1}{Z_2} + \frac{1}{Z_1}\right) e^{-j\beta_1\frac{d}{2N}} & \left(\frac{\lambda_1}{Z_2} - \frac{1}{Z_1}\right) e^{+j\beta_1\frac{d}{2N}} \\ \left(\frac{\lambda_1}{Z_2} - \frac{1}{Z_1}\right) e^{-j\beta_1\frac{d}{2N}} & \left(\frac{\lambda_1}{Z_2} + \frac{1}{Z_1}\right) e^{+j\beta_1\frac{d}{2N}} \end{bmatrix}$$

$$\boldsymbol{T}_{P3} = \left(\frac{Z_1 K_1}{W_1}\right) \begin{bmatrix} \left(\frac{1}{\lambda_1 Z_1} + \frac{1}{Z_2}\right) e^{-j\beta_1\frac{d}{2N}} & \left(\frac{1}{\lambda_1 Z_1} - \frac{1}{Z_2}\right) e^{-j\beta_1\frac{d}{2N}} \\ \left(\frac{1}{\lambda_1 Z_1} - \frac{1}{Z_2}\right) e^{+j\beta_1\frac{d}{2N}} & \left(\frac{1}{\lambda_1 Z_1} + \frac{1}{Z_2}\right) e^{+j\beta_1\frac{d}{2N}} \end{bmatrix} \ldots \left(\frac{Z_{N-1} K_{N-1}}{W_{N-1}}\right) \begin{bmatrix} \left(\frac{1}{\lambda_{N-1} Z_{N-1}} + \frac{1}{Z_N}\right) e^{-j\beta_{N-1}\frac{d}{2N}} & \left(\frac{1}{\lambda_{N-1} Z_{N-1}} - \frac{1}{Z_N}\right) e^{-j\beta_{N-1}\frac{d}{2N}} \\ \left(\frac{1}{\lambda_{N-1} Z_{N-1}} - \frac{1}{Z_N}\right) e^{+j\beta_{N-1}\frac{d}{2N}} & \left(\frac{1}{\lambda_{N-1} Z_{N-1}} + \frac{1}{Z_N}\right) e^{+j\beta_{N-1}\frac{d}{2N}} \end{bmatrix}. \quad (9)$$

propagation constant as a function of frequency compared with that of rectangular waveguide whose equivalent width is calculated from (10), (11), and (12) is illustrated in Fig. 4. The comparison verifies the accuracy of the proposed method. The propagation constant calculated by empirical equation in (10) and (11) is very close to experimental measurements in [8]. Hence, the cut off frequency of our method agrees well with the results of [8, 9].

The second example refers to a substrate integrated waveguide presented in [7, 11]. Its dimensions are as follows: *W=3.97 mm, d=0.635 mm, S=1.016 mm,* and $\varepsilon_r=9.9$. Results of the propagation constant are illustrated in Fig. 5. Our simulation result is well agreed with the calculated data of [7, 11] which are compared with the measurement values reported in [11].

The cut off characteristics are of importance for evaluating the performance of the SIW. For comparison, the same parameters of [9, 10] are chosen to calculate the cut off frequencies of TE_{10} mode with respect to the cylinder diameter and cylinder spacing of metallized holes as demonstrated in Fig. 6. Our simulation results show a very good agreement with those of [8]. Also, by increasing the cylinder diameter (or by decreasing the cylinder separation) the proposed method agrees well with the results of [8, 9]. Moreover, we compare our results, shown in Fig. 6, with those of [10]. However, the cut off frequency that is calculated from analytical formula of (12) is far from the others especially at small value of lateral spacing, *W*.

In this method, we express the single mode technique to improve simplicity of the analysis. In SIW structures only TE_{n0} modes (with odd value of *n*) can be excited and extracted, due to evanescent of the surface current on lateral walls and nature of the structure [8]. Therefore, single mode analysis is possible to nearly describe the propagation constant of the fundamental SIW mode. However, more accurate results can be achieved by considering high-order mode effects at the cost of complexity, computer memory and simulation time.

In spite of the variety of methods used to characterize the propagation characteristics in SIWs, high frequency structure simulator (HFSS) software, mainly relies on the finite-element (FE) method, is one of the most accurate methods for

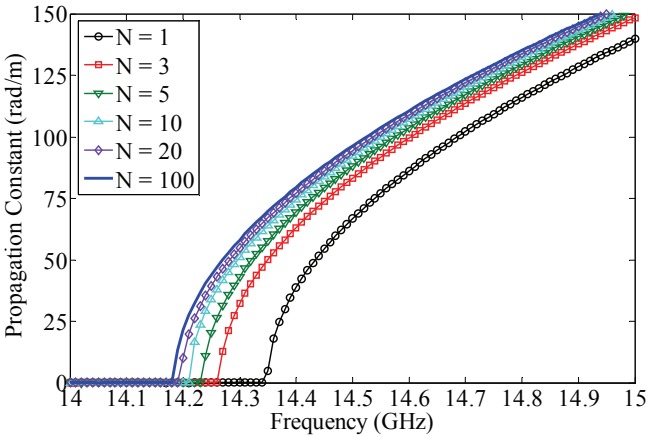

Fig. 3. Propagation constant of TE_{10} mode as a function of number of steps, *N*.

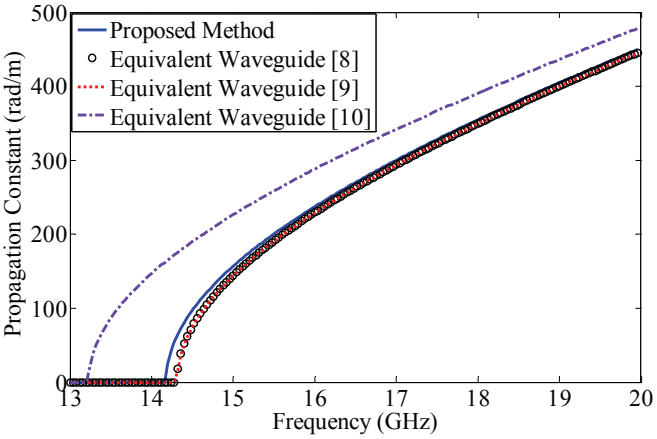

Fig. 4. Comparison of TE_{10} mode propagation constant between the proposed method and the closed-form formulas in [8-10].

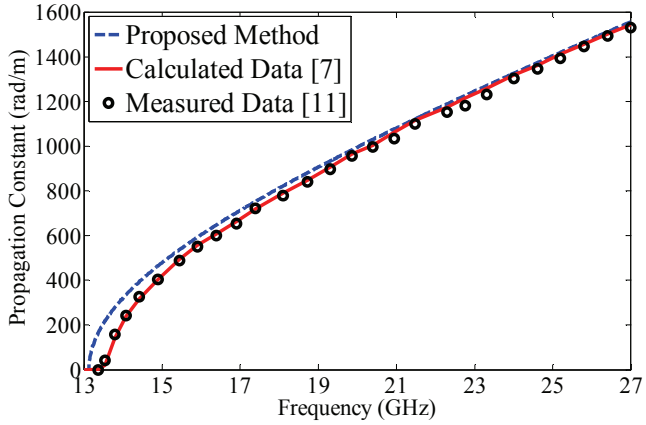

Fig. 5. Comparison of TE_{10} mode propagation constant between the proposed method and calculated results and measured data in [7, 11].

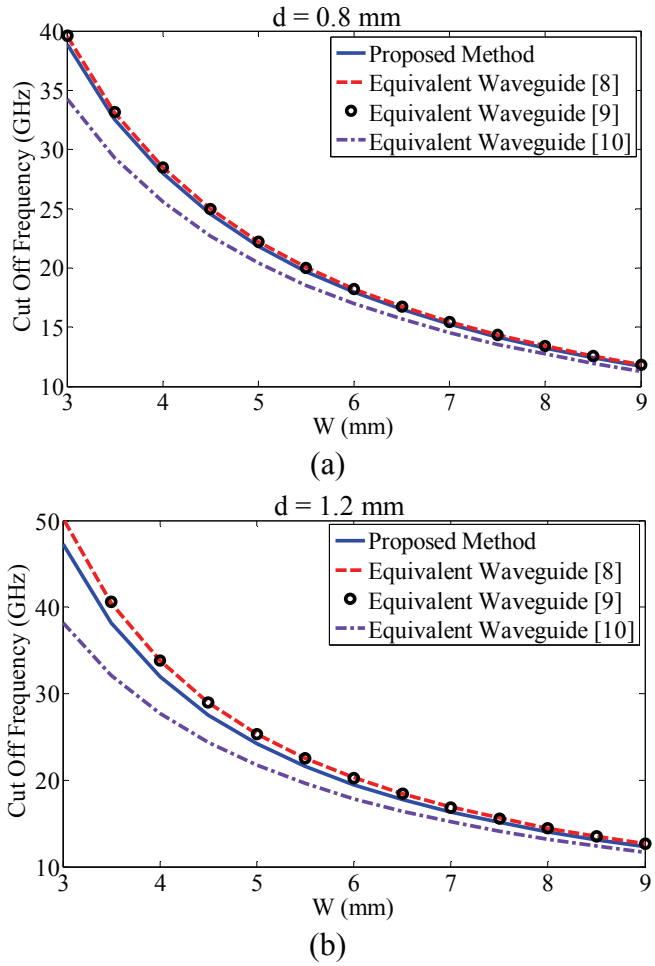

Fig. 6. Cut off frequency of TE_{10} mode with $S=1.5$ *mm* and $\varepsilon_r=2.2$ versus cylinder spacing of W and diameter of (a) $d=0.8$ *mm* and (b) $d=1.2$ *mm*.

analysis of electromagnetic problems. Hence, to demonstrate computational efficiency of the method, we make use of HFSS to solve the same problem for the comparison of the execution time, required memory, and accuracy. A single unit cell with single-mode excitation is used in HFSS to achieve propagation behavior of the SIW. Software, frequency steps, and frequency range are the same in both HFSS and proposed method. The simulation results of our method for two different numbers of sections are compared with those of HFSS and depicted in Table 1. According to the results, the typical computation time and memory requirement in the proposed technique is much less than HFSS results at the maximum cost of 0.7% error in cut off frequency.

Table 1: Execution time and required memory obtained from the proposed method and HFSS.

Methods	Time (s)	Memory (Mb)
Proposed method (N=10)	1.9	0.7
Proposed method (N=100)	5.3	4.9
HFSS + Floquet Theorem	67.1	63.1

IV. CONCLUSION

In this work, by ignoring high-order mode effects, an accurate and fast method with low memory requirements for analyzing SIW structures has been presented. The overall transfer matrix of the segmented structure is well calculated by satisfying the boundary conditions. Then, the propagation constant is calculated by applying the Floquet theorem. The significant advantage of the employed method in comparison with other numerical methods is its simplicity in computer implementation, let alone the accuracy of results. The execution time and required memory for this technique are much less than those of Ansoft's HFSS at the maximum cost of 0.7% error. The cut off frequency of TE_{10} mode with respect to the cylinder diameter d, and cylinder spacing W, is investigated to confirm accuracy of the method in a wide range of dimension parameters. The simulation results show a very good agreement with the results obtained from other numerical methods and experimental measurements over a wide frequency range.

ACKNOWLEDGMENT

The authors would like to thank Mr. Reza Rezaiesarlak for his generous cooperation in preparing the paper.

REFERENCES

[1] E. Mehrshahi, M. Salehi, and R. Rezaeisarlak, "Substrate integrated waveguide filters with stopband performance improvement," *International Conference on Microwave and Millimeter Wave Technology (ICMMT),* pp. 2018-2020, 2010.

[2] G. Angiulli, E. Arnieri, D. De Carlo *et al.*, "Fast nonlinear eigenvalues analysis of arbitrarily shaped substrate integrated waveguide (SIW) resonators," *IEEE*

Transactions on Magnetics, vol. 45, no. 3, pp. 1412-1415, 2009.

[3] C. Ji-Xin, H. Wei, H. Zhang-Cheng *et al.*, "Development of a low cost microwave mixer using a broad-band substrate integrated waveguide (SIW) coupler," *Microwave and Wireless Components Letters, IEEE,* vol. 16, no. 2, pp. 84-86, 2006.

[4] L. Bing, H. Wei, K. Zhenqi *et al.*, "Substrate integrated waveguide (SIW) monopulse slot antenna array," *IEEE Transactions on Antennas and Propagation,* vol. 57, no. 1, pp. 275-279, 2009.

[5] X. Feng, Z. Yulin, H. Wei *et al.*, "Finite-difference frequency-domain algorithm for modeling guided-wave properties of substrate integrated waveguide," *IEEE Transactions on Microwave Theory and Techniques,* vol. 51, no. 11, pp. 2221-2227, 2003.

[6] L. Yan, W. Hong, K. Wu *et al.*, "Investigations on the propagation characteristics of the substrate integrated waveguide based on the method of lines," *Microwaves, Antennas and Propagation, IEE Proceedings,* vol. 152, no. 1, pp. 35-42, 2005.

[7] M. Bozzi, L. Perregrini, and W. Ke, "Modeling of conductor, dielectric, and radiation losses in substrate integrated waveguide by the boundary integral-resonant mode expansion method," *Microwave Theory and Techniques, IEEE Transactions on,* vol. 56, no. 12, pp. 3153-3161, 2008.

[8] X. Feng and W. Ke, "Guided-wave and leakage characteristics of substrate integrated waveguide," *IEEE Transactions on Microwave Theory and Techniques,* vol. 53, no. 1, pp. 66-73, 2005.

[9] Y. Cassivi, L. Perregrini, P. Arcioni *et al.*, "Dispersion characteristics of substrate integrated rectangular waveguide," *Microwave and Wireless Components Letters, IEEE,* vol. 12, no. 9, pp. 333-335, 2002.

[10] W. Che, K. Deng, D. Wang *et al.*, "Analytical equivalence between substrate-integrated waveguide and rectangular waveguide," *Microwaves, Antennas & Propagation, IET,* vol. 2, no. 1, pp. 35-41, 2008.

[11] D. Deslandes and W. Ke, "Accurate modeling, wave mechanisms, and design considerations of a substrate integrated waveguide," *IEEE Transactions on Microwave Theory and Techniques,* vol. 54, no. 6, pp. 2516-2526, 2006.

Esfandiar Mehrshahi was born in Tehran, Iran, in 1963. He received the B.Sc. degree from the Iran University of Science and Technology, Tehran, Iran, in 1987, and the M.Sc. and Ph.D. degrees from the Sharif University of Technology, Tehran, Iran, in 1991 and 1998, respectively, all in electrical engineering. Since 1990, he has been involved in several research and engineering projects at the Iran Telecommunications Research Center (ITRC). He is currently an Assistant Professor at Shahid Beheshti University, Tehran, Iran. His main areas of interest are the nonlinear simulation of microwave circuits and low phase noise oscillators.

Mehdi Salehi was born in Isfahan, Iran, in 1979. He received the B.Sc. and M.Sc. degrees both in electrical engineering from Isfahan University of Technology (IUT), Isfahan, Iran, in 2001 and 2006, respectively. He is currently working toward his Ph.D. degree in electrical engineering at Shahid Beheshti University (SBU), Tehran, Iran. He worked as a researcher in Information and Communication Technology Institute (ICTI) on RF circuit design from 2001 to 2003. His current research interests include numerical methods in electromagnetic and advanced microwave and millimeter-wave circuits and components.

Positive-Negative-Positive Metamaterial Consisting of Ferrimagnetic Host and Wire Array

Yongjun Huang[1], Guangjun Wen[1], Tianqian Li[1], and Kang Xie[2]

[1] School of Communication and Information Engineering
University of Electronic Science and Technology of China, Chengdu, 611731, China
yjhuangllp@live.cn, wgj@uestc.edu.cn

[2] School of Opto-Electronic Information
University of Electronic Science and Technology of China, Chengdu, 610054, China
kangxie@uestc.edu.cn

Abstract ─ The positive-negative-positive metamaterial consisting of ferrimagnetic host and wire array is presented in this paper. Such metamaterial possesses three pass bands resulting from the interactions between the ferrimagnetic host and the wire array. The necessary parameter conditions are theoretically investigated and then the transmission and refraction properties are demonstrated by numerical method. The results show that the metamaterial exhibits three transmission peaks at frequencies of 7.1 GHz, 10.9 GHz, and after 15.5 GHz, respectively. The refraction directions at corresponding frequencies show that the metamaterial indeed exhibits positive-negative-positive refractive characteristics. Such metamaterial offers the potential applications, such as, multiband band pass filter, wavelength divider, and coupler.

Index Terms ─ Ferrimagnetic host, metamaterial, positive-negative-positive refraction.

I. INTRODUCTION

Metamaterial [1], so-called negative index material (NIM) or double-negative (DNG) material with simultaneously negative permittivity ε and permeability μ, has attracted more attention since the publication of Smith et al.'s initial paper [2], which demonstrated the existence of such a medium. Much of the fascination arises from the unusual electromagnetic properties, such as, reversals of both Doppler shift and Cherenkov radiation [1], enhancement of evanescent waves, and sub-wavelength resolution imaging [3], etc. Most of metamaterials are realized by artificial metallic structures with metallic plasma resonance, such as, using wires to provide negative permittivity and using split-ring resonators (SRR) to provide negative permeability [2], [4–6].

Some researchers, recently, proposed another metamaterial composed of ferrimagnetic host and wires [7–10]. The ferrimagnetic metamaterial, however, can also exhibit positive-negative-positive refractive characteristics at microwave frequencies that have not been discussed in previous published papers [7–10]. This characteristic is significantly different from other metamaterials [2], [4–6]. Metamaterials consisting of cut wires and SRR can exhibit a transmission band in a special frequency region with a negative refractive index characteristic and exhibit big loss below and above the negative frequency region. These metamaterials may also possess the positive-negative-positive refractive characteristic; but the two-side transmission bands of these metamaterials are not indistinctly shown due to the big loss and the metallic structure multiband metamaterials are limited in a narrow band or not at all tunable.

Since the multiband metamaterials offer potential applications, such as multiband pass filters, wavelength dividers, and couplers, it should be discussed further in this paper. The necessary parameter conditions of the positive-negative-positive metamaterial must be found out first by analyzing the theoretically effective electromagnetic parameters. And then the positive-negative-positive refractive characteristic is

investigated numerically. Finally, some conclusions are provided.

II. THEORETIC ANALYSIS

The previous works show that the metamaterial consisting of a ferrimagnetic host and wire array can achieve negative refraction in given frequency band when a plane electromagnetic wave propagates to the surface of the sample under applied magnetic field [10]. It can be found that such metamaterial can also exhibit three pass bands due to the interactions between the ferrimagnetic host and wire array. Therefore, this paper mainly focuses on such characteristics that have not been reported previously.

The single unit cell of original model [7], of the ferrimagnetic metamaterial, is shown in Fig. 1. The conducting region is within the circle of radius r_1. The region between r_1 and r_2 is filled with a dielectric insulator. The region surrounding the cladded wire is filled with ferrimagnetic material. All of these sizes are much smaller than the free-base wavelength λ_0 at the central frequency, 11 GHz. The whole structure has infinite size in the x and z directions. An EM wave propagates along the y axis with the electronic field along the z axis and the magnetic field along the x axis, and a dc applied magnetic field acts on the ferrimagnetic host along the z axis.

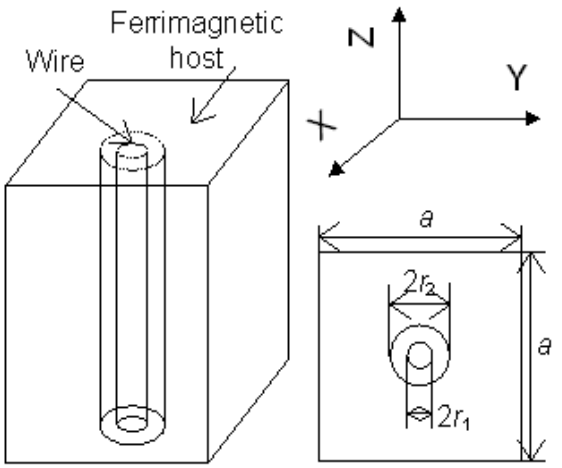

Fig. 1. Single unit cell (left) and top view (right) of the positive-negative-positive metamaterial composed of ferrimagnetic host and wire array.

This model presented here is the same as [7], so the effective permeability, μ_{eff}, and permittivity, ε_{eff}, of the metamaterial can be obtained from the following expression [7]:

$$\frac{\mu_{eff}}{\mu_0} = \frac{(H+M_S)^2 - (\omega/\mu_0\gamma)^2}{H(H+M_S) - (\omega/\mu_0\gamma)^2}, \quad (1)$$

$$H = H_0 - i(\frac{\omega}{\mu_0\gamma})(\frac{\Lambda}{\mu_0\gamma M_S}), \quad (2)$$

$$\frac{\varepsilon_{eff}}{\varepsilon_0} = \frac{\varepsilon_f}{\varepsilon_0} - \frac{\sigma_{eff}/\omega\varepsilon_0}{i + (\frac{\omega a^2 \sigma_{eff}}{2\pi})\left(\mu_0 \ln(\frac{r_2}{r_1}) + \mu_{eff}\left(\ln(\frac{a}{r_2}) - 1.06\right)\right)}. \quad (3)$$

Here M_S is saturation magnetization of ferrimagnetic host, H_0 is dc applied magnetic field, γ is gyromagnetic ratio, and Λ is a phenomenological damping parameter describing losses intrinsic to the ferrimagnetic host [7]. ω is angle frequency, ε_f is permittivity of ferrimagnetic host, ε_0 and μ_0 are permittivity and permeability of air, respectively, and σ_{eff} is effective conductivity of wire array. In the process of obtaining the effective permeability and permittivity, we have assumed that the EM wave propagates perpendicular to wires with the electronic field parallel to it and the magnetic field perpendicular to it, and a dc applied magnetic field acts on the ferrimagnetic host along the wires. Therefore, one can use the effective parameters shown in equations (1) – (3) to express the properties of the magnetic material and wire array [11, 12].

As shown in Ref. [7], Dewar claimed that the parameter values must be chosen properly so that such metamaterial can achieve a negative refraction. However, such metamaterial can, also, achieve three transmissions with positive-negative-positive refractive characteristics by redesigning the parameter values. This property can be used to explain why there are some unexpected pass bands in ferrimagnetic host based tunable metamaterials as shown in our previous paper [10].

To design a positive-negative-positive metamateial at microwave frequencies, the effective electromagnetic parameters are analyzed firstly. It can be calculated simply from equations (1) and (2) by using the following ferrimagnetic material's

parameter values: $M_S = 2 \times 10^5$ A/m, $H_0 = 1.39 \times 10^5$ A/m, and $\Lambda = 1 \times 10^9$. The big phenomenological damping parameter Λ presented here is used to display clearly the real part of μ_{eff} and the ferromagnetic resonance (FMR) frequency f_{FMR} [4]. For a general quality ferrimagnetic host, the Λ may be 10 – 20 times smaller than the above values. The parameter values presented above are used to show a microwave frequency metamaterial. These values can also be used for particular metamaterials [10]. The calculated μ_{eff} is shown in Fig. 2(a) (black lines). However, the ε_{eff} is difficult to satisfy the expected result, in which the composite medium must show positive-negative-positive refractive characteristics, due to the complex expression in equation (3). Here the Matlab software is used to numerically calculate and optimize the parameter values of showing expected three pass bands.

Since the copper wires are used to calculate the effective permittivity in this paper, and the copper wire's skin depth δ is much smaller than the wire radius. So the effective conductivity of the wire array is given by [7]

$$\sigma_{eff} = \frac{\sigma 2\pi r_1 \delta}{a^2},\ \delta = \sqrt{\frac{2}{\mu_0 \sigma \omega}}. \qquad (4)$$

Here σ is conductivity of copper wire. Hence, the parameter values of effective permittivity ε_{eff} are optimized finally and the calculated result is shown in Fig. 2(a) (grey lines with dots). The effective complex propagative constant k calculated from the ε_{eff} and μ_{eff} with $k=2\pi f\cdot(\varepsilon\varepsilon_0\cdot\mu\mu_0)^{1/2}$ is also shown in Fig. 2(b). The optimized parameters are shown as follows: $\varepsilon_f = 4\varepsilon_0$, $a = 2.4 \times 10^{-3}$ m, $r_1 = 2 \times 10^{-5}$ m, $r_2 = 1.5 \times 10^{-4}$ m. Therefore, the normalized electrical size (periodic size/wavelength ratio) of the designed metamaterial at the central frequency is about 0.088.

From Fig. 2(a), it can be known that in the frequency range of 9.6 GHz – 11.8 GHz both the μ_{eff} and ε_{eff} are negative, while in the ranges of 6.4 GHz – 7.7 GHz and after 14.5 GHz both the μ_{eff} and ε_{eff} are positive. This means that the EM waves can be transferred in the three frequency ranges with positive-negative-positive refractive characteristics. As shown in Fig. 2(b), the imaginary parts, which imply the loss in such metamaterial, of the propagative constant k in the ranges of 6.4 GHz – 7.7 GHz and 9.6 GHz – 11.8 GHz are larger than in the range of after 14.5 GHz. So the losses in the first two ranges are larger than the third range.

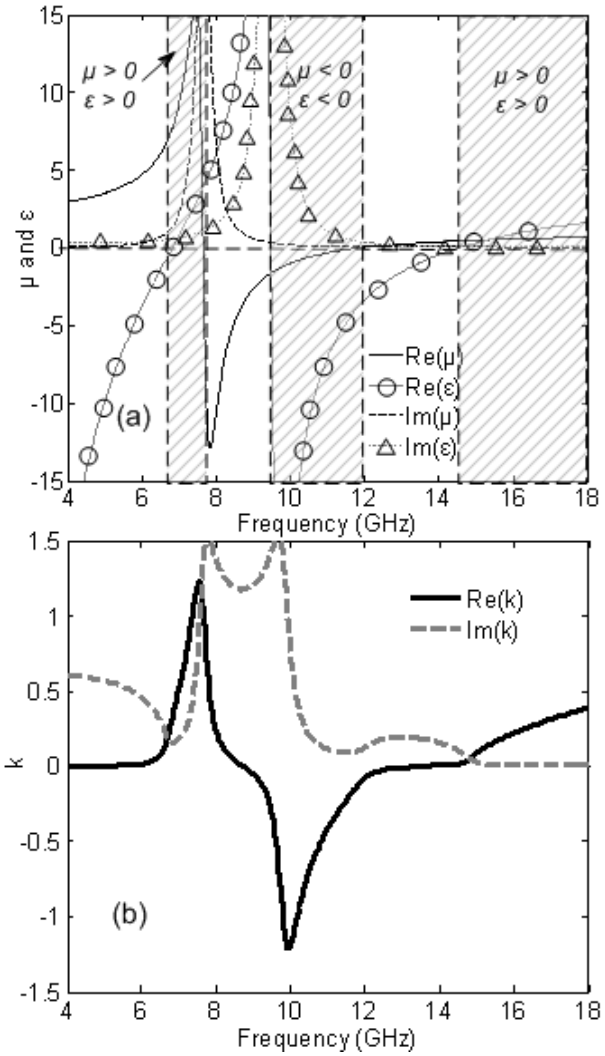

Fig. 2. (a) The effective permeability (black lines) and the effective permittivity (grey lines with dots) calculated from the equations (1)-(4). (b) The effective complex propagative constant k calculated from the ε_{eff} and μ_{eff} with $k=2\pi f\cdot(\varepsilon\varepsilon_0\cdot\mu\mu_0)^{1/2}$.

Why have the three pass bands appeared? Dewar has proved that the negative permeability of ferrimagnetic host would damage the negative permittivity property of wire array unless the wires are cladded with dielectrics [12]. And the thickness of cladding is crucial for appearing negative refraction and other characteristics. Therefore, one can design the parameter values so that the effective permittivity has both positive and negative values in the frequency band of negative permeability [see Fig. 2(a)], resulting in a positive-negative-positive metamaterial.

III. SIMULATION

In this section, the positive-negative-positive refractive characteristic of the above analyzed metamaterial is numerically demonstrated by utilizing a commercial finite-element based electromagnetic solver (HFSS, Ansoft) with the parameter values mentioned above.

To simulate the transmission properties in a broad frequency band (4 GHz – 18 GHz), a planar waveguide system (inserted in Fig. 3) with a cross section of 48 × 8 mm^2 is used. The metamaterial slab, with two layers, is put in the middle of the planar waveguide and the two side walls are Master and Slave Boundaries. So the simulated model has infinite boundary in the x and z directions. It is the same as the theoretical model and a dc applied magnetic field acts on the ferrimagnetic host along the wires.

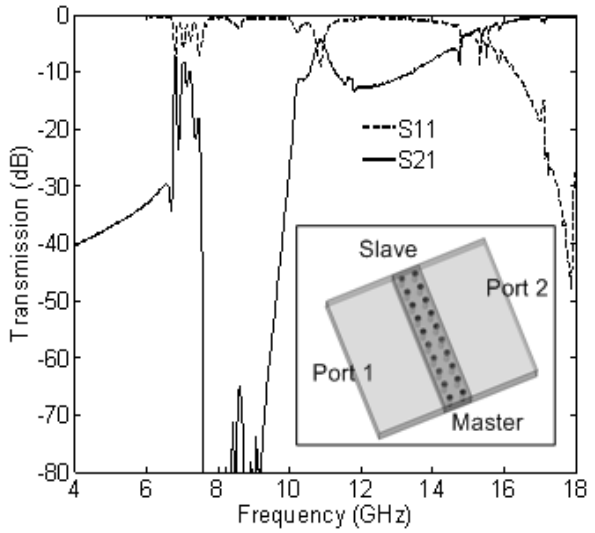

Fig. 3. Numerically simulated transmission properties of the ferrimagnetic metamaterial. The magnitudes of S_{11} (dotted line) and the S_{21} (solid line) are presented. The simulated model is also inserted in this figure.

Figure 3 shows the simulated transmission properties of the ferrimagnetic metamaterial in a broad frequency band. It can be seen that the metamaterial slab exhibits three transmission pass bands in the ranges of 6.7 GHz – 7.5 GHz, 10.2 GHz – 11.5 GHz, and after 15 GHz with transmission peaks at 7.1 GHz, 10.9 GHz, and 15.5 GHz, respectively. Moreover, the transmission amplitude values (S_{21}) at 7.1 GHz and 10.9 GHz are smaller than the value after 15.5 GHz, and the reflection values at 7.1 GHz and 10.9 GHz are larger than the value after 15.5 GHz. The smaller transmission values in the first two ranges result from the larger imaginary part of the effective propagative constant k shown in Fig. 2(b). The larger reflections in the first two ranges are due to the mismatch between metamaterial and air. These simulated results, shown in Fig. 3, agree with the theoretical results shown in Fig. 2, very well. When we change the number of layers, the transmission characteristic is not changed except for a small loss in such metamaterials (This result is not shown in this paper).

Moreover, the three pass bands of the ferrimagnetic metamaterial can be tuned by changing the dc applied magnetic field. The tunability is the particular characteristic of the ferrimagnetic metamaterial and has been discussed in Ref. [10], so it is not discussed in this paper.

Generally, to investigate a new metamaterial, most researchers would retrieve the effective parameters with the method proposed by Smith et al. [12] from the scattering parameters. In this paper, however, we do not retrieve the effective parameters, but directly investigate the refraction properties of the metamaterial at the three peak points shown in Fig. 3. The schematic of refraction system and the model of the prism sample are shown in Fig. 4(a). The wedge of the prism sample presented here is 18.43°, and a dc applied magnetic field, also, acts on the ferrimagnetic host along the wires. The incident beam impinges onto the sample at normal incidence with a Gaussian intensity profile tailored by side absorbers. For this condition of excitation, the electromagnetic wave undergoes refraction at the second tilted interface.

Figure 4(b)-(d) show the maps of the normalized electric field magnitude at various frequencies calculated at the mid-plane between the top and bottom perfect E conductors. The black arrow and the dash-dot line indicate the direction of the refracted beam and the normal to the second tilted interface, respectively. For frequencies of 7.1 GHz and 15.5 GHz [Fig. 4(b) and 4(d)], it can be seen that the angles of the two refracted beams are in the positive direction with respect to the normal as expected for a positive dispersion branch. At 10.9 GHz [Fig. 4(c)], the peak of the refracted beam is directed along a negative angle with respect to the normal and is consistent with the negative branch. Moreover, the

refracted power at 15.5 GHz [Fig. 4(d)] is much higher than the refracted powers at 7.1 GHz and 10.9 GHz [Fig. 4(b) and 4(c)]. That is because the losses and reflections at 7.1 GHz and 10.9 GHz are larger than those at 15.5 GHz [see Fig. 3]. These refraction phenomena at different frequencies agree with the theoretical results shown in Fig. 2 and the simulated three pass bands characteristic shown in Fig. 3, very well.

In the numerical results presented above, there is no spatial dispersion that has been discussed in [13, 14]. This is because the one-dimensional wire array has infinite length along the *z* direction and periodic boundary in the *x* direction.

This model is, also, the same as the theoretical analysis mentioned in section II. Furthermore, Pendry [3] discussed that three-dimensional wire array should be coated with some magnetic materials for reducing the spatial dispersion to achieve negative permittivity [15]. However, he has, also, shown that there is no spatial dispersion for the condition when the electric field is parallel to one of the three sets of wires. In this paper, the ferrimagnetic magnetic material is used to provide the negative permeability. So this is not the same condition and therefore, there is no spatial dispersion.

IV. CONCLUSION

In this paper, a positive-negative-positive metamaterial consisting of ferrimagnetic host and wire array is discussed. The necessary parameter conditions of such metamaterial are investigated theoretically. Then the three transmission passbands property and the positive-negative-positive refraction phenomena in different frequencies are numerically investigated. Both the theoretical and numerical results show that the metamaterial exhibits a positive-negative-positive refractive characteristic. Since such metamaterial has very small normalized electrical size of 0.088, it shows the potential applications such as novel multiband band pass filter, wavelength divider, and coupler, etc. Moreover, the arbitrary controllability of effective permeability and permittivity in the ferrimagnetic metamaterial and the tunability of operating frequency open a way to design an invisible cloak and absorber at arbitrary frequencies.

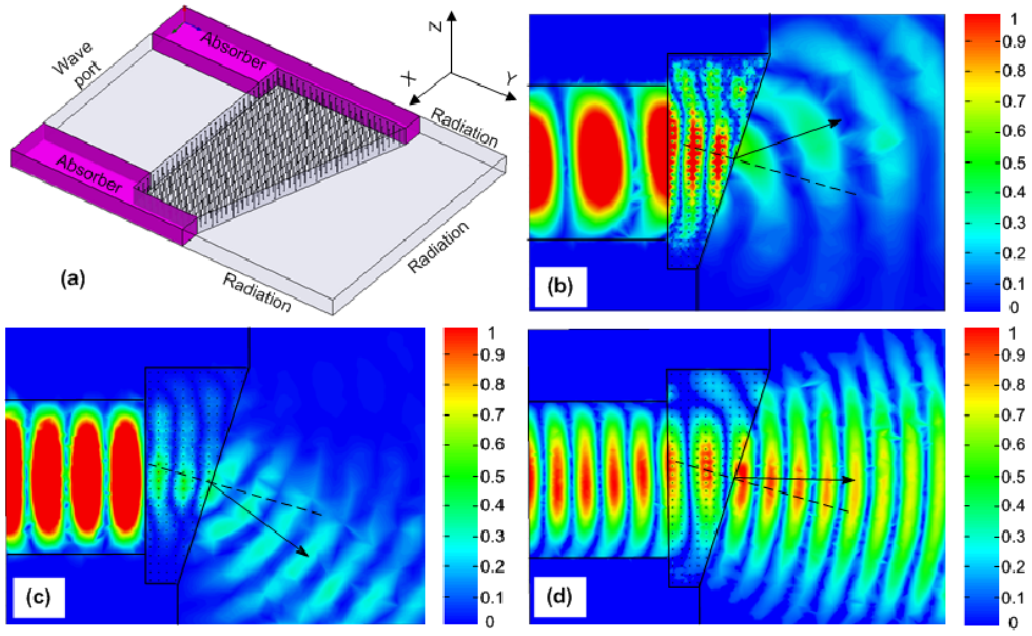

Fig. 4. (a) Schematic of the refraction system and numerically demonstrated refraction phenomena of the metamaterial in different frequency points: (b) 7.1 GHz; (c) 10.9 GHz; (d) 15.5 GHz.

ACKNOWLEDGMENT

This work was supported by the National Nature Science Found of China under Grant Nos. 60571024, 60771046, and 60588502.

REFERENCES

[1] V. G. Veselago, "The electrodynamics of substances with simultaneously negative values of ε and μ," Sov. Phys. Usp., vol. 10, no. 4, pp. 509-514, 1968.

[2] D. R. Smith, W. J. Padilla, D. C. Vier, S. C. Nemat-Nasser, and S. Schultz, "Composite medium with simultaneously negative permeability and permittivity," Phys. Rev. Lett., vol. 84, no. 18, pp. 4184-4187, May 2000.

[3] J. B. Pendry, "Negative refraction make a perfect lens," Phys. Rev. Lett., vol. 85, no. 18, pp. 3966-3369, 2000.

[4] J. Huangfu, L. Ran, H. Chen, X. Zhang, K. Chen, T. M. Grzegorczyk, and J. A. Kong, "Experimental confirmation of negative refractive index of metamaterial composed of Omega-like metallic patterns," Appl. Phys. Lett., vol. 84, no. 9, pp. 1357-1359, 2004.

[5] H. Chen, L. Ran, J. Huangfu, X. Zhang, K. Chen, T. M. Grzegorczyk, and J. A. Kong, "Left-handed materials composed of only S-shaped resonators," Phys. Rev. B, vol. 70, pp. 073102-1-3, 2004.

[6] R. W. Ziolkowski, "Design, fabrication, and testing of double negative metamaterials," IEEE Transactions on Antennas and Propagation, vol. 51, no. 7, pp. 1516-1528, 2003.

[7] G. Dewar, "Minimization of losses in a structure having a negative index of refraction," New Journal of Phys., vol. 7, pp. 161-1-11, 2005.

[8] Y. J. Cao, G. J. Wen, K. M. Wu, and X. H. Xu, "A novel approach to design microwave medium of negative refractive index and simulation verification," Chin. Sci. Bull., vol. 52, no.4, pp. 433-439, 2007.

[9] H. J. Zhao, J. Zhou, Q. Zhao, B. Li, L. Kang, and Y. Bai, "Magnetotunable left-handed material consisting of yttrium iron garnet slab and metallic wires," Appl. Phys. Lett., vol. 91, no. 13, pp. 131107-1-3, 2007.

[10] Y. J. Huang, G. J. Wen, T. Q. li, K. Xie, "Low-Loss, Broadband and Tunable Negative Refractive Index Metamaterial," J. Electromagnetic Analysis & Applications, vol. 2, no.2, pp.104-110, 2010.

[11] B. Lax and K. J. Button, Microwave Ferrites and Ferrimagnetics, McGraw-Hill, New York, 1962, 7, 304.

[12] G. Dewar, "The applicability of ferrimagnetic hosts to nanostructured negative index of refraction (left-handed) materials," in proceeding of SPIE, vol. 4806, pp. 156-166, 2002.

[13] D. R. Smith, D. C. Vier, Th. Koschny, and C. M. Soukoulis, "Electromagnetic parameter retrieval from inhomogeneous metamaterials," Phys. Rev. E, vol. 71, no. 3, pp. 036617-1-11, 2005.

[14] P. A. Belov, R. Marques, S. I. Maslovski, I. S. Nefedov, M. Silveirinha, C. R. Simovski, and S. A.Tretyakov, "Strong spatial dispersion in wire media in the very large wavelength limit," Phys. Rev. B, vol. 67, pp. 113103-1-4, 2003.

[15] M. G. Silveirinha, C. A. Fernandes, and J. R. Costa, "Electromagnetic characterization of textured surfaces formed by metallic pins," IEEE Trans. Antennas Propagat., vol. 56, no. 2, pp. 405-415, Feb. 2008.

[16] A. Demetriadou and J. B. Pendry, "Taming spatial dispersion in wire metamaterial," J. Phys.: Condens. Matter, vol. 20, pp. 295222-1-11, 2008.

Yongjun Huang was born in Sichuan, China, in 1985. He received his B.S. in Mathematics from NeiJiang Normal University of China in 2007 and will receive his M. S. in Communication Engineering from University of Electronic Science and Technology of China in 2010. His dissertation work and research activities are electromagnetic metamaterial and its application in microwave engineering area, FDTD analysis for the model and RCS characteristic of metamaterials.

Guangjun Wen was born in Sichuan, China, in 1964. He received his M.S. and Ph.D. from Chongqing University of China in 1995 and from University of Electronic Science and Technology of China in 1998, respectively. He is currently a professor and doctor supervisor at University of Electronic Science and Technology of China.

His research and industrial experience covers a broad spectrum of electromagnetics, including RF, Microwave, Millimeter wave Integrated Circuits and Systems design for Wireless Communication, Navigation, Identification, Mobile TV applications, RFIC/MMIC/MMMIC device modeling, System on Chip (SoC) and System in Package (SiC) Design, RF/Microwave/Millimeter wave Power source Design, "The Internet of things" devices and system, RFID system and networks, antennas, as well as, model of electromagnetic metamaterial and its application in microwave engineering area.

Kang Xie was born in 1965. He received his M.S. and Ph.D. from Xi'an Jiaotong University of China in 1988 and from University of Salford in 1993. He was Research Assistant and Research Fellow at University of Salford in 1992-1997, Research Associate at University of Manchester in 1997-2000, Senior Engineer, Principal Engineer, Staff Scientist at COM DEV Europe LTD in 2000-2003, and Principal Member of Technical Staff of COM DEV Europe LTD in Sept. 2003.

He is currently a professor and doctor supervisor at University of Electronic Science and Technology of China. His research activities are Optical engineering, microwave opto-electronics, Nonlinear optical.

Three-Dimension Finite Element Analysis of a Helical Motion Induction Motor

J. H. Alwash[1] and L. J. Qaseer[2]

Department of Electrical Engineering
Uuniversity of Baghdad, Jaderia, Baghdad, Iraq
jalwash@yahoo.com

General & Theoretical Electrical Engineering Department
University of Duisburg-Essen
Bismarckstrasse 81, 47057, Duisburg, Germany
laythqaseer@yahoo.com

Abstract **-** The paper presents a three-dimensional finite element analysis applicable to all forms of sheet rotor, cylindrical, linear induction motor, as well as, helical motion induction motor. The analysis accounts for longitudinal and transverse end effects, skin depth and finite sheet thickness; furthermore, there is practically no restriction on the shape of magnetic circuit that can be considered. It yields detailed space profile of the state variables. The winding arrangement may include multi-polar system circumferentially and axially. The excitation produced by such winding is a helically traveling wave. The formulation results in a set of linear equations which are solved by point relaxation method. The solution algorithm employs power mismatch in the machine to indicate accuracy. The theory is supported by experimental results.

Index Terms **-** AC machines, finite element methods, induction motors, numerical analysis.

I. INTRODUCTION

The two-degree of mechanical freedom actuator capable of linear, rotation, or helical motion would be a desirable asset to the fields of machine tools and robotics. The magnetic circuits suggested for such a machine use laminations transverse to the direction of motion.

In a previous paper [1], a tubular motor with a double helical winding was presented using a multi–layer mathematical model for the analysis. Mendrela and Turowski [2], Fleszar and Mendrela [3], and Mendrela and Gierczak [4] reported analysis of helical motion induction motor (HMIM) using the Fourier series method which takes into account the end effects.

Cathey [5] and Rabiee and Cathey [6, 7] had presented a helical motion induction motor and a procedure was developed for the determination of the equivalent circuit parameters even though the magnetizing inductance is small for a typical secondary of conducting sleeve design. It was shown that under appropriate definition of slip the Steinmetz equivalent circuit of an induction motor can be applied to this two degree of freedom machine.

In a later paper, Alwash, Mohssen and Abdi [8] presented a multi–layer theory analysis of HMIM with any number of axial and circumferential poles and that the method retains the true cylindrical topology of the machine under consideration.

The object of this paper is to present a three–dimensional (3-D) finite element analysis of HMIM, since the helical winding topology is not axisymmetric and, hence, cannot be analyzed using a two-dimensional finite element method. The formulation is derived using a variational approach, the problem of induction in moving media is being treated by the extension of a

previous finite element solution, of electromagnetic field problems [9, 10]. The solution, which appears to behave well numerically, employs a convergence test devised from power balance considerations in the machine.

II. THEORETICAL ANALYSIS

The general outline of the model is shown in Fig. 1. *r,* θ and *z* are cylindrical coordinates. The quantities p_z, V_θ and V_z represent axial pole pitch, circumferential rotor velocity and axial rotor velocity respectively. The rotor conducting sheet moves in both axial (z) and circumferential (θ) directions.

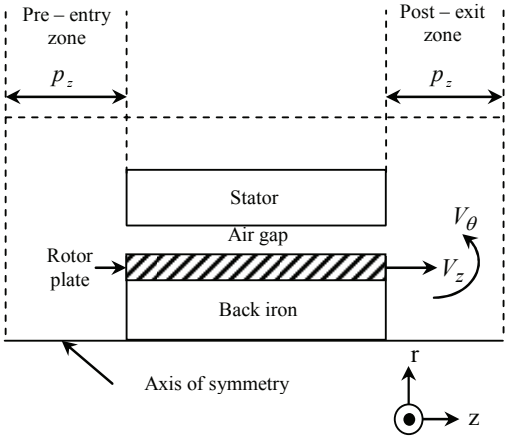

Fig. 1. General outline of the model.

The solution, where ω represents the angular frequency, is based on the following assumptions:

1. The stator current is known and has two cylindrical components, namely J_θ and J_z.
2. All fields vary with time as $\exp(j\omega t)$ and decay to zero at sufficiently far distances from the machine axis.
3. Displacement currents and laminated iron conductivity are not considered.

The above assumptions are quite common in machine analysis. It is noted that they impose no restriction on the topology of the machine in the rz – plane, thus allowing treatment of all practical forms of sheet rotor cylindrical linear induction motors.

A. Stator current density

It is assumed that the winding produces perfect sinusoidal traveling wave. The line current density J_o may be represented as [8]:

$$J_o = J_s \exp j(\omega t - kz + n\theta), \tag{1}$$

where *k* and *n* represent the wave length factor defined below and number of circumferential pole pairs in helical system respectively. The stator line current density J_s is defined as:

$$J_s = J_m \exp(j\phi),$$

where

$$\phi = \tan^{-1}\frac{n}{k \cdot r_g}, \tag{2}$$

$$k = \frac{\pi \cdot \cos(\phi)}{p}, \tag{3}$$

with J_m, ϕ, r_g and *p* representing amplitude of line current density, helicoid angle, inner stator radius and normal pole pitch respectively.

B. Governing equations

For a 3-D analysis, Maxwell's equations require that the vector potential $A(r,\theta,z)$ satisfies [9], such that

$$\nabla \times \left(\frac{1}{\mu}\nabla \times \overline{A}\right) = \overline{J}, \tag{4}$$

where $\overline{A}$ and $\overline{J}$ represent the three dimensional magnetic vector potential and the current density vector respectively. According to assumption (1), the above equation leads to two Euler equations in cylindrical coordinates (or three equations in Cartesian coordinates). Depending on the position, the current density takes the following values:

Stator winding region

$$\overline{J} = \overline{J}_0. \tag{5a}$$

Non conducting region

$$\overline{J} = \overline{0}. \tag{5b}$$

Rotor conducting sheet

$$\overline{J} = -j\omega\sigma\overline{A} + \sigma\left(\overline{V} \times \overline{B}\right), \tag{5c}$$

where σ, $\overline{V}$ and $\overline{B}$ represent rotor conductivity, three dimensional velocity vector and magnetic flux density vector. Equations (4) and (5), and the

zero potential conditions assumed at the outermost boundaries, as well as machine axis, specify the problem in differential form and should yield a unique solution for the magnetic vector potential.

Now, the solution of equation (4) is known to minimize the energy functional χ [12]

$$\chi = \iiint_{\Omega} \left\{ \frac{1}{2\mu}\left(B_r^2 + B_\theta^2 + B_z^2\right) - \overline{A}\cdot\overline{J} \right\} r dr d\theta dz \,, \quad (6)$$

where Ω denotes the entire domain considered in the analysis; this may be simply verified by applying Euler's theorem of variational calculus to show that (4) is the Euler equation corresponding to χ as defined in (6).

C. Performance calculations

Once the potential distribution in the system is known, it is possible to compute all quantities of interest. These include the rotor induced current density, flux density components, propulsion force, the rotational torque, the power supplied, the air gap power, the rotor ohmic losses, stator voltage, input power factor and the efficiency [9]. The performance parameters mentioned above require derivatives and integrals involving the magnetic vector potential. Only force calculations will be be considered here.

1) The propulsion force:

The calculation of propulsion force, in particular, requires some consideration, as there are three methods.

The first method is the Maxwell stress method which states that the time average axial force F_z on a volume element can be calculated by integrating the electromagnetic stress over its surface, with H_r, H_θ, and H_z being the radial, circumferential and axial components of magnetic field strength vector and μ_0 is the permeability of free space

$$F_z^e = \frac{1}{2}\mathrm{Re}\left\{ \iint_s \mu_o H_r H_z^* ds \right\}. \quad (7)$$

Choosing a volume which consists of a cylinder of radius R bounded at its ends by the outer boundaries, it is possible to write:

$$F_z^e = \frac{R(\Delta\theta)}{2}\mu_o \int_{z_{\min}}^{z_{\max}} \mathrm{Re}\left\{H_r H_z^*\right\} dz \,. \quad (8)$$

This requires finding the contribution to the force from all elements that span the radius R where the cylinder encloses the rotor. For a typical element shown in Fig. 2, the time average value of the force on the rotor conductor is given by:

$$F_z = \frac{R}{2\mu_o}\left[z_{\max} - z_{\min} \right] . \sum_e \mathrm{Re}\left\{ B_r^e B_z^{*e} \right\} (\Delta\theta) . \quad (9)$$

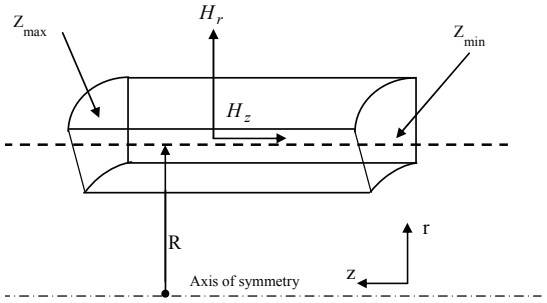

Fig. 2. Typical element for the calculation of propulsion force.

The second method is $\overline{J}\times\overline{B}$ on a stator winding region where the time average propulsion force per unit volume is obtained by taking the z – component in (9), therefore

$$f_z^e = -\frac{1}{2}\mathrm{Re}\left\{ J_\theta^e B_r^{*e} \right\} \quad \mathrm{N/}m^3 \,.$$

Hence, the time average propulsion force on an element can be written as:

$$F_z^e = -\frac{1}{2}\mathrm{Re}\left\{ \iiint_e J_\theta^e B_r^{*e}\, r dr d\theta dz \right\},$$

and the total time average propulsion force on the rotor conductor now becomes:

$$F_z = -\frac{1}{2}\sum_e \mathrm{Re}\left\{ J_\theta^e B_r^{*e} \right\} \Delta v \quad \mathrm{N}, \quad (10)$$

where $\Delta v = r_c \Delta r \Delta\theta \Delta z$.

The summation is carried out over all elements in the stator winding region.

The third method is $\overline{J}\times\overline{B}$ on rotor region

where the calculation of the force by $\left(\overline{J}\times\overline{B}\right)$ on an eddy current region is similar to that on a current source region. The only difference being that the induced current density is used rather than the specified stator current density. For an iron cored rotor rotary-linear motor, this method can lead to errors as it neglects the forces which act directly on the iron.

2) The rotational force:

The time average rotational force per unit volume is given by

$$f_\theta^e = \frac{1}{2}\mathrm{Re}\left\{J_z^e B_r^{*e}\right\} \quad \mathrm{N}/m^3$$

$$\text{or} \quad F_\theta^e = \frac{1}{2}\mathrm{Re}\left\{\iiint_e J_z^e B_r^{*e}\, dv\right\} \quad \mathrm{N},$$

and the total time average rotational force on the rotor conductor now becomes

$$F_\theta = \sum_e F_\theta^e \,, \tag{11}$$

where the summation is carried out over all elements in stator winding region. The circumferential (rotational) torque can be obtained simply by multiplying the circumferential force by the radius of the stator over which the integration is carried out.

3) The radial force:

The radial component of the Lorentz force per unit volume on each element in a conductor is given by

$$f_r^e = \frac{1}{2}\mathrm{Re}\left\{J_\theta^e B_z^{*e} - J_z^e B_\theta^{*e}\right\} \quad \mathrm{N}/m^3 .$$

Due to rotor circular symmetry of RLIM, the rotor experiences no radial force, therefore

$$F_r = \sum_e f_r^e\, dv = 0 .$$

III. EXPERIMENTAL MACHINE

To verify the theoretical results obtained through the computation, laboratory measurements were made on two experimental machines. The first model A was constructed by Cathey and Rabiee in [6,7]. It was an iron cored stator iron cored rotor machine. Extensive analysis for this model is made with standstill and variable speed analysis for the state variables.

Model B was constructed by Alwash, Mohssen and Abdi [8] at the University of Baghdad. The stator of this machine contains no iron and hence is considered as an open magnetic circuit. The model was tested with variable frequency under standstill conditions.

Table 1. Machine parameters for Model A.

Parameter	Value
Stator length, m	182.8
Phases	3
Circumferential poles	2
Axial poles	2
Slots per pole per phase	2
Slots per pole	6
Slots, axial & circumferential	12, 12
Normal coil width, mm	7.18
Normal slot pitch, mm	10.78
Normal pole pitch, mm	64.64
Helicoids angle on primary, degrees	45
Turns per coil	20
Stator phase current, A	15 r.m.s.
Frequency, Hz	60
Circumferential pole pitch at inner stator radius, mm	52.62
Air gap length, mm	2.78
Steel shaft diameter, mm	25.4
Copper sleeve thickness, mm	1.27
Copper rotor conductivity, S/m	4.48×10^7
Shaft relative permeability	750

Table 2. Machine parameters for Model B.

Parameter	Value
Stator length, m	203
Phases	3
Circumferential poles	2
Axial poles	4
Slots per pole per phase	1
Slots per pole	3
Slots, axial & circumferential	12, 6
Normal coil width, mm	7
Normal slot pitch, mm	12
Normal pole pitch, mm	36
Helicoids angle on primary, degrees	36.3
Turns per coil	160
Stator phase current, A	2.3 r.m.s.
Frequency, Hz	50/150/250

Circumferential pole pitch at inner stator radius, mm	50.27
Air gap length, mm	3.5
Steel shaft diameter, mm	25
Copper sleeve thickness, mm	3
Copper rotor conductivity, S/m	3.4×10^7
Shaft relative permeability	56

Tables 1 and 2 show the parameters of models A and B respectively. Table 3 shows the discretization data and CPU time for model A. The computer used was a Pentium 4 (2.4 GHz) PC.

Table 3. Discretization data and CPU time for Model A.

Number of element	325,247
Number of nodes	61,856
Number of edges	409,973
Total CPU time (hours)	1,238

IV. RESULTS

Figures 3 and 4 show respectively the variation of the propulsion force and the circumferential torque with respect to speed for model A at 60 Hz using the finite element method and equivalent circuit model adopted in [6,7] for the sake of comparison. The two methods agree within 5% for the propulsion force. For the circumferential torque, it is clear that the finite element method is closer to measured values than equivalent circuit method while both methods agree with maximum deviation of 5.2 %.

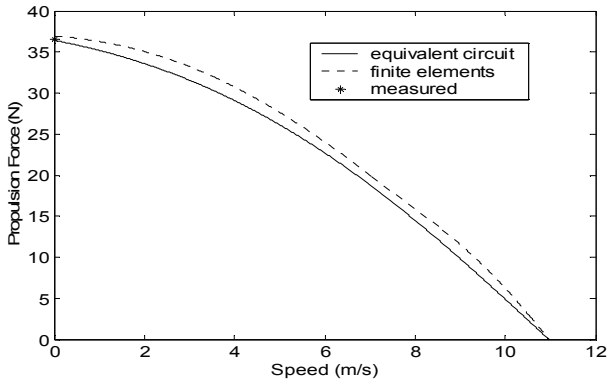

Fig. 3. Propulsion force against speed at 60 Hz for model A.

The power of the finite element method, in addition to its high accuracy compared to the analytical methods lies in its ability to display the effect of finite dimensions (end effects) of the actual machine.

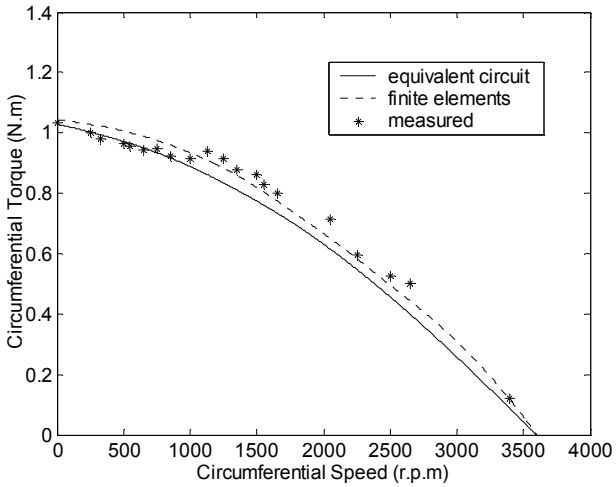

Fig. 4. Circumferential torque against speed at 60 Hz for model A.

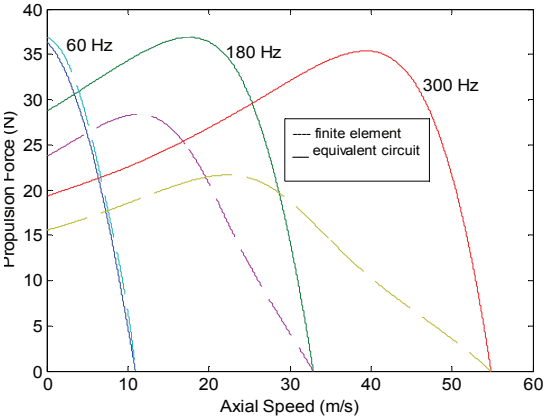

Fig. 5. End effects on propulsion force at different frequencies for model A.

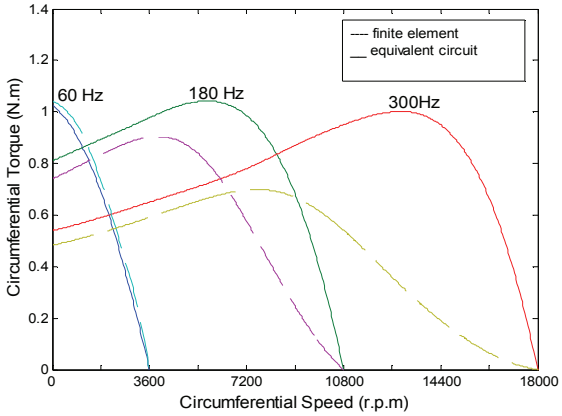

Fig. 6. End effects on circumferential torque at different frequencies for model A.

To validate this, Figs. 5 and 6 show the variation of force and circumferential torque with respect to speed for model A at 60, 180 and 300 Hz using the finite element method and equivalent circuit model. The results show that the end effects are prominent as frequency and speed increase [10] which affect the peak force and torque values when the finite element method is adopted.

Figures 7 to 9 show the flux profile of the model for the three components of flux density at frequency of 60 Hz using three different slips.

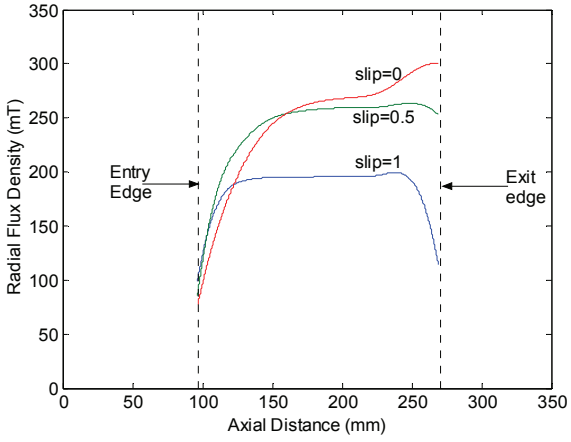

Fig. 7. Radial flux density distribution at 60 Hz for model A.

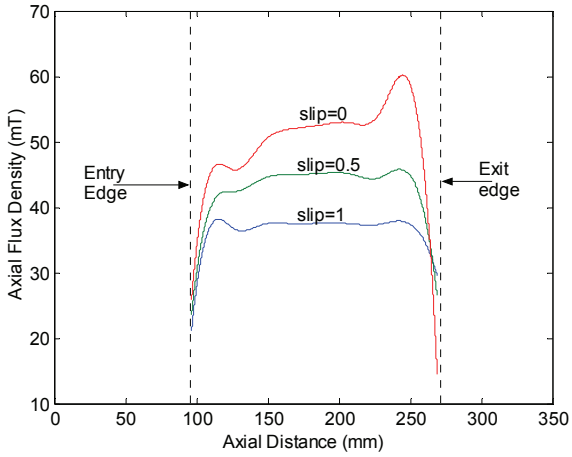

Fig. 8. Axial flux density distribution at 60 Hz for model A.

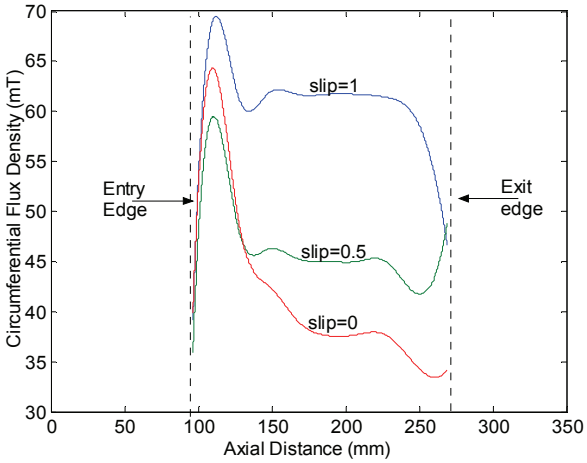

Fig. 9. Circumferential flux density distribution at 60 Hz for model A.

Figures 10 to 13 show the space profile for the rotor current density, air gap power, propulsion force and circumferential torque distributions for model A at standstill and frequencies of 60, 180 and 300 Hz where end effects are prominent and clearly visible.

Figures 14 to 17 show the variation of line terminal voltage, input power, input power factor and efficiency with respect to speed for model A using the finite element method.

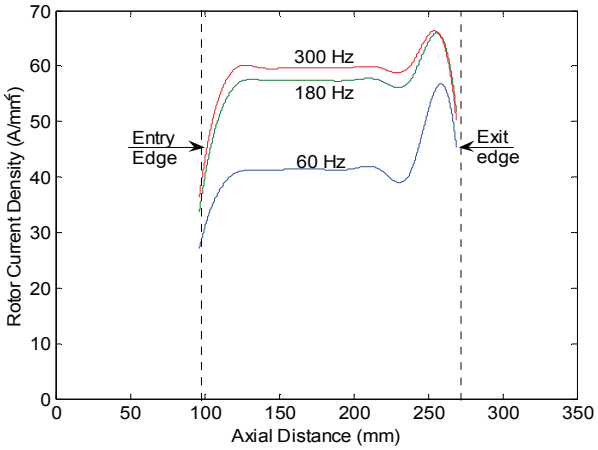

Fig. 10. Rotor current density distribution along axial distance at standstill for model A.

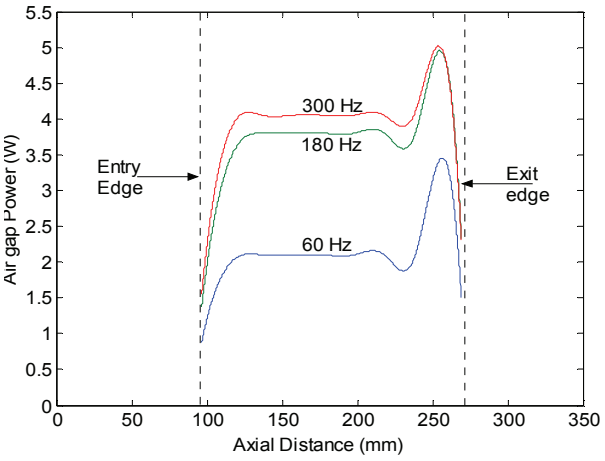

Fig. 11. Air gap power distribution along axial distance at standstill for model A.

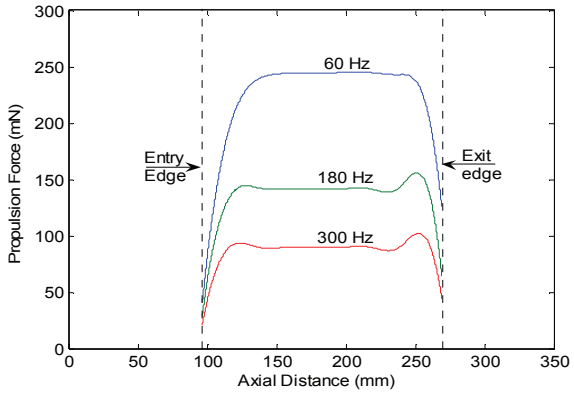

Fig. 12. Propulsion force distribution along axial distance at standstill for model A.

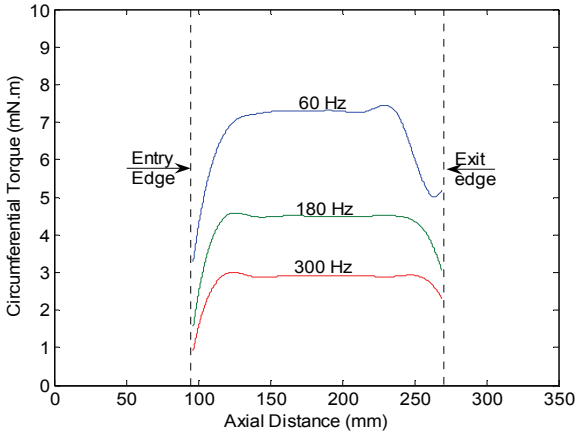

Fig. 13. Circumferential torque distribution along axial distance at standstill for model A.

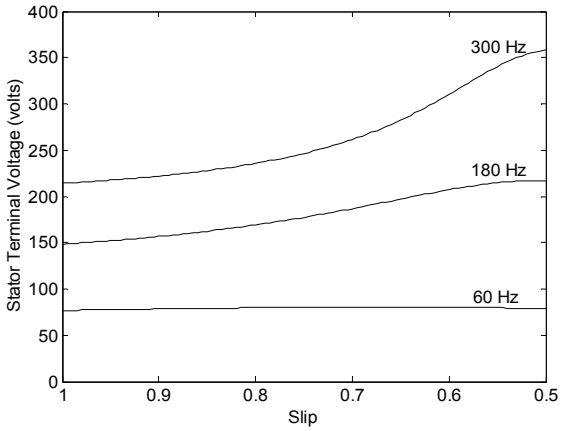

Fig. 14. Stator terminal voltage against speed at different frequencies for model A.

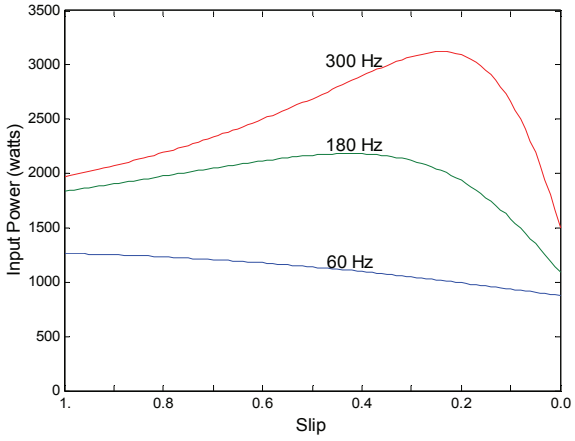

Fig. 15. Input power against speed at different frequencies for model A.

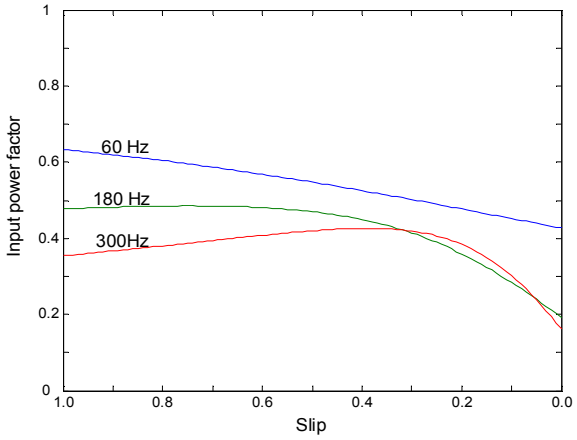

Fig. 16. Input power factor against speed at different frequencies for model A.

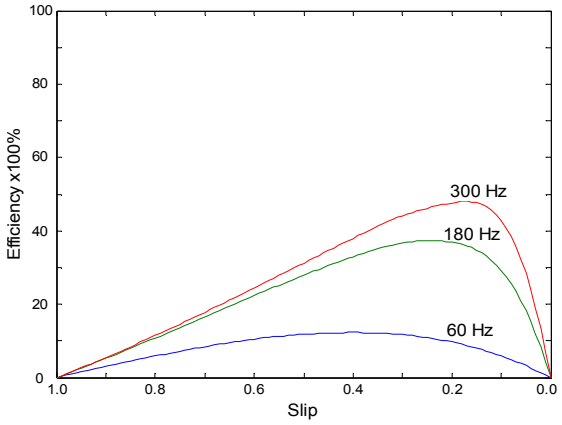

Fig. 17. Efficiency against speed at different frequencies for model A.

Figures 18 and 19 show respectively the variation of propulsion force with frequency for model B using a hollow aluminum rotor and a solid aluminum rotor by introducing the numerical results from the finite element analysis and the computed results of the layer theory approach adopted in [8] against measured values at standstill. Figures 20 and 21 show respectively the variation of the circumferential torque with frequency at standstill for model B using hollow and solid aluminum rotor by introducing finite element results and layer theory results against measured values.

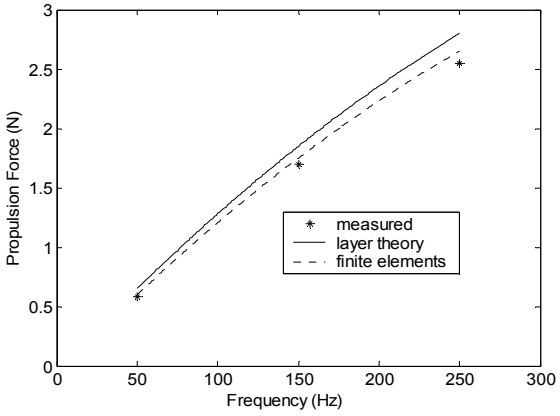

Fig. 18. Propulsion force against frequency for model B with hollow rotor.

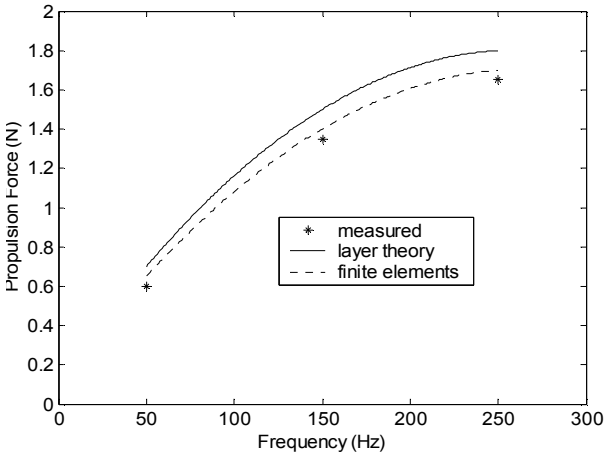

Fig. 19. Propulsion force against frequency for model B with solid rotor.

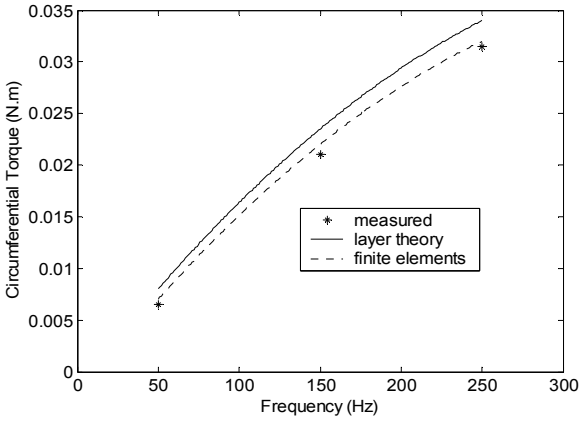

Fig. 20. Circumferential torque against frequency for model B with hollow rotor.

The agreement between layer theory and experimental results lies within a maximum deviation of 7.6% while the agreement between finite element and experimental results lies within a maximum deviation of 3.9%.

It is worth mentioning that in addition to the fact that the finite element method is closer to experimental results than the layer theory approach, the differences between the results of the layer theory approach and finite element computations increase with increasing frequency due to longitudinal end effects, which becomes more effective at higher frequencies.

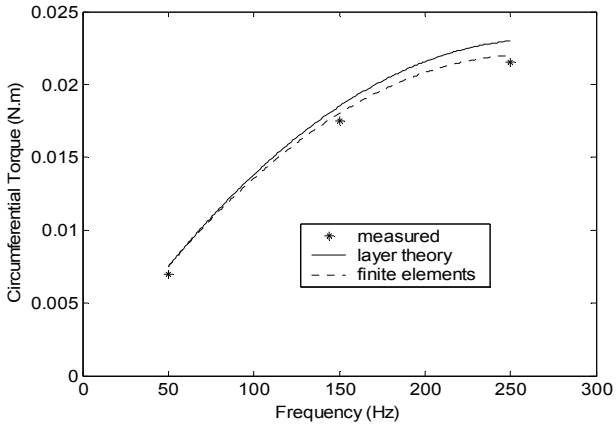

Fig. 21. Circumferential torque against frequency for model B with solid rotor.

V. CONCLUSION

The 3-D finite element method has been used for the analysis of helical motion induction motors. The methodology presented is quite general as it lends itself to the analysis of tubular linear induction motors and cylindrical induction heating systems. It is shown for the models considered that longitudinal end effects are most effective at higher frequencies and speeds. An important conclusion inferred from our study is that end effects must play an important part in these machines. The 3 – D finite element method has been shown to be eminently suited to the analysis of helical induction machines. The results, displayed and discussed in the previous section, show clearly that the finite element results agree well with the experimental ones more than any other closed form technique. This may be considered as a fair justification of the analysis method proposed in this paper.

ACKNOWLEDGMENT

L. J. Qaseer is deeply indebted to Daniel Erni, his host and co-worker at the University of Duisburg-Essen for advice and encouragement.

REFERENCES

[1] J. F. Eastham and J. H. Alwash, "Transverse flux tubular motors," *Proc. IEE*., vol. 112, no. 12, pp. 1709-1718, Dec. 1972.

[2] E. A. Mendrela and J. Turowski, "Rotary-linear induction motor," *IEEE winter power meeting*, New York, no. A78 091-1, 1978,

[3] J. Fleszer and E. A. Mendrela, "Twin–armature rotary–linear induction motor," *Proc. IEE* pt. B, vol. 130, no. 3, pp. 186–192, May 1983.

[4] E. A. Mendrela and E. Geirczak, "Double–winding rotary–linear induction motors," *IEEE Trans. Energy Convers.*, vol. EC–2, no. 1, pp. 48–54, March 1987.

[5] J. J. Cathey, "Helical motion induction motor," *Proc. IEE* pt. B, vol. 132, no. 2, pp. 112–114, March 1985.

[6] M. Rabiee and J. J. Cathey, "Verification of a field theory analysis applied to a helical motion induction motors," *IEEE Trans. Magn.*, vol. 24, no. 4, pp. 127–138, July 1988.

[7] J. J. Cathey and M. Rabiee, "Verification of an equivalent circuit model for a helical motion induction motor", *IEEE Trans. Energy Convers.*, vol. 3, no. 3, pp. 660–666, Sept. 1988.

[8] J. H. Alwash, A. D. Mohssen and A. S. Abdi, "Helical motion tubular induction motor," *IEEE Trans. Energy Convers.,* vol. 18, no. 3, pp. 362– 396, Sept. 2003.

[9] T. Yamaguchi, Y. Kawase, M. Yoshida, Y. Saito and Y. Ohdachi, "3 – D finite element analysis of a linear induction motor," *IEEE, Trans. Magn*., vol. 37, no. 5, pp. 3668–3671, Sept. 2001.

[10] M. A. Al–Maayouf, "*Study of a Linear Induction Motor Using Alternative Models,*" Ph. D thesis, City University, London, U. K., 1981.

J. H. H. Alwash was born in Babylon, Iraq, on March 7, 1945. He graduated from University College London in 1967 and obtained his Ph.D. degree from London University in 1972 as an internal student of both Kings College & Imperia college of Science & Technology. He is now a Professor of Electrical Engineering Department, University of Baghdad. His special fields of interest included induction machines (rotary, flat linear and tubular linear types) and induction heating.

L. J. B. Qaseer was born in Baghdad, Iraq, on October 14, 1957. He received his B.Sc., M. Sc. and Ph.D. degrees from the University of Baghdad in 1979, 1993 and 2004 respectively, all in electrical engineering. In 2005, he was with the Mechatronic Engineering Department at the University of Baghdad. Dr. Qaseer is currently with the General & Theoretical Electrical Engineering Department of the University of Duisburg-Essen, Duisburg, Germany. His special fields of interest include rotary, linear, tubular linear and helical motion induction motors, as well as, induction heating.

Micro-T Circuit Model for Double and Single Sided Induction Heating Systems

Layth Jameel Buni Qaseer

General and Theoretical Electrical Engineering Department
University of Duisburg-Essen, Bismarckstrasse 81, 47057 Duisburg, Germany
laythqaseer@yahoo.com

Abstract - A method is given for obtaining a phase terminal equivalent circuit, which is useful for the analysis of traveling wave as well as longitudinal flux induction systems for heating thin metal strips. The excitation is transverse to the direction of strip motion and can be realized as a three phase system or a single phase system where the strip could be ferromagnetic or nonmagnetic. First, a general form of the field solution is obtained using transfer matrices. A variable transformation is then made which makes it possible to derive an equivalent circuit for each planar region in the system. By joining the equivalent circuits in cascade, an equivalent circuit for the complete system is obtained. The voltages and currents in the equivalent circuit relate directly to the field quantities within the actual system.

Index Terms - Eddy currents, electromagnetic induction, energy conversion, equivalent circuits, induction heating.

I. INTRODUCTION

Traveling wave induction heating (TWIH) systems, as one of the multi-phase induction heating systems, have particular features which make them attractive to achieve various heating applications. Among the advantages are the possibility to heat, quite uniformly, thin strips without moving the inductor above its surface, to reduce the vibration of inductor and load due to electromagnetic forces and, also, the noise provoked by them, to obtain nearly balanced distributions of power and temperature, mechanical strength and the protection for the coils given by the ferromagnetic core [1-7]. The finite element method (FEM) is the most popular numerical method for the analysis of such systems and has been developed in 2-D and 3-D [2-4], [7-10]. Analytical solutions were almost exclusive to cylindrical induction heating systems [5-6], [11-14]. The layer theory approach is an analytical solution of the field problem applied to flat linear machines [15, 16] and cylindrical machines [17-19].

The aim of this paper is to show how the analytical solution to the field problem may be extended to yield an equivalent circuit representation for the induction heating systems.

It is usually straightforward to relate field quantities in the system to voltages and currents in the equivalent circuits. The approach in this paper is presented along a simple multi-region model.

A region in the system is defined by its uniform material in nature having boundaries of simple planar shape.

The equivalent circuits developed here seem to have the form of a cascade of cells made of lumped elements; hence it is possible to consider any number of regions.

The accuracy of the method is verified with measurements of practical induction heating systems, together with comparisons to numerical and analytical methods.

II. MATHEMATICAL MODEL

A general multi-region problem is analyzed. Figure 1 shows a cross section of the *N*-region model used in the theory. The model is taken to be an asset of infinitely long planar regions. The current sheet lies between regions r and r+1. The current sheet varies sinusoidally in the y-direction and with time. It is of infinite extent in the x-

direction and infinitesimally thin in the z-direction.

Regions *1-N* are layers of materials where the general region has a conductivity σ_n and relative permeability μ_n. It is further assumed that

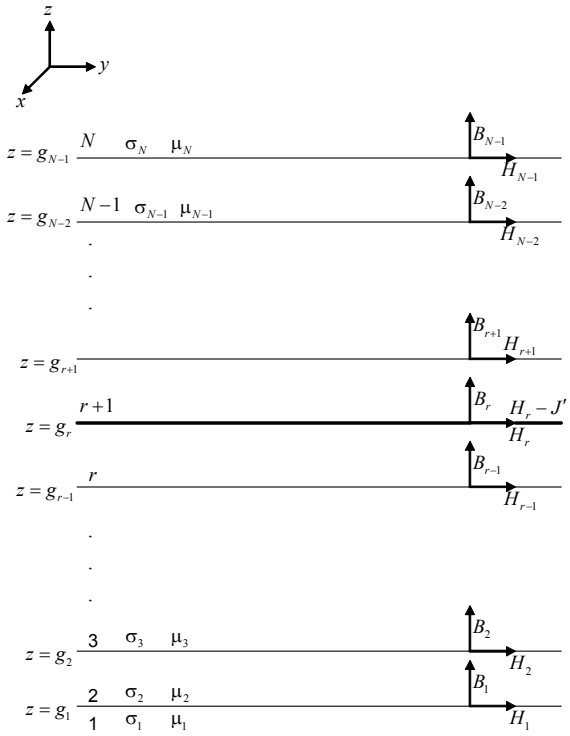

Fig. 1. Cross-section through cylindrical multi-layer induction heating system.

displacement currents at the working frequencies used (from main frequency to several kilohertz) are negligible [15-17] and magnetic materials are assumed linear.

The important field quantities are those acting at the region boundaries. For the models considered here, there are, at most, three field quantities that are relevant. These are the electric field strength E_x which is directed along the interface transverse to the direction of strip motion, the magnetic field strength H_y which is directed axially along the interface and the third one (if existing) is the flux density B_z normal to the interface. If these quantities are known, the equivalent circuit is then derived to obtain the important induction heating system parameters which are the terminal impedance, induced power and axial force.

The intermediate stage between the field solution and the final equivalent circuit is represented in a transmission line form. It is well known that the B_z and H_y values on either side of a region could be linked by a transfer matrix [17]. Hence, every bounded region in the model shown in Fig. 1 could be represented by a corresponding transfer matrix equation.

Figures 2 and 3 show the general outline of a double sided and a single sided induction heating system respectively.

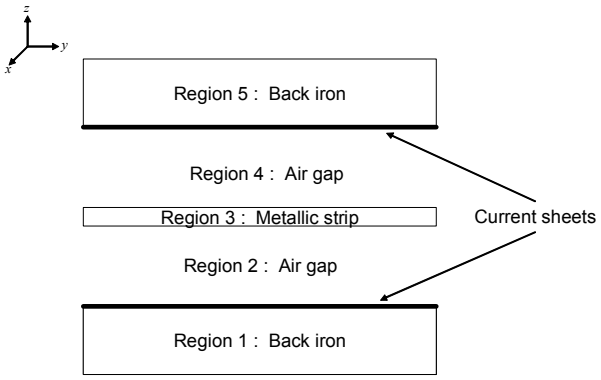

Fig. 2. General outline of a double sided induction heating system.

In the following sections, the theoretical analysis for three phase and single phase excitations are derived.

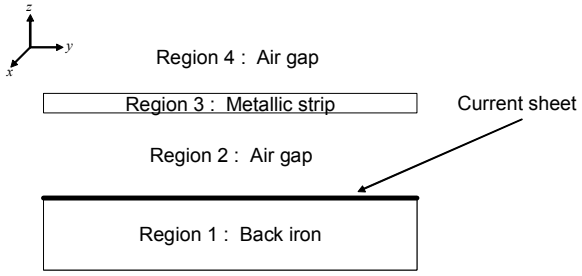

Fig. 3. General outline of a single sided induction heating system.

III. THEORETICAL ANALYSIS

It is assumed that the winding produces a perfect sinusoidal traveling wave. The line current density may be represented as

$$J = \mathrm{Re}\left[J' \exp\left\{ j(\omega t - ky) \right\} \right],$$

where J', ω and k are the amplitude of line

current density, angular frequency and wavelength factor respectively where the latter is related to the pole pitch τ by

$$k = \pi / \tau.$$

A. Field theory solution

The field produced will link all regions from *1* to *N*. Maxwell's equations are solved accordingly to yield (for regions $1 < n < N$)

$$\begin{bmatrix} B_{z,n} \\ H_{y,n} \end{bmatrix} = [T_n] \cdot \begin{bmatrix} B_{z,n-1} \\ H_{y,n-1} \end{bmatrix}, \tag{1}$$

where $B_{z,n}$ and $H_{y,n}$ are the field components at the outer boundary of region n and $B_{y,n-1}$ and $H_{z,n-1}$ are the equivalent values at the inner boundary of the same region and $[T_n]$ is the associated transfer matrix which is given by

$$[T_n] = \begin{bmatrix} \cosh(\alpha_n S_n) & \dfrac{\sinh(\alpha_n S_n)}{\beta_n} \\ \beta_n \sinh(\alpha_n S_n) & \cosh(\alpha_n S_n) \end{bmatrix}, \tag{2}$$

where S_n and α_n are the thickness and attenuation constant of region n, and

$$\beta_n = \frac{\alpha_n}{j\mu_0\mu_n k}.$$

Hence given the values of B_z and H_y at the lower boundary of a region, the values of B_z and H_y at the outer boundary are immediately obtainable from this simple transfer matrix relation. At the boundaries where no excitation current sheet exists, B_z and H_y are continuous; thus for example, if two regions are considered with no current sheet at the common boundary, knowing $B_{z,n}$ and $H_{y,n}$, the lower boundary of the first region, B_z and H_y at the upper boundary of the second region can be calculated by successive use of the underlying two transfer matrices. Considering the current sheet to be at $z = g$, then

$$H'_{y,n} = H_{y,n} \qquad , n \neq r,$$

and

$$H'_{y,n} = H_{y,n} - J' \quad , n = r, \tag{3}$$

where $H_{y,n}$ is the axial magnetic field strength in close lower proximity to the boundary and $H'_{y,n}$ is the axial magnetic field strength in close upper proximity to the boundary.

Given the current sheet excitation at $z = g_r$, the overall structure divides into an upper part, which is modeled according to

$$\begin{bmatrix} B_{z,n-1} \\ H_{y,n-1} \end{bmatrix} = [T_{n-1}] \cdot [T_{n-2}] \cdots [T_{r+1}] \cdot \begin{bmatrix} B_{Z,r} \\ H_{y,r} - J' \end{bmatrix}, \tag{4}$$

and a lower part which supports the following relation

$$\begin{bmatrix} B_{z,r} \\ H_{y,r} \end{bmatrix} = [T_r] \cdot [T_{r-1}] \cdots [T_2] \cdot \begin{bmatrix} B_{z,1} \\ H_{y,1} \end{bmatrix}. \tag{5}$$

Enough information is now available to find all field components; hence, the equivalent circuit model can be set up using the surface impedances of the regions under consideration.

B. Surface impedance calculations

Looking outwards from the current sheet, the surface impedance at a boundary of $z = g$ is defined as [14]

$$Z_{n+1} = \frac{E_{x,n}}{H_{y,n}} = -\frac{\omega}{k} \cdot \frac{B_{z,n}}{H_{y,n}}. \tag{6}$$

And the surface impedance looking inwards is defined as

$$Z_n = -\frac{E_{x,n}}{H_{y,n}} = \frac{\omega}{k} \cdot \frac{B_{z,n}}{H_{y,n}}. \tag{7}$$

Using the method obtained in [14] with the values of $B_{z,N-1}$, $H_{y,N-1}$, B_{z1}, H_{y1} and $[T_n]$ as derived in the previous section then

$$Z_{in} = \frac{Z_r Z_{r+1}}{Z_r + Z_{r+1}}, \tag{8}$$

where Z_{in} is the input surface impedance at the

current sheet and Z_{g+1} and Z_g are the surface impedances looking outwards and inwards at the current sheet. Substituting for Z_r and Z_{r+1} using (7) and (6), respectively, and rearranging the terms yields

$$Z_{in} = -\frac{E_{x,r}}{H_{y,r} - H'_{y,r}}. \quad (9)$$

Substituting (3) into (9) yields

$$Z_{in} = \frac{E_{x,r}}{J'}. \quad (10)$$

From this, the input surface impedance at the current sheet can be determined. All the field components can be found by a straightforward use of this and (7), (4) and (5).

Having found E_x, B_z and H_y at all boundaries, it is then a simple matter to calculate the power entering a region through the concept of the Poynting vector. The time-average power density passing through a surface is usually given as

$$P = \frac{1}{2}\mathrm{Re}\{\bar{E} \times \bar{H}^*\} \quad \mathrm{W}/m^2.$$

Hence the time average power density flowing upwards from the current sheet at $z = g_r$ is given by

$$P'_{in,r} = \frac{1}{2}\mathrm{Re}\left\{E_{x,r} H'^{\,*}_{y,r}\right\},$$

and the time average power density flowing downwards from the current sheet at $z = g_r$ is given by

$$P_{in,r} = -\frac{1}{2}\mathrm{Re}\left\{E_{x,r} H^{*}_{y,r}\right\}.$$

The net power density in a region is the difference between the power in and power out, where

$$P_{in} = -\frac{\omega}{2k}\mathrm{Re}\left\{B_{z,r} H'^{\,*}_{y,r} - B_{z,r} H_{y,r}\right\}. \quad (11)$$

It follows that the tangential force density $F_{y,}$ acting on the strip, is the net power density induced divided by traveling wave velocity $2\tau f$ [15]

$$F_y = \frac{P_{in}}{\lambda f} \quad \mathrm{N}/m^2, \quad (12)$$

where f is the operating frequency.

As the transfer matrix formalism is strictly rooted in the analytical field solutions, the presented formalism might be regarded as sufficient in itself. However, from the technical view point it is hardly possible to draw a clear picture that refers to any of the intended functionalities. Engineers, for the most part, prefer to think in terms of an equivalent circuit model rather than to refer to full-wave time varying field analysis. In addition, the impact of altering design parameters is easier to grasp than in the framework of an applied electromagnetics analysis. For this reason an equivalent circuit model has been developed in the following section.

C. The micro-T terminal equivalent circuit

The underlying transmission-line form of (3)-(5) suggests that, by analogy, some form of equivalent circuit is possible [15]. No loss of generality occurs if only one region is considered. The electric and magnetic field quantities are linked as shown in (1) and by making use of the relation

$$E_x = -\frac{\omega}{k} \cdot B_z.$$

In order to represent the relationship between E_n, H_n and E_{n-1}, H_{n-1} by a corresponding T-circuit, a change of variable is required. Without such a transformation it does not appear to be possible to represent a region with such a simple 3-element circuit. Engineers prefer to think in terms of an equivalent circuit rather than time varying field problem as represented in [20, 21]. A practical variable transformation refers to the variable *E*, which is changed to *wE,* where *w* is the width of the strip.

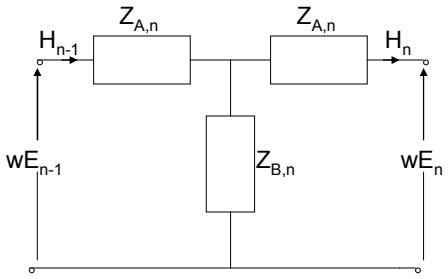

Fig. 4. Basic T-circuit for region *n*.

A T-circuit can now be used to link the variables *wE* and *H* on either side of a region as shown in Fig. 4.

In effect, the current H_n in a T-circuit is driven by a voltage wE_n. For the general region *n*, the impedances are given by the following relations [17]

$$Z_{A,n} = Z_n' \tanh(\frac{\alpha_n S_n}{2}) \tag{13}$$

$$Z_{B,n} = \frac{Z_n'}{\sinh(\alpha_n S_n)}, \tag{14}$$

where Z_n' is the characteristic impedance of region *n* and is defined by the relation

$$Z_n' = \frac{j\omega\mu_0\mu_n}{\alpha_n}, \tag{15}$$

where μ_n is the relative permeability of region n. The attenuation constant α_n is defined by

$$\alpha_n = (k^2 + j\omega\sigma_n\mu_0\mu_n)^{\frac{1}{2}},$$

where σ_n is the conductivity of region n.

As a check, if this circuit is loaded with an impedance Z_{n+1}, the input impedance is Z_n as given in (7). Regions *2* to *N-1* in the general case could all be replaced by such circuits. Regions *1* and *N* would simply require a single impedance which is the characteristic impedance of the respective region as in (15).

On joining the T-circuits in cascade, the full basic equivalent circuit for the single sided traveling wave induction heating system is obtained as shown in Fig. 5.

For DSIH systems, the full basic equivalent circuit is shown in Fig. 6.

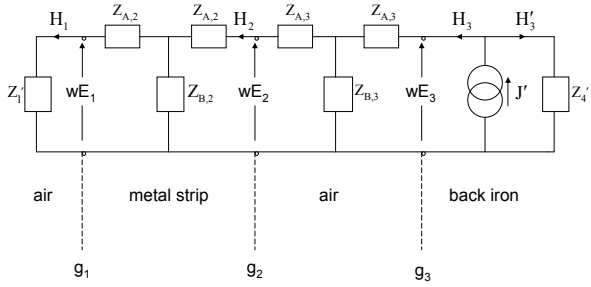

Fig. 5. Basic equivalent circuit for a single sided induction heating system.

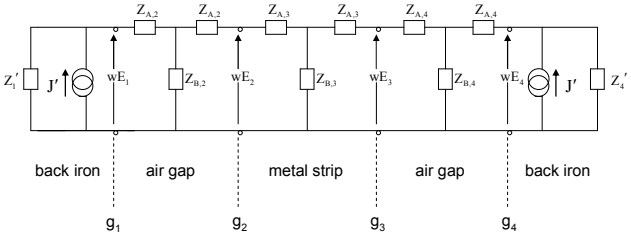

Fig. 6. Basic equivalent circuit for a double sided induction heating system.

Thus an equivalent circuit has been derived by a rearrangement of the field solution, where the voltages and currents are directly related to the field quantities.

It is convenient to think in terms of phase voltages and currents. The input quantities to the basic equivalent circuit are the current J' and the voltage wE_r. The relation between J' and the r.m.s. phase current *I* can be written as

$$J' = \frac{6\sqrt{2}N_{eff}I}{\tau p},$$

where *p* is the number of poles and N_{eff} stands for the effective number of series turns per phase, hence

$$I = (I_{fac})J', \tag{16}$$

where

$$I_{fac} = \frac{\tau p}{6\sqrt{2}N_{eff}},$$

The phase voltage is linked to wE_r by

$$V = \sqrt{2}N_{eff}wE_r, \quad (17)$$

therefore,

$$V = V_{fac}wE_r, \quad (18)$$

where

$$V_{fac} = \sqrt{2}N_{eff}.$$

Let us now consider the effect of multiplying the quantities wE_n and H_n terms in the basic equivalent circuit by the factors V_{fac} and I_{fac} respectively then, the impedances in the basic circuit have to be multiplied by an impedance factor given by

$$Z_{fac} = \frac{V_{fac}}{I_{fac}} = \frac{12(N_{eff})^2}{\tau p}, \quad (19)$$

and the terminal impedance of the induction heating system is given by

$$Z_t = Z_{fac}wZ_{in} \quad \Omega. \quad (20)$$

This relation results in a completely new equivalent circuit in which the input quantities are the r.m.s voltage and r.m.s. current using (18) and (16). Thus the various voltages and currents at the input to each T-circuit are now related directly to the field quantities at the corresponding interfaces of the induction heating system and this terminal equivalent circuit has all the advantages of the basic circuit but, in addition, the impedances are real impedances.

IV. NUMERICAL RESULTS

The equivalent circuit method that has been described in the previous section is validated through a numerical example. Reference [7] employed a double sided induction heating system whose data are given in Table 1. Five regions are required to simulate a double sided system, therefore three T-circuits are combined together and terminated by characteristic impedances of outer regions which are the backing iron regions as shown in Fig. 3.

For comparison reasons, FEM computation is adopted in our analysis which is widely used as a numerical technique for this kind of applications.

In our implementation, the field domain is divided into a number of regions, each being defined by its coordinates, permeability and conductivity. Each region is descritized using first order triangular elements [22]. The induced power in the charge is obtained through the solution of governing differential equation for each nodal magnetic vector potential. Three values of power are computed: the power integrated over the coil, the air gap power and the power integrated over the charge.

Table 1. Problem data for traveling wave dish and ssih systems [9].

Strip thickness, (mm)	2
Strip width, (mm)	1000
Strip length, (mm)	960
Relative permeability of strip	1
Mean strip conductivity, (S/m)	3.03×10^7
Axial pole pitch, (mm)	480
Slot pitch, (mm)	160
Slot width, (mm)	80
Slot depth, (mm)	40
Slots per pole per phase	1
Number of axial poles	2
Number of conductors per slot	8
Frequency, (Hz)	50
Inductor axial length, (mm)	960
Inductor width, (mm)	1000
Magnetic yoke depth, (mm)	80
Air gap length between yoke & strip, (mm)	15
Amplitude of line current density, (kA/m)	200
Input phase voltage, (V)	220

The solution is assumed to be convergent when these three values do not differ by more than 1% which is termed as the power mismatch or power

imbalance.

For the sake of comparison, the same model is adopted as a single sided induction heating system using the same line current density by removing one of the inductors along with its backing iron. Four regions are required to simulate a single sided system therefore two T-circuits are combined together and terminated by characteristic impedances of outer regions which are the backing iron region and outer air region as shown in fig.4.

Table 2 shows the computed parameters for both systems using FEM and the micro-T circuit model. Results obtained using both methods are in good agreement as shown in Table 2. This agreement is attributed to the fact that strip thickness is very small compared to strip length and width which coincides with the assumptions made in the mathematical model.

Table 2. Computed parameters for traveling wave induction heating systems.

Parameter	FEM value	Layer Theory value
Per phase DSIH strip resistance (Ω)	0.0497	0.0513
Per phase DSIH reactance (Ω)	0.014	0.017
DSIH strip power (kW)	1210.3	1250.2
DSIH axial force (N)	23914.5	26045.3
Per phase SSIH strip resistance (Ω)		0.0125
0.012		
Per phase SSIH reactance (Ω)	0.0087	0.0086
SSIH strip power (kW)	305.06	292.8
SSIH axial force (N)	6300	6099.9

Figures 7 and 8 show respectively the variation of normal and tangential (axial) flux density components (B_z, B_y) along magnetic gap length. The maximum deviation between the results of both methods is found to be 5.2%.

Figures 9 and 10 show the variation of normal and tangential (axial) flux density components (B_z, B_y) along distance normal to the strip. Again both methods correlate well within 4%. In both systems, the axial flux density component in the air gap is greater than the normal component, this may be attributed to the fact that the pole pitch is much greater than the air gap length in both systems and in this case these systems are considered as axial flux machines. It is clear from these figures that the axial component of magnetic flux density is decreased within the strip due to skin effect which is not effectively pronounced in the normal component to the strip.

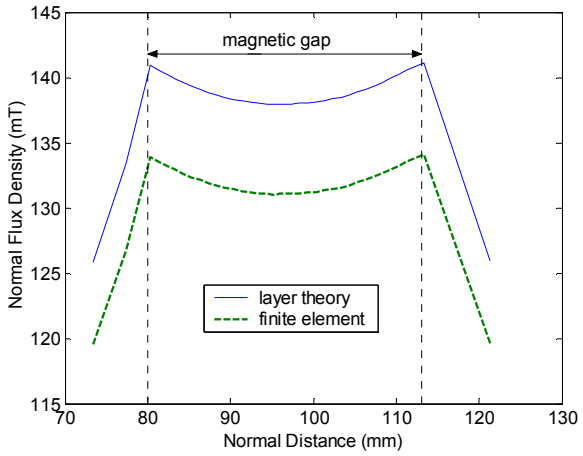

Fig. 7. Variation of normal flux density component along normal distance to strip for double sided induction heating system.

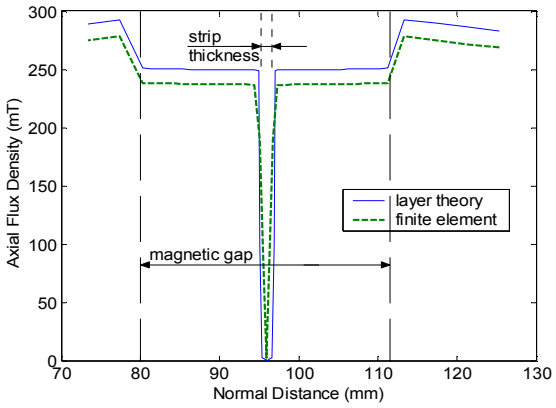

Fig. 8. Variation of axial flux density component along normal distance to strip for double sided induction heating system.

It should be appreciated that comparisons of computed field values in multilayer simulation problem of electrical machines with real field data are found in literature [18, 23].

V. CONCLUSION

The micro-T circuit has been used for the analysis of single and double sided traveling wave induction heating systems. It can be used for any number of regions, and with any number of poles. Using such circuits may provide a better technical

insight into the system than is possible from studying the full-wave solutions from a computational electromagnetics analysis.

Given just the voltages and currents in the terminal equivalent circuit, the field quantities at any region boundary can be easily derived. The obtained results agree well with the data from the corresponding FEM analysis.

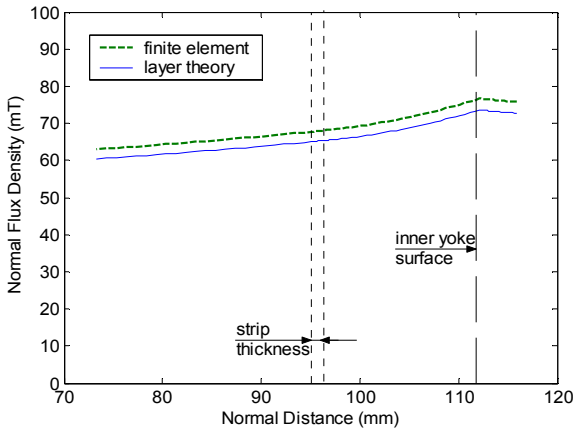

Fig. 9. Variation of normal flux density component along normal distance to strip for single sided induction heating system.

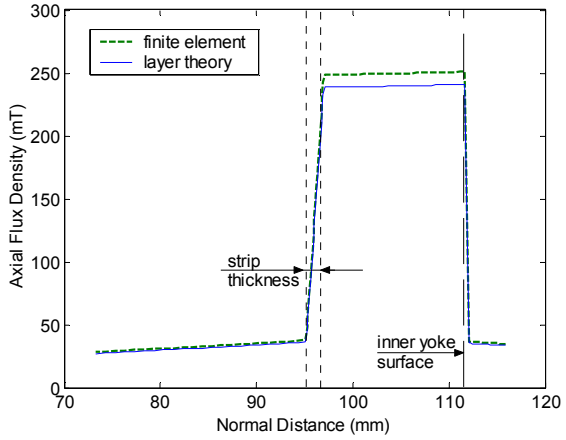

Fig. 10. Variation of axial flux density component along normal distance to strip for single sided induction heating system.

ACKNOWLEDGMENT

The author is deeply indebted to Professor Daniel Erni, his host and co-worker at the University of Duisburg-Essen for advice and encouragement. This work was supported in part by the DAAD under Grant A0901170.

REFERENCES

[1] W. Jackson, “Analysis of edge effects in traveling wave inductors heating metal products,” *Proc. Of NCE-UIC Electroheat for Metals Conf.*, vol. 5, no. 3, 1982.

[2] S. Lupi, M. Forzan, F. Dughiero, and A. Zenkov, “Comparison of edge-effects of transverse flux and traveling wave induction heating inductors,” *IEEE Trans. Magn.,* vol. 35, no. 5, pp. 3556-58, 1999.

[3] L. Pang, Y. Wang, and T. Chen, “Analysis of eddy current density distribution in slotless traveling wave inductor,” *Proc. ICEMS*, pp. 2865-68, 1998.

[4] J. Wang, J. Li, Y. Wang, and X. Yang, “Simulation of traveling wave induction heating systems,” *Proc. WAC World Automation Conf.*, pp. 1-4, 2008.

[5] V. Bukanin, F. Dughiero, S. Lupi and V. Nemkov, "Simulation and design problems of multiphase induction heating systems", *Proc. 37th Int. Wiss Kolloquium,* pp. 588-593, 1992**.**

[6] V. Vadher, "Theory and design of traveling wave induction heaters," *Proc. BNCE-UIE Electroheat for Metals Conf.*, vol. 5, no. 1, 1982.

[7] F. Dughiero, S. Lupi, V. Nemkov, and P. Siega, “Traveling wave inductors for the continuous induction heating of metal strips,” *Proc. Mediterranean Electrotechnical Conf.*, pp. 1154-1157, 1994.

[8] L. Pang, Y. Wang, and T. Chen, “Analysis of eddy current density distribution in slotless traveling wave inductor,” *Proc. ICEMS*, pp. 2865-68, 1998.

[9] Y. Wang and J. Wang, “The study of two novel induction heating technology,” *Proc. ICEMS, conf.*, pp. 572-574, 2008.

[10] S. Ho, J. Wang, W. Fu, and Y. Wang, “A novel crossed traveling wave induction heating system and finite element analysis of eddy current and temperature distributions,” *IEEE*

Trans. Magn., vol. 45, no.10, pp. 4777-80, 2009.

[11] A. Ali, V. Bukanin, F. Dughiero, S. Lupi, V. Nemkov, and P. Siega, "Simulation of multiphase induction heating systems," *Proc. Computation in Electromagnetics International conf.,* pp. 211-214, 1994.

[12] F. Dughiero, S. Lupi, and P. Siega, "Analytical calculation of traveling wave induction heating systems," *Proc. International Symposium on Electromagnetic Fields in Electrical Engineering*, pp. 207-210, 1993.

[13] V. Vadher and I. Smith, "Traveling wave induction heaters with compensating windings," *Proc. International Symposium on Electromagnetic Fields in Electrical Engineering*, pp. 211-214, 1993.

[14] L. Bunni and K. Altaii, "The layer theory approach applied to induction heating systems with rotational symmetry," *Proc. IEEE Southeast Conf.*, pp. 413-420, 2007.

[15] J. Greig and E. M. Freeman, "Traveling wave problem in electrical machine," *Proc. IEE*, vol. 114, no. 11, pp. 1681-1683, 1967.

[16] E. M. Freeman, "Traveling waves in induction machines: input impedance and equivalent circuits," *Proc. IEE*, vol. 115, no. 12, pp. 1772-1776, Dec. 1968.

[17] E. M. Freeman and B. E. Smith, "Surface impedance method applied to multilayer cylindrical induction devices with circumferential exciting currents," *Proc. IEE*, vol. 117, no. 10, pp. 2012-2013, Oct. 1970.

[18] J. F. Eastham and J. H. Alwash, "Transverse flux tubular motors," *Proc. IEE*., vol. 112, no. 12, pp. 1709-1718, 1972.

[19] J. H. Alwash, A. D. Mohssen, and A. S. Abdi, "Helical motion tubular induction motor," *IEEE Trans. Energy Convers.,* vol. 18, no. 3, pp. 362 – 396, 2003.

[20] E. M. Freeman, "Equivalent circuits from electromagnetic theory: low frequency induction devices," *Proc. IEE*, vol. 121, no. 10, pp. 1117-1121, 1974.

[21] E. M. Freeman and T. G. Bland, "Equivalent circuit of concentric cylindrical conductors in an axial alternating magnetic field," *Proc. IEE*, vol. 123, no. 2, pp. 149-152, 1976.

[22] P. P. Silvester, and R. L. Ferrari, *Finite Elements for Electrical Engineers,* 3rd edition, Cambridge University Press, 1996.

[23] J. H. Alwash, *Analysis and Design of Linear Induction Machines*, Ph.D. thesis, Imperial College, University of London, U.K., 1972.

L. J. B. Qaseer was born in Baghdad, Iraq, on October 14, 1957**.** H**e** received his B.Sc., M. Sc. and Ph.D. degrees from the University of Baghdad in 1979, 1993 and 2004 respectively, all in electrical engineering. In 2005, he was with the Mechatronic Engineering Department at the University of Baghdad. Dr. Qaseer is currently with the General & Theoretical Electrical Engineering Department of the University of Duisburg-Essen, Duisburg, Germany. His special fields of interest include rotary, linear, tubular linear and helical motion induction motors, as well as induction heating.

Corrections to "A Simplified Model for Normal Mode Helical Antennas"

Changyi Su [1], Haixin Ke [2], and Todd Hubing [1]
[1] Department of Electrical and Computer Engineering
Clemson University, SC 29634-3001, USA
csu@clemson.edu, hubing@clemson.edu

[2] Department of Biomedical Engineering
Washington University in St. Louis, MO 63130, USA
keh@seas.wustl.edu

In Section III of the above paper[1], there is a typographical error in the caption of Figure 3 (c): *input reactance* should read *input resistance*.

Figure 6(a) did not appear in print the way the author intended. The correct figure appears here.

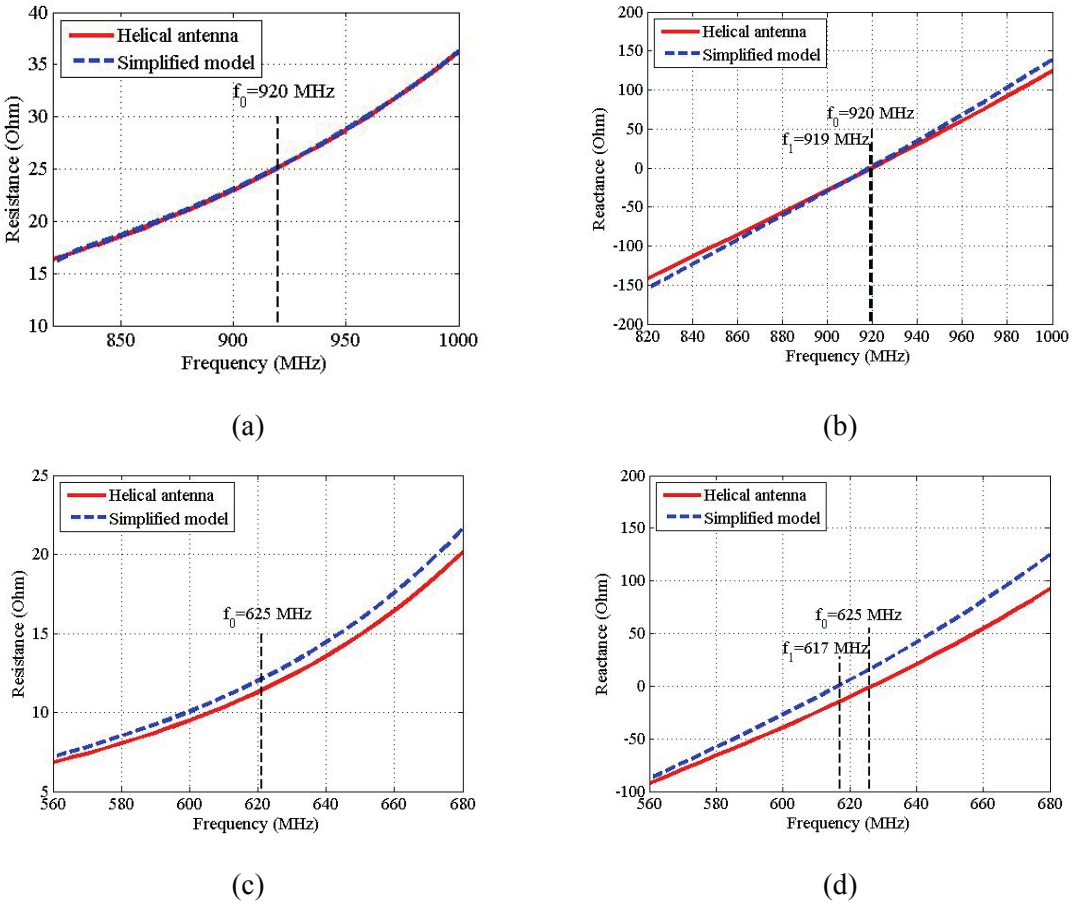

Fig. 6. Input impedance of the RFID antenna and its simplified model: (a) Input resistance in air (b) Input reactance in air (c) Input resistance in dielectric (d) Input reactance in dielectric.

Finally, there is a typographical error on page 39: *10 x 4.8 x 1.67 mm* should read *10 x 4.8 x 1.67 cm*.

[1]C. Su, H. Ke and T. Hubing, "A simplified model for normal mode helical antennas," *Journal of the Applied Computational Electromagnetics Society*, vol. 25, no. 1, pp. 32-40, Jan. 2010.

2010 INSTITUTIONAL MEMBERS

DTIC-OCP LIBRARY
8725 John J. Kingman Rd, Ste 0944
Fort Belvoir, VA 22060-6218

AUSTRALIAN DEFENCE LIBRARY
Northcott Drive
Canberra, A.C.T. 2600 Australia

BEIJING BOOK CO, INC
701 E Linden Avenue
Linden, NJ 07036-2495

BUCKNELL UNIVERSITY
69 Coleman Hall Road
Lewisburg, PA 17837

ROBERT J. BURKHOLDER
OHIO STATE UNIVERSITY
1320 Kinnear Road
Columbus, OH 43212

DARTMOUTH COLLEGE
6025 Baker/Berry Library
Hanover, NH 03755-3560

DSTO EDINBURGH
AU/33851-AP, PO Box 830470
Birmingham, AL 35283

SIMEON J. EARL – BAE SYSTEMS
W432A, Warton Aerodome
Preston, Lancs., UK PR4 1AX

ELLEDIEMME
Libri Dal Mondo
PO Box 69/Poste S. Silvestro
Rome, Italy 00187

ENGINEERING INFORMATION, INC
PO Box 543
Amsterdam, Netherlands 1000 Am

ETSE TELECOMUNICACION
Biblioteca, Campus Lagoas
Vigo, 36200 Spain

OLA FORSLUND
SAAB MICROWAVE SYSTEMS
Nettovagen 6
Jarfalla, Sweden SE-17588

GEORGIA TECH LIBRARY
225 North Avenue, NW
Atlanta, GA 30332-0001

HRL LABS, RESEARCH LIBRARY
3011 Malibu Canyon
Malibu, CA 90265

IEE INSPEC
Michael Faraday House
6 Hills Way
Stevenage, Herts UK SG1 2AY

IND CANTABRIA
PO Box 830470
Birmingham, AL 35283

INSTITUTE FOR SCIENTIFIC INFO.
Publication Processing Dept.
3501 Market St.
Philadelphia, PA 19104-3302

KUWAIT UNIVERSITY
Postfach/po box 432
Basel, Switzerland 4900

LIBRARY – DRDC OTTAWA
3701 Carling Avenue
Ottawa, Ontario, Canada K1A OZ4

LIBRARY of CONGRESS
Reg. Of Copyrights
Attn: 407 Deposits
Washington DC, 20559

LINDA HALL LIBRARY
5109 Cherry Street
Kansas City, MO 64110-2498

RAY MCKENZIE – TELESTRA
13/242 Exhibition Street
Melbourne, Vic, Australia 3000

MISSISSIPPI STATE UNIV LIBRARY
PO Box 9570
Mississippi State, MS 39762

MISSOURI S&T
400 W 14th Street
Rolla, MO 56409

MIT LINCOLN LABORATORY
Periodicals Library
244 Wood Street
Lexington, MA 02420

OSAMA MOHAMMED
FLORIDA INTERNATIONAL UNIV
10555 W Flagler Street
Miami, FL 33174

NAVAL POSTGRADUATE SCHOOL
Attn:J. Rozdal/411 Dyer Rd./ Rm 111
Monterey, CA 93943-5101

NDL KAGAKU
C/0 KWE-ACCESS
PO Box 300613 (JFK A/P)
Jamaica, NY 11430-0613

OVIEDO LIBRARY
PO BOX 830679
Birmingham, AL 35283

PENN STATE UNIVERSITY
126 Paterno Library
University Park, PA 16802-1808

DAVID J. PINION
1122 E PIKE STREET #1217
SEATTLE, WA 98122

KATHERINE SIAKAVARA-
ARISTOTLE UNIV OF
THESSALONIKI
Gymnasiou 8
Thessaloniki, Greece 55236

SWETS INFORMATION SERVICES
160 Ninth Avenue, Suite A
Runnemede, NJ 08078

TIB & UNIV. BIB. HANNOVER
DE/5100/G1/0001
Welfengarten 1B
Hannover, Germany 30167

UNIV OF CENTRAL FLORIDA
4000 Central Florida Boulevard
Orlando, FL 32816-8005

UNIVERSITY OF COLORADO
1720 Pleasant Street, 184 UCB
Boulder, CO 80309-0184

UNIVERSITY OF KANSAS –
WATSON
1425 Jayhawk Blvd 210S
Lawrence, KS 66045-7594

UNIVERSITY OF MISSISSIPPI
JD Williams Library
University, MS 38677-1848

UNIVERSITY LIBRARY/HKUST
CLEAR WATER BAY ROAD
KOWLOON, HONG KONG

UNIV POLIT CARTAGENA
Serv Btca Univ,
Paseo Alfonso XIII, 48
Cartagena, Spain 30203

THOMAS WEILAND
TU DARMSTADT
Schlossgartenstrasse 8
Darmstadt, Hessen, Germany 64289

STEVEN WEISS
US ARMY RESEARCH LAB
2800 Powder Mill Road
Adelphi, MD 20783

YOSHIHIDE YAMADA
NATIONAL DEFENSE ACADEMY
1-10-20 Hashirimizu
Yokosuka, Kanagawa,
Japan 239-8686

ACES COPYRIGHT FORM

This form is intended for original, previously unpublished manuscripts submitted to ACES periodicals and conference publications. The signed form, appropriately completed, MUST ACCOMPANY any paper in order to be published by ACES. PLEASE READ REVERSE SIDE OF THIS FORM FOR FURTHER DETAILS.

TITLE OF PAPER:

AUTHORS(S)

PUBLICATION TITLE/DATE:

RETURN FORM TO:

Dr. Atef Z. Elsherbeni
University of Mississippi
Dept. of Electrical Engineering
Anderson Hall Box 13
University, MS 38677 USA

PART A - COPYRIGHT TRANSFER FORM

(NOTE: Company or other forms may not be substituted for this form. U.S. Government employees whose work is not subject to copyright may so certify by signing Part B below. Authors whose work is subject to Crown Copyright may sign Part C overleaf).

The undersigned, desiring to publish the above paper in a publication of ACES, hereby transfer their copyrights in the above paper to The Applied Computational Electromagnetics Society (ACES). The undersigned hereby represents and warrants that the paper is original and that he/she is the author of the paper or otherwise has the power and authority to make and execute this assignment.

Returned Rights: In return for these rights, ACES hereby grants to the above authors, and the employers for whom the work was performed, royalty-free permission to:

1. Retain all proprietary rights other than copyright, such as patent rights.
2. Reuse all or portions of the above paper in other works.
3. Reproduce, or have reproduced, the above paper for the author's personal use or for internal company use provided that (a) the source and ACES copyright are indicated, (b) the copies are not used in a way that implies ACES endorsement of a product or service of an employer, and (c) the copies per se are not offered for sale.
4. Make limited distribution of all or portions of the above paper prior to publication.
5. In the case of work performed under U.S. Government contract, ACES grants the U.S. Government royalty-free permission to reproduce all or portions of the above paper, and to authorize others to do so, for U.S. Government purposes only.

ACES Obligations: In exercising its rights under copyright, ACES will make all reasonable efforts to act in the interests of the authors and employers as well as in its own interest. In particular, ACES REQUIRES that:

1. The consent of the first-named author be sought as a condition in granting re-publication permission to others.
2. The consent of the undersigned employer be obtained as a condition in granting permission to others to reuse all or portions of the paper for promotion or marketing purposes.

In the event the above paper is not accepted and published by ACES or is withdrawn by the author(s) before acceptance by ACES, this agreement becomes null and void.

AUTHORIZED SIGNATURE — TITLE (IF NOT AUTHOR)

EMPLOYER FOR WHOM WORK WAS PERFORMED — DATE FORM SIGNED

Part B - U.S. GOVERNMENT EMPLOYEE CERTIFICATION

(NOTE: if your work was performed under Government contract but you are not a Government employee, sign transfer form above and see item 5 under Returned Rights).

This certifies that all authors of the above paper are employees of the U.S. Government and performed this work as part of their employment and that the paper is therefor not subject to U.S. copyright protection.

AUTHORIZED SIGNATURE — TITLE (IF NOT AUTHOR)

NAME OF GOVERNMENT ORGANIZATION — DATE FORM SIGNED

PART C - CROWN COPYRIGHT

(NOTE: ACES recognizes and will honor Crown Copyright as it does U.S. Copyright. It is understood that, in asserting Crown Copyright, ACES in no way diminishes its rights as publisher. Sign only if *ALL* authors are subject to Crown Copyright).

This certifies that all authors of the above Paper are subject to Crown Copyright. (Appropriate documentation and instructions regarding form of Crown Copyright notice may be attached).

AUTHORIZED SIGNATURE TITLE OF SIGNEE

NAME OF GOVERNMENT BRANCH DATE FORM SIGNED

Information to Authors

ACES POLICY

ACES distributes its technical publications throughout the world, and it may be necessary to translate and abstract its publications, and articles contained therein, for inclusion in various compendiums and similar publications, etc. When an article is submitted for publication by ACES, acceptance of the article implies that ACES has the rights to do all of the things it normally does with such an article.

In connection with its publishing activities, it is the policy of ACES to own the copyrights in its technical publications, and to the contributions contained therein, in order to protect the interests of ACES, its authors and their employers, and at the same time to facilitate the appropriate re-use of this material by others.

The new United States copyright law requires that the transfer of copyrights in each contribution from the author to ACES be confirmed in writing. It is therefore necessary that you execute either Part A-Copyright Transfer Form or Part B-U.S. Government Employee Certification or Part C-Crown Copyright on this sheet and return it to the Managing Editor (or person who supplied this sheet) as promptly as possible.

CLEARANCE OF PAPERS

ACES must of necessity assume that materials presented at its meetings or submitted to its publications is properly available for general dissemination to the audiences these activities are organized to serve. It is the responsibility of the authors, not ACES, to determine whether disclosure of their material requires the prior consent of other parties and if so, to obtain it. Furthermore, ACES must assume that, if an author uses within his/her article previously published and/or copyrighted material that permission has been obtained for such use and that any required credit lines, copyright notices, etc. are duly noted.

AUTHOR/COMPANY RIGHTS

If you are employed and you prepared your paper as a part of your job, the rights to your paper initially rest with your employer. In that case, when you sign the copyright form, we assume you are authorized to do so by your employer and that your employer has consented to all of the terms and conditions of this form. If not, it should be signed by someone so authorized.

NOTE RE RETURNED RIGHTS: Just as ACES now requires a signed copyright transfer form in order to do "business as usual", it is the intent of this form to return rights to the author and employer so that they too may do "business as usual". If further clarification is required, please contact: The Managing Editor, R. W. Adler, Naval Postgraduate School, Code EC/AB, Monterey, CA, 93943, USA (408)656-2352.

Please note that, although authors are permitted to re-use all or portions of their ACES copyrighted material in other works, this does not include granting third party requests for reprinting, republishing, or other types of re-use.

JOINT AUTHORSHIP

For jointly authored papers, only one signature is required, but we assume all authors have been advised and have consented to the terms of this form.

U.S. GOVERNMENT EMPLOYEES

Authors who are U.S. Government employees are not required to sign the Copyright Transfer Form (Part A), but any co-authors outside the Government are.

Part B of the form is to be used instead of Part A only if all authors are U.S. Government employees and prepared the paper as part of their job.

NOTE RE GOVERNMENT CONTRACT WORK: Authors whose work was performed under a U.S. Government contract but who are not Government employees are required so sign Part A-Copyright Transfer Form. However, item 5 of the form returns reproduction rights to the U. S. Government when required, even though ACES copyright policy is in effect with respect to the reuse of material by the general public.

APPLIED COMPUTATIONAL ELECTROMAGNETICS SOCIETY JOURNAL
http://aces.ee.olemiss.edu

INFORMATION FOR AUTHORS

PUBLICATION CRITERIA

Each paper is required to manifest some relation to applied computational electromagnetics. **Papers may address general issues in applied computational electromagnetics, or they may focus on specific applications, techniques, codes, or computational issues.** While the following list is not exhaustive, each paper will generally relate to at least one of these areas:

1. **Code validation.** This is done using internal checks or experimental, analytical or other computational data. Measured data of potential utility to code validation efforts will also be considered for publication.

2. **Code performance analysis.** This usually involves identification of numerical accuracy or other limitations, solution convergence, numerical and physical modeling error, and parameter tradeoffs. However, it is also permissible to address issues such as ease-of-use, set-up time, run time, special outputs, or other special features.

3. **Computational studies of basic physics.** This involves using a code, algorithm, or computational technique to simulate reality in such a way that better, or new physical insight or understanding, is achieved.

4. **New computational techniques** or new applications for existing computational techniques or codes.

5. **"Tricks of the trade"** in selecting and applying codes and techniques.

6. **New codes, algorithms, code enhancement, and code fixes.** This category is self-explanatory, but includes significant changes to existing codes, such as applicability extensions, algorithm optimization, problem correction, limitation removal, or other performance improvement. **Note: Code (or algorithm) capability descriptions are not acceptable, unless they contain sufficient technical material to justify consideration.**

7. **Code input/output issues.** This normally involves innovations in input (such as input geometry standardization, automatic mesh generation, or computer-aided design) or in output (whether it be tabular, graphical, statistical, Fourier-transformed, or otherwise signal-processed). Material dealing with input/output database management, output interpretation, or other input/output issues will also be considered for publication.

8. **Computer hardware issues.** This is the category for analysis of hardware capabilities and limitations of various types of electromagnetics computational requirements. Vector and parallel computational techniques and implementation are of particular interest.

Applications of interest include, but are not limited to, antennas (and their electromagnetic environments), networks, static fields, radar cross section, inverse scattering, shielding, radiation hazards, biological effects, biomedical applications, electromagnetic pulse (EMP), electromagnetic interference (EMI), electromagnetic compatibility (EMC), power transmission, charge transport, dielectric, magnetic and nonlinear materials, microwave components, MEMS, RFID, and MMIC technologies, remote sensing and geometrical and physical optics, radar and communications systems, sensors, fiber optics, plasmas, particle accelerators, generators and motors, electromagnetic wave propagation, non-destructive evaluation, eddy currents, and inverse scattering.

Techniques of interest include but not limited to frequency-domain and time-domain techniques, integral equation and differential equation techniques, diffraction theories, physical and geometrical optics, method of moments, finite differences and finite element techniques, transmission line method, modal expansions, perturbation methods, and hybrid methods.

Where possible and appropriate, authors are required to provide statements of quantitative accuracy for measured and/or computed data. This issue is discussed in "Accuracy & Publication: Requiring, quantitative accuracy statements to accompany data," by E. K. Miller, *ACES Newsletter,* Vol. 9, No. 3, pp. 23-29, 1994, ISBN 1056-9170.

SUBMITTAL PROCEDURE

All submissions should be uploaded to ACES server through ACES web site (http://aces.ee.olemiss.edu) by using the upload button, journal section. Only pdf files are accepted for submission. The file size should not be larger than 5MB, otherwise permission from the Editor-in-Chief should be obtained first. Automated acknowledgment of the electronic submission, after the upload process is successfully completed, will be sent to the corresponding author only. It is the responsibility of the corresponding author to keep the remaining authors, if applicable, informed. Email submission is not accepted and will not be processed.

PAPER FORMAT (INITIAL SUBMISSION)

The preferred format for initial submission manuscripts is 12 point Times Roman font, single line spacing and single column format, with 1 inch for top, bottom, left, and right margins. Manuscripts should be prepared for standard 8.5x11 inch paper.

EDITORIAL REVIEW

In order to ensure an appropriate level of quality control, papers are peer reviewed. They are reviewed both for

technical correctness and for adherence to the listed guidelines regarding information content and format.

PAPER FORMAT (FINAL SUBMISSION)

Only camera-ready electronic files are accepted for publication. The term **"camera-ready" means that the material is neat, legible, reproducible, and in accordance with the final version format listed below.**

The following requirements are in effect for the final version of an ACES Journal paper:

1. The paper title should not be placed on a separate page. The title, author(s), abstract, and (space permitting) beginning of the paper itself should all be on the first page. The title, author(s), and author affiliations should be centered (center-justified) on the first page. The title should be of font size 16 and bolded, the author names should be of font size 12 and bolded, and the author affiliation should be of font size 12 (regular font, neither italic nor bolded).

2. An abstract is required. The abstract should be a brief summary of the work described in the paper. It should state the computer codes, computational techniques, and applications discussed in the paper (as applicable) and should otherwise be usable by technical abstracting and indexing services. The word "Abstract" has to be placed at the left margin of the paper, and should be bolded and italic. It also should be followed by a hyphen (—) with the main text of the abstract starting on the same line.

3. All section titles have to be centered and all the title letters should be written in caps. The section titles need to be numbered using roman numbering (I. II. ….)

4. Either British English or American English spellings may be used, provided that each word is spelled consistently throughout the paper.

5. Internal consistency of references format should be maintained. As a guideline for authors, we recommend that references be given using numerical numbering in the body of the paper (with numerical listing of all references at the end of the paper). The first letter of the authors' first name should be listed followed by a period, which in turn, followed by the authors' complete last name. Use a coma (,) to separate between the authors' names. Titles of papers or articles should be in quotation marks (" "), followed by the title of journal, which should be in italic font. The journal volume (vol.), issue number (no.), page numbering (pp.), month and year of publication should come after the journal title in the sequence listed here.

6. Internal consistency shall also be maintained for other elements of style, such as equation numbering. As a guideline for authors who have no other preference, we suggest that equation numbers be placed in parentheses at the right column margin.

7. The intent and meaning of all text must be clear. For authors who are not masters of the English language, the ACES Editorial Staff will provide assistance with grammar (subject to clarity of intent and meaning). However, this may delay the scheduled publication date.

8. Unused space should be minimized. Sections and subsections should not normally begin on a new page.

ACES reserves the right to edit any uploaded material, however, this is not generally done. It is the author(s) responsibility to provide acceptable camera-ready pdf files. Incompatible or incomplete pdf files will not be processed for publication, and authors will be requested to re-upload a revised acceptable version.

COPYRIGHTS AND RELEASES

Each primary author must sign a copyright form and obtain a release from his/her organization vesting the copyright with ACES. Copyright forms are available at ACES, web site (http://aces.ee.olemiss.edu). To shorten the review process time, the executed copyright form should be forwarded to the Editor-in-Chief immediately after the completion of the upload (electronic submission) process. Both the author and his/her organization are allowed to use the copyrighted material freely for their own private purposes.

Permission is granted to quote short passages and reproduce figures and tables from and ACES Journal issue provided the source is cited. Copies of ACES Journal articles may be made in accordance with usage permitted by Sections 107 or 108 of the U.S. Copyright Law. This consent does not extend to other kinds of copying, such as for general distribution, for advertising or promotional purposes, for creating new collective works, or for resale. The reproduction of multiple copies and the use of articles or extracts for commercial purposes require the consent of the author and specific permission from ACES. Institutional members are allowed to copy any ACES Journal issue for their internal distribution only.

PUBLICATION CHARGES

All authors are allowed for 8 printed pages per paper without charge. Mandatory page charges of $75 a page apply to all pages in excess of 8 printed pages. Authors are entitled to one, free of charge, copy of the journal issue in which their paper was published. Additional reprints are available for a nominal fee by submitting a request to the managing editor or ACES Secretary.

Authors are subject to fill out a one page over-page charge form and submit it online along with the copyright form before publication of their manuscript.

ACES Journal is abstracted in INSPEC, in Engineering Index, DTIC, Science Citation Index Expanded, the Research Alert, and to Current Contents/Engineering, Computing & Technology.